Progress in Nuclear Magnetic Resonance Spectroscopy 154–155 (2026) 101600

Contents lists available at ScienceDirect

Progress in Nuclear Magnetic Resonance Spectroscopy

journal homepage: www.elsevier.com/locate/pnmrs

Recent progress in high-field liquid-state Overhauser dynamic nuclear polarization

Luming Yang [a,*], Igor Tkach [a], Alex van der Ham [a,c], Maik Reinhard [a], Yu Rao [a], Tamar Wolf [a,c], Ilya Kuprov [c], Marcel Levien [d], Tomas Orlando [e], Marina Bennati [a,b,*]

[a] Electron-Spin Resonance Spectroscopy, Max Planck Institute for Multidisciplinary Sciences, Am Fassberg 11, 37077 Göttingen, Germany
[b] Institute of Physical Chemistry, Department of Chemistry, Georg-August-University, Tammannstr. 6, 37077 Göttingen, Germany
[c] Department of Chemical and Biological Physics, Weizmann Institute of Science, Herzl St 234, Rehovot 76100, Israel
[d] Institut des Sciences et Ingénierie Chimiques, École Polytechnique FédÉrale de Lausanne (EPFL), CH-1015 Lausanne, Switzerland
[e] National High Magnetic Field Laboratory and Florida State University, 1800 E. Paul Dirac Dr., 32310 Tallahassee, Florida, USA

ARTICLE INFO

Editor Name: Thomas Prisner and David Neuhaus

Keywords:
Dynamic nuclear polarization
Overhauser effect
High-resolution NMR
Liquid-state NMR
Hyperpolarization

ABSTRACT

Overhauser-effect dynamic nuclear polarization (OE-DNP) is an emerging method for enhancing the sensitivity of high-resolution nuclear magnetic resonance (NMR) in liquids. OE-DNP generates nuclear spin hyperpolarization by electron-to-nuclear cross-relaxation between the analyte and a paramagnetic polarizing agent doped into the NMR solution. The key advantage of this method is the in situ enhancement of nuclear polarization under steady-state, which is inherently compatible with multiscan signal averaging and multidimensional NMR. Although OE-DNP has been known for several decades, recent demonstrations of one and two-dimensional OE-DNP at high magnetic fields (9 and 14 Tesla) have expanded its application, and opened up new possibilities for NMR-based analysis of drugs, natural products, and heterogeneous catalytic processes. In parallel, progress in quantum chemical calculations and numerical simulation capabilities have started to unravel the atomistic details of the OE-DNP mechanism at high magnetic fields. These studies revealed that hyperpolarization generation relies on sub-picosecond molecular dynamics and hyperfine coupling through non-covalent intermolecular interactions, such as hydrogen and halogen bonds. This understanding enables not only the rational design of OE-DNP experiments tailored to different samples, but provides new insight into fundamental physics and chemistry in solution as well. In this review, we summarize recent developments of OE-DNP and outline guidelines for its implementation to different nuclei. We start with an overview of the current theoretical framework of OE-DNP, and subsequently, discuss the role of electronic spin saturation and its implications for microwave hardware design at 9 and 14 Tesla. Finally, we review high-field OE-DNP performance of the most extensively investigated nuclei, ^{13}C, ^{1}H, ^{19}F and ^{31}P, and representative applications that illustrate the future potential of this method.

Contents

* Corresponding authors at: Electron-Spin Resonance Spectroscopy, Max Planck Institute for Multidisciplinary Sciences, Am Fassberg 11, 37077 Göttingen, Germany.
E-mail addresses: luming.yang@mpinat.mpg.de (L. Yang), marina.bennati@mpinat.mpg.de (M. Bennati).

https://doi.org/10.1016/j.pnmrs.2026.101600
Received 17 December 2025; Accepted 24 April 2026
Available online 30 April 2026

Glossary of abbreviations

AWG	Arbitrary waveform generator
BDPA	1,3-bisdiphenylene-2-phenylallyl
BRW	Bloch-Redfield-Wangsness theory
C or c	Concentration
COSY	Correlation spectroscopy
CW	Continuous-wave
dDNP	Dissolution dynamic nuclear polarization
DFT	Density functional theory
DLPNO-CCSD	Domain-based local pair natural orbital coupled-cluster with singles and doubles
DNP	Dynamic nuclear polarization
DOPC	1,2-dioleoyl-*sn*-glycero-3-phosphocholine
DQF-COSY	Double-quantum-filtered correlation spectroscopy
EIO/EIA	Extended interaction oscillator/klystron amplifier
ELDOR	Electron-electron double resonance
ENDOR	Electron-nuclear double resonance
EPR	Electron paramagnetic resonance
FEP	Fluorinated ethylene propylene
FID	Free-induction decay
HETCOR	Heteronuclear correlation spectroscopy
HSFF	Hard-sphere force-free
INADEQUATE	Incredible natural-abundance double-quantum transfer experiment
INEPT	Insensitive nuclei enhanced by polarization transfer
MAS-DNP	Magic angle spinning dynamic nuclear polarization
MD	Molecular dynamics
MRI	Magnetic resonance imaging
MW	Microwave
$N@C_{60}$	Nitrogen-atom-endohedral C_{60}
NMR	Nuclear magnetic resonance
NMRD	Nuclear magnetic resonance dispersion
NOE	Nuclear Overhauser effect
NOESY	Nuclear Overhauser effect spectroscopy
OE-DNP	Overhauser-effect dynamic nuclear polarization
PBG	Photonic band-gap
PFAS	*Per-* and polyfluoroalkyl substances
PHIP	Parahydrogen-induced hyperpolarization
Photo-CIDNP	Photochemically-induced dynamic nuclear polarization
QM/MM	Quantum mechanics/molecular mechanics
RF	Radiofrequency
SABRE	Signal amplification by reversible exchange
SE	Solid effect
SENS	Surface enhanced NMR spectroscopy
SF	Supercritical fluid
SOMO	Singly-occupied molecular orbital
TEMPO	2,2,6,6-tetramethylpiperidin-1-oxyl
TEMPOL	4-hydroxy-2,2,6,6-tetramethylpiperidin-1-oxyl
TEMPONE	4-oxo-2,2,6,6-tetramethylpiperidin-1-oxyl
TOCSY	Total correlation spectroscopy
TROSY	Transverse relaxation-optimized spectroscopy
TTBP	2,4,6-tri-tert-butylphenoxyl
TWT	Traveling wave tube

(*continued on next column*)

(*continued*)

1. Introduction

Nuclear magnetic resonance (NMR) spectroscopy is an indispensable tool for probing molecular structure and chemical dynamics, and for

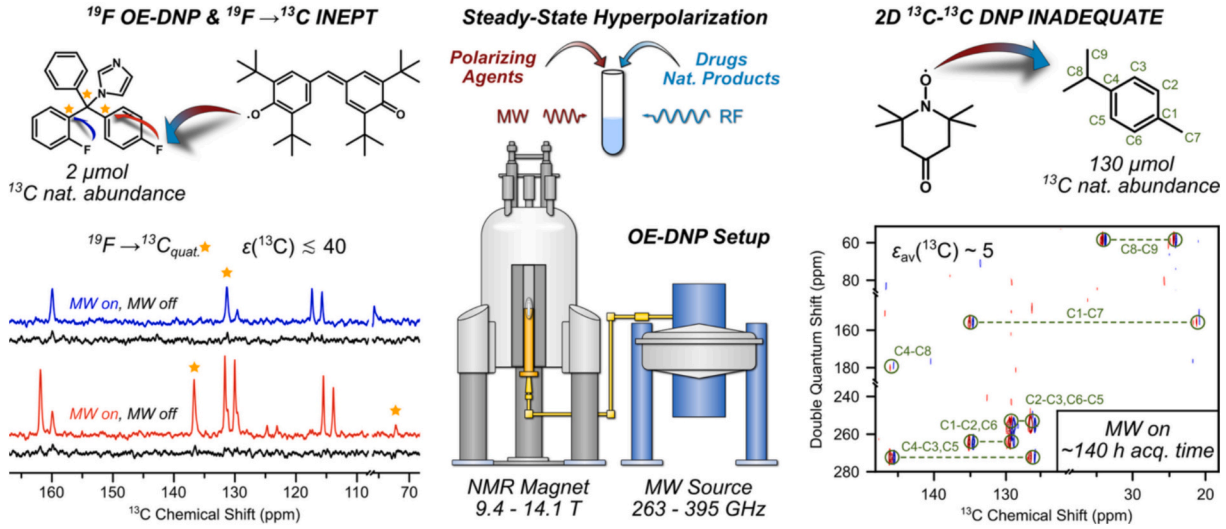

Scheme 1. Representation of a high-field OE-DNP experiment, where the polarizing agent is mixed with the analyte solution and is pumped in situ by a microwave source. Left: enhancement of natural-abundant, quaternary ^{13}C ($^{13}C_{quat.}$) signals of a drug through heteronuclear hyperpolarization transfer. [39] Right: example of an OE-DNP enhanced 2D ^{13}C—^{13}C correlation experiment at natural ^{13}C abundance. [40] ε represents enhancements and subscript "av" represents average of all nuclei in the molecule.

characterizing complex systems ranging from small organic molecules and catalytic intermediates to biological macromolecules. Such applications usually necessitate high chemical shift resolution, roughly corresponding to operation at magnetic fields $\gtrsim$ 9 T in modern NMR analysis. Over the last two decades, it has been widely recognized that an inherent limitation of NMR is the low sensitivity, arising from the small nuclear polarization (i.e., the population difference of the nuclear spin states) at thermal equilibrium. For example, at room temperature and a magnetic field of 9.4 Tesla, the proton polarization is only about 32 ppm (parts per million), and that of carbon-13 is approximately 8 ppm. Because the polarization increases linearly with the magnetic field, the sensitivity limitation of NMR persists even at the highest commercially available static polarizing field of 28.8 Tesla, [1] and is particularly severe for dilute samples, transient species, or high-throughput analysis.

Over the past two decades, overcoming this sensitivity barrier has been a central goal of magnetic resonance research. The resulting field of study, known as hyperpolarization, encompasses a range of physical and chemical strategies designed to generate non-equilibrium population of nuclear spin states with significantly enhanced polarization. Historically, dynamic nuclear polarization (DNP) was the first such method, originally proposed by Overhauser in 1953 in the solid state. [2] Early investigations of DNP in liquids [3,4] and solids [5–9] were performed up to ~1.5 Tesla. Later in the 1990s, Griffin and coworkers expanded DNP in combination with magic angle spinning (MAS) NMR for biological applications in the solid state. [10] Subsequently, DNP-based methods were developed to boost sensitivity also for liquid-state NMR, including dissolution DNP (dDNP) [11–13], Overhauser-effect dynamic nuclear polarization (OE-DNP) [14–16], and photochemically-induced dynamic nuclear polarization (photo-CIDNP) [17–19] at magnetic fields above 3 Tesla. These approaches exploit the much larger polarization of the unpaired electron spin on a polarizing agent in the NMR sample. Indeed, electron spin polarization close to unity can be generated at magnetic fields larger than 3.3 Tesla and cryogenic temperatures below 4.2 K [20], or through optical excitation. In the latter scenario, photogenerated electron spin triplet states have been investigated as polarization sources for DNP in both solids and liquids. [21] Concurrently, parahydrogen-induced hyperpolarization (PHIP) [22,23] and the closely associated method of signal amplification by reversible exchange (SABRE) emerged as powerful alternatives. [24,25] Both methods utilize the large polarization created and stored in the singlet proton spin state of parahydrogen. These hyperpolarized protons are subsequently introduced into the target analyte by either irreversible hydrogenation of the substrate, as in PHIP [26], or reversible chemical exchange with a catalyst, as in SABRE [27]. Across these approaches, huge NMR signal enhancements up to 10^4 to 10^5 have been achieved for nuclei such as ^1H, ^{13}C, ^{19}F, and ^{15}N, translating to detection limits in the micro- to nano-, or even picomole range. [28] These methods have already led to spectacular new applications, notably in metabolic profiling and magnetic resonance imaging (MRI). [29–34] Nevertheless, some of these methods are inherently limited to short acquisition times, often on the order of the nuclear spin-lattice relaxation time, as hyperpolarization is not regenerated after NMR acquisition. While specialized sequences have been developed to circumvent this issue [35–38], methods capable of continuously generating steady-state hyperpolarization remain of considerable interest.

This review focuses on Overhauser-effect dynamic nuclear polarization (OE-DNP), a promising method for the in situ hyperpolarization of small molecules in liquids. In OE-DNP, nuclear spin polarization, and subsequently the NMR signal, is enhanced by intermolecular electron-nuclear cross-relaxation associated with the unpaired electron spins located on the polarizing agents, which are paramagnetic molecules doped into the NMR solution. Polarization transfer is induced by excitation and saturation of the polarizing agent electron paramagnetic resonance (EPR) transitions, which transiently couple to the nucleus of interest by intermolecular hyperfine interaction. In contrast to many other liquid-state hyperpolarization techniques, OE-DNP generates nuclear hyperpolarization under steady-state conditions. Therefore, it is intrinsically compatible with "multi-shot" NMR experiments, and data acquisition is not limited by nuclear spin-lattice relaxation. Consequently, OE-DNP can be integrated into existing one- and multidimensional NMR schemes without significant modification, apart from hardware requirements and the chemical compatibility of the polarizing agents with the target solution (Scheme 1). This feature renders OE-DNP highly attractive, despite its lower achievable enhancements (typically 10^1–10^3) relative to dDNP, photo-CIDNP, or PHIP/SABRE.

Conceptually, OE-DNP originates from the seminal work by Overhauser, who predicted that EPR saturation of conducting electrons in a metal should lead to an increased spin polarization of hyperfine-coupled nuclei. [2] Using the relaxation theory derived by Solomon [41], the Overhauser effect in liquids was initially reviewed by Hausser and Stehlik [3]. Several studies of liquid-state OE-DNP were conducted in

the 1980–1990s by Müller-Warmuth [4], Dorn [42], and others. Although these studies were performed at low magnetic fields (up to about 1 T), they established the theoretical framework that served as a basis for current understanding of OE-DNP at higher magnetic fields. This theory, together with recent progress, is outlined in section 2.

The advent of commercially available high-frequency microwave (MW) sources enabled the extension of liquid-state OE-DNP to high magnetic fields up to 14 T. An early study was reported in 2002 by Griffin and coworkers at 5 T ($\nu(^1H) = 211$ MHz, $\nu(e^-) = 140$ GHz), using a gyrotron as the MW source. [43] Later, Bennati and Prisner [44,45] demonstrated ^{1}H OE-DNP experiments at 3 and 9 T, respectively, for water doped with nitroxide radicals using EPR optimized resonant structures. Prisner and coworkers further implemented a high-power gyrotron in generating OE-DNP. [46] More recent developments of high-field liquid state OE-DNP have focused on overcoming the hardware challenges for simultaneously achieving high NMR resolution and sensitivity, as well as efficient MW excitation of the sample in the sub-THz frequency range. These efforts are reviewed in sections 3 and 4, which address EPR saturation behavior and probehead design principles, respectively.

Finally, one of the most peculiar observations of liquid-state OE-DNP was the dipolar-driven, negative signal enhancements for ^{1}H nuclei, which decay substantially with increasing magnetic fields. This behavior has been reviewed in detail in [14] and [15]. In contrast, studies in 2017 and 2019 from Bennati and coworkers demonstrated sizable positive and scalar-dominated OE-DNP enhancements for ^{13}C at intermediate (3.4 T) and high (9.4 and 14.1 T) magnetic fields, as reviewed in [16]. These findings highlight the critical influence of the electronic and chemical properties of the nucleus of interest. Since then, the community has witnessed substantial progress in elucidating high-field liquid-state OE-DNP mechanism and expanding its applications at 9 and 14 T. OE-DNP-enhanced one- (1D) and two-dimensional (2D) NMR experiments have been reported, and strategies for propagating hyperpolarization from strongly polarized sites across networks of coupled nuclei are emerging. While site-specificity of OE-DNP still remains a challenge, more general principles of protocols for practical application are becoming apparent. OE-DNP performance for different nuclei, along with emerging applications, are reviewed in section 5.

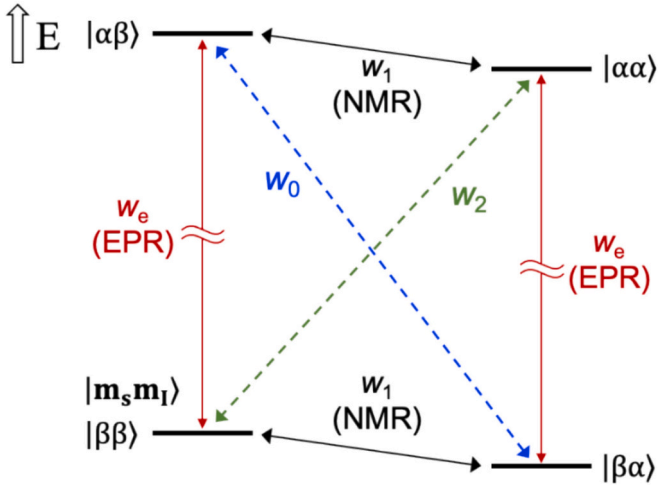

Fig. 1. Energy-level diagram of an $S = 1/2$ electron spin hyperfine coupled to an $I = 1/2$ nuclear spin with positive gyromagnetic ratio. w_i mark transition probabilities per unit time; w_e and w_1 correspond to electron and nuclear single-quantum transitions, respectively. w_0 and w_2 correspond to zero and double-quantum transitions, respectively, with the dashed lines representing their nature as forbidden transitions.

2. Theory of liquid-state OE-DNP

In the liquid state, the efficiency of OE-DNP is related to multiple factors, including strengths of the hyperfine and Zeeman interactions, timescale of molecular motions, efficiency of various relaxation pathways, and the degree of EPR saturation. Relaxation rates and EPR spectral profiles are further dependent on the magnetic field at which OE-DNP is performed. As a result, rational optimization of the liquid-state OE-DNP requires detailed understanding of the underlying physical and chemical principles. In the following section, we discuss the relaxation theory and its implications in OE-DNP at various magnetic fields. We then discuss insights into the microscopic OE-DNP process offered by computational chemistry, and ongoing efforts in describing OE-DNP with the Bloch-Redfield-Wangsness (BRW) theory.

2.1. Master equations

The interaction of an electron spin $S = 1/2$ coupled to a nuclear spin $I = 1/2$ is described by the spin Hamiltonian consisting of electron and nuclear Zeeman and hyperfine terms:

$$\hat{H} = \mu_B \boldsymbol{B}\cdot\mathbf{g}\cdot\hat{\boldsymbol{S}} - \mu_N g_n \boldsymbol{B}\cdot\hat{\boldsymbol{I}} + \hat{\boldsymbol{S}}\cdot\mathbf{A}\cdot\hat{\boldsymbol{I}} \tag{1}$$

where $\boldsymbol{B}$ is the vector for the external magnetic field, $\mathbf{g}$ the electronic g tensor, g_n the isotropic nuclear g factor, $\mathbf{A}$ the hyperfine tensor, μ_B and μ_N the Bohr and nuclear magnetons, respectively. The hyperfine Hamiltonian is written as a sum of the scalar $\hat{H}^{sc}$ and dipolar $\hat{H}^{d}$ parts as: [41,47]

$$\hat{H}^{sc} = A^N_{iso}\hat{\boldsymbol{S}}\cdot\hat{\boldsymbol{I}} \text{ with } A^N_{iso} = \frac{2\mu_0}{3} g_e \mu_B g_n \mu_N \rho_N^{\alpha-\beta} \tag{2a}$$

$$\hat{H}^{d} = k_m g_e \mu_B g_n \mu_N \left[\frac{3(\hat{\boldsymbol{S}}\cdot\boldsymbol{r})(\boldsymbol{r}\cdot\hat{\boldsymbol{I}})}{r^5} - \frac{\hat{\boldsymbol{S}}\cdot\hat{\boldsymbol{I}}}{r^3}\right] \tag{2b}$$

where A^N_{iso} in energy units is the isotropic hyperfine constant at the observed nucleus N, g_e the isotropic g factor, and $\rho_N^{\alpha-\beta}$ the electron spin density operator at nucleus N, defined as the difference of contributions with electron spin α and β, $k_m = \mu_0/4\pi$ in SI units, and $\boldsymbol{r}$ the distance vector between the electron and nuclear magnetic moments. Eqs. (2a) and (2b) can be also expressed in terms of the electron and nuclear gyromagnetic ratios γ_e und γ_n, with $\gamma_e = -g_e \bullet \mu_B/\hbar$ and $\gamma_n = g_n \bullet \mu_N/\hbar$. The Hamiltonian (eq. (1)) gives rise to a system with four energy eigenstates, schematically depicted in Fig. 1. We note that the frequency of EPR transitions at a field of 9 Tesla is approximately 260 GHz, whereas the corresponding frequency of NMR transitions ($\lesssim$ 400 MHz) is scaled according to γ_e/γ_n. The Boltzmann equilibrium polarization (population difference) of the EPR and NMR transitions is scaled by the same factor.

The OE-DNP enhancement, defined as $\varepsilon = \langle\hat{I}_z\rangle/I_0$ – the ratio of the nuclear spin expectation value along the external magnetic field over its equilibrium value – is induced by continuous on-resonance excitation of the EPR transitions. In liquids, the enhancement originates from cross-relaxation driven by rapid, random fluctuations of the hyperfine Hamiltonian. Early investigations of liquid-state OE-DNP and its theoretical formulation were carried out by Hausser and Stehlik [3], as well as Müller-Warmuth [4] at low magnetic fields (B $\lesssim$1 Tesla) several decades ago, building on the theory of paramagnetic relaxation developed by Solomon and Bloembergen [41,48] and by Abragam [49]. Since key aspects of OE-DNP theory have been discussed in details in previous reviews, [3,4,14–16,50,51] we here recapitulate just briefly the essential steps to provide the framework for discussing more recent observations at high magnetic fields. The treatment starts with the master equations for the population changes in the four-level system (Fig. 1) under MW irradiation, which leads to a set of coupled differential equations: [3]

$$\frac{d\langle \widehat{I}_z\rangle}{dt} = -(w_0 + 2w_1 + w_2)(\langle \widehat{I}_z\rangle - I_0) - (w_2 - w_0)(\langle \widehat{S}_z\rangle - S_0) \tag{3a}$$

$$\frac{d\langle \widehat{S}_z\rangle}{dt} = -(w_2 - w_0)(\langle \widehat{I}_z\rangle - I_0) - (w_0 + 2w_e + w_2)(\langle \widehat{S}_z\rangle - S_0) \tag{3b}$$

where w_i are the transition probabilities per unit time, i.e. rates, as defined in section 2.2. $w_0 + 2w_1 + w_2 \equiv R_{1,para}$ is the paramagnetic part of the nuclear relaxation rate, and $w_2 - w_0$ is the difference between the cross-relaxation rates. The electron (T_{1e}) and nuclear (T_{1n}) longitudinal relaxation times can be expressed as $T_{1e} = 1/(2w_e)$ and $T_{1n} = 1/(w_0 + 2w_1 + w_2 + R_{1,dia})$, with $R_{1,dia}$ the diamagnetic nuclear relaxation. In a typical liquid-state OE-DNP experiment, the electronic spin relaxation ($T_{1e} \sim 10^2$–10^3 ns) is orders of magnitude faster than the nuclear spin relaxation ($T_{1n} \sim 0.1$–10 s). Under these conditions, eq. (3a) provides an adequate description of the nuclear relaxation. In contrast, eq. (3b) becomes negligible for the electron spin, for which the relaxation is well described by the Bloch equation for an isolated $S = 1/2$ spin. Reaching steady state under continuous-wave (CW) MW irradiation, $d\langle \widehat{I}_z\rangle/dt = 0$, leads to:

$$\langle \widehat{I}_z\rangle = I_0 + \frac{w_2 - w_0}{w_0 + 2w_1 + w_2 + R_{1,dia}}(S_0 - \langle \widehat{S}_z\rangle) \tag{3c}$$

Rearranging eq. (3c) leads to the Overhauser equation:

$$\varepsilon = 1 - \xi \cdot f \cdot s \cdot \frac{|\gamma_e|}{\gamma_n} \tag{4}$$

where the coupling factor ξ, the leakage factor f, and the saturation factor s have the following definitions:

$$\xi = \frac{w_2 - w_0}{w_0 + 2w_1 + w_2} \tag{5a}$$

$$f = \frac{w_0 + 2w_1 + w_2}{w_0 + 2w_1 + w_2 + R_{1,dia}} \tag{5b}$$

$$s = \frac{S_0 - \langle \widehat{S}_z\rangle}{S_0} \tag{5c}$$

Specifically, the leakage factor ($0 \le f \le 1$) describes the contribution of paramagnetic relaxation to the total nuclear spin relaxation, and is maximized when diamagnetic relaxation becomes negligible. The saturation factor ($0 \le s \le 1$) describes the deviation of electron polarization from its equilibrium, and reaches $s = 1$ under complete saturation. Note that the definition of s here is opposite to that in the EPR literature, where $s = \langle \widehat{S}_z\rangle/S_0$ and complete saturation corresponds to $s = 0$. [52].

The contributions of dipolar and scalar relaxation to the coupling factor (eq. (5a)) can be written through additive terms: [3]

$$\xi = \frac{w_2^d - w_0^d - w_0^{sc}}{w_0^d + 2w_1^d + w_2^d + w_0^{sc}} \tag{6}$$

In the limit of purely scalar relaxation, the coupling factor approaches $\xi = -w_0^{sc}/w_0^{sc} = -1$. At the dipolar limit, ξ approaches $+0.5$, in analogy to the well-known nuclear Overhauser effect. [53] Altogether, considering coupling, leakage, and saturation factors, the OE-DNP enhancement ε can reach a theoretical limit of $+|\gamma_e|/\gamma_n$ for scalar-only relaxation, and $-|\gamma_e|/(2\gamma_n)$ for dipolar-only relaxation.

In practice, all three factors of ξ, f, and s, depend on the experimental conditions and may, in principle, be determined independently. Since the expression for f (eq. (5b)) can be rewritten as:

$$f = 1 - \frac{R_{1,dia}}{w_0 + 2w_1 + w_2 + R_{1,dia}} = 1 - \frac{\left(w_0 + 2w_1 + w_2 + R_{1,dia}\right)^{-1}}{\left(R_{1,dia}\right)^{-1}} = 1 - \frac{T_{1n}}{T_{1n}^{dia}} \tag{7}$$

the leakage factor can be determined by measuring the nuclear spin-lattice relaxation times in the presence (T_{1n}) and absence (T_{1n}^{dia}) of the polarizing agent. Given suitable hardware, the saturation factor can be obtained from EPR or NMR measurements, as discussed in section 3. The coupling factor can be extracted from the experimentally obtained OE-DNP enhancement ε, f, and s, using eq. (4). In simple systems, the field dependence of ξ can be modelled using appropriate analytical expressions for spectral densities, provided that the transient hyperfine coupling at the observed nucleus can be estimated or calculated by quantum chemical methods (sections 2.2–2.4). More recently, approaches based on atomistic molecular dynamics simulations or numerical solutions of generalized Redfield theory have been proposed to estimate the coupling factors. These methods are illustrated in sections 2.5 and 2.6.

2.2. Relaxation rates

The relation between transition probabilities per unit time (relaxation rates) w_0, w_1, and w_2 and the spectral density of the randomly fluctuating hyperfine Hamiltonian was derived by Solomon [41] and can be expressed as:

$$w_0^d = k_d \cdot J_d(\omega_n - \omega_e, \tau_d) \tag{8a}$$

$$w_1^d = \frac{3}{2} k_d \cdot J_d(\omega_n, \tau_d) \tag{8b}$$

$$w_2^d = 6k_d \cdot J_d(\omega_n + \omega_e, \tau_d) \tag{8c}$$

$$w_0^{sc} = k_{sc} \cdot J_{sc}(\omega_n - \omega_e, \tau_{sc}) \tag{8d}$$

where ω_n and ω_e are the nuclear and electronic Larmor frequencies (in units of rad/s). The correlation times τ_d and τ_{sc} as well as the prefactors k_d and k_{sc}, for dipolar (d) and scalar (sc) relaxation, respectively, are defined in the following section.

Following the original treatment, [41] eqs. (8a-8d) can be derived from perturbation theory, which gives transition probabilities per unit time between two eigenstates $|m_i\rangle$ and $|m_j\rangle$ (as)

$$w_{ij} = \frac{1}{t}\frac{1}{\hbar^2}\left|\int_0^t \langle m_j|\widehat{H}(t')\,m_i\rangle\, e^{-i\omega_{ij}t'}\,dt'\right|^2 \tag{9}$$

Here, $|m_i\rangle$ and $|m_j\rangle$ correspond to eigenstates in Fig. 1, $\widehat{H}(t)$ is the fluctuating hyperfine Hamiltonian, and ω_{ij} is the transition frequency. Under the assumption that the timescale of fluctuations is much faster than the observation window t (certainly valid for OE-DNP, since the former is of 0.1–10^2 ps for fast-tumbling systems in non-viscous solution), the integral can be rewritten as an ensemble average taken over all nuclear sites at a given time. Using Abragam's notation [49], one obtains:

$$\langle w_{ij}\rangle_{av} = \frac{1}{\hbar^2}\int_{-\infty}^{\infty} \overline{\langle m_i|\widehat{H}(t)\,m_j\rangle\langle m_j|\widehat{H}^*(t+\tau)\,m_i\rangle}\, e^{-i\omega_{ij}\tau}d\tau = J'(\omega_{ij},\tau) \tag{10}$$

where $\overline{\langle m_i|\widehat{H}(t)\,m_j\rangle\langle m_j|\widehat{H}^*(t+\tau)\,m_i\rangle} = G_{m_i,m_j}(\tau)$ is the autocorrelation function. The integral thus corresponds to the Fourier transform of $G_{m_i,m_j}(\tau)$, resulting in the spectral density function $J'(\omega_{ij},\tau)$. The correlation function of a randomly fluctuating function follows an exponential form, $G(\tau) = G(0)\exp(-|\tau|/\tau_c)$, with a characteristic correlation time τ_c. Subsequently, the Fourier transform yields a Lorentzian spectral density function:

$$J'(\omega,\tau_c) = G(0)\frac{2\tau_c}{1+\omega^2\tau_c^2} = G(0)\cdot J(\omega,\tau_c) \tag{11}$$

In our case, where the fluctuating Hamiltonian is the hyperfine interaction, $G(0)$ represents the prefactor in eqs. (8a-8d) for the different components of the hyperfine Hamiltonian. [41] Note that $J(\omega,\tau_c)$ and $J(\omega,\tau_c)$ only differ by the prefactor. Eq. (11) dictates that the relaxation process defined by $J(\omega,\tau_c)$, including cross-relaxation, becomes most efficient when τ_c is the on the order of $1/\omega$ for fixed ω. This has important implications for OE-DNP with cross-relaxation at frequencies $\omega_e \pm \omega_n \approx \omega_e$ (see eq. (8)). This point is illustrated in section 2.4. In the following sections, we use the abbreviations τ_d and τ_{sc} only in conjunction with the Lorentzian function.

In practice, a Lorentzian spectral density often serves as an approximation for explaining experimentally observed OE-DNP enhancements and their magnetic field dependence. Several models have been developed to describe the polarizing agent-analyte relative motions, which contribute to either scalar- or dipolar-driven relaxation. Reliable application and distinction of those models require measurement of OE-DNP coupling factors ξ at multiple magnetic fields (for instance, at 0.3 T, 1.2 T, 3.4 T, and 9.4 T). In the following part, we describe models that have been validated against experiments, which mainly involves OE-DNP of ^{13}C and ^{1}H.

2.3. Spectral density models for dipolar and scalar relaxation

For small molecules in solution, three phenomenological processes have been shown as relevant sources for random fluctuation of the polarizing agent-analyte hyperfine interaction – translational diffusion, rotational diffusion, and molecular collision. [3,16,54,55] The two diffusional processes modulate the intermolecular dipolar hyperfine coupling by changing the inter-dipole distance or orientation. The collisional process modulates the isotropic hyperfine coupling of the polarizing agent-analyte transient complex formed in solution.

The relative translational diffusion between the polarizing agent and the analyte was described by the hard-sphere force-free (HSFF) model [56–58], in which molecules are approximated as non-interacting rigid spheres undergoing Brownian motion. The corresponding spectral density function has the form:

$$J_{d,trans}(\omega,\tau_{d,trans}) = \frac{1+5z/8+z^2/8}{1+z+z^2/2+z^3/6+4z^4/81+z^5/81+z^6/648} \tag{12}$$

where z relates to the correlation time of the translational diffusion $\tau_{d,trans}$ and the frequency ω as through $z = \sqrt{2\omega\tau_{d,trans}}$. This correlation time can be calculated from $\tau_{d,trans} = r_d^2/D$, where r_d (in unit of m) is the distance of polarizing agent-analyte closest approach, and D is the sum of the diffusion coefficients of the polarizing agent and the analyte (in unit of m^2/s). The corresponding prefactor in eqs. (8a-c) takes the form:

$$k_{d,trans} = \frac{32000\pi}{405}\left(\frac{\mu_0}{4\pi}\right)^2 \cdot \frac{N_A C \gamma_n^2 g_e^2 \mu_B^2 S(S+1)}{r_d D} \tag{13}$$

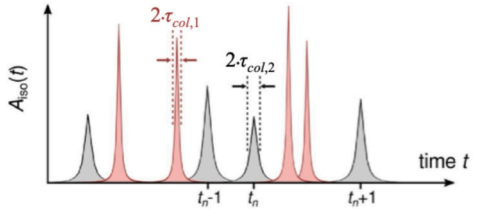

Fig. 2. Schematic representation of the temporal fluctuation of the isotropic hyperfine constant $A_{iso}(t)$ as described by the pulse model. Red and gray shaded peaks represent two types of collisions with Lorentzian pulse shapes but different characteristic durations. Adapted from ref. [64]. (For interpretation of the references to colour in this figure legend, the reader is referred to the web version of this article.)

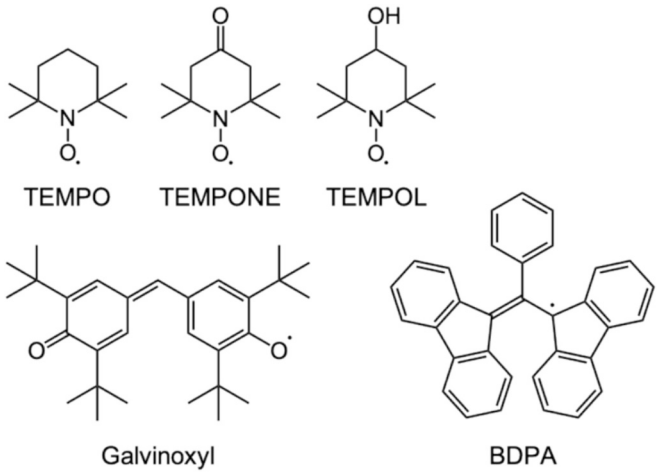

Scheme 2. Structure of selected polarizing agents for high-field liquid-state OE-DNP.

where N_A is the Avogadro constant, C is the polarizing agent concentration ($mol \bullet L^{-1}$). For typical organic molecules with molar mass below approximately 700 Da, $\tau_{d,trans}$ ranges from 10^1 to 10^2 ps. We note that r_d may not equal exactly the distance between the centers of mass of the molecules, or that between the dipolar-coupled electron and nuclear spins. This effect has been studied in the context of NMR relaxation [59,60], and recently, also in OE-DNP at multiple magnetic fields [61].

Dipolar relaxation can further include contributions from rotation of the transiently-formed polarizing agent-analyte complex (so-called inner-sphere relaxation). Under the approximation that the interacting spins are located at the centers of the spheres, the spectral density can be represented by a Lorentzian function: [4,58]

$$J_{d,rot}(\omega,\tau_{d,rot}) = \frac{2\tau_{d,rot}}{1+\omega^2\tau_{d,rot}^2} \tag{14}$$

with $\tau_{d,rot}$ being the rotational correlation time, which can be extracted from line shape analysis of EPR spectra if the polarizing agent displays g and hyperfine anisotropy, such as in nitroxide radicals. For nitroxide and galvinoxyl (2,6-di-tert-butyl-α-(3,5-di-tert-butyl-4-oxo-2,5-cyclohexadien-1-ylidene)-p-tolyloxy) polarizing agents employed in high-field OE-DNP, $\tau_{d,rot}$ typically lies in the range of 10^0 to 10^2 ps in low-viscosity organic solvents such as toluene, carbon tetrachloride (CCl_4), and dimethyl sulfoxide-methanol mixtures. [62–64] When the nitroxide radicals are anchored onto larger particles, such as fullerenes [62,65] and nanoparticles [66], $\tau_{d,rot}$ can reach up to hundreds of picoseconds. Unlike translational diffusion, rotational diffusion has been more difficult to quantify when analyzing the OE-DNP profile. The prefactor in eqs. (8a-c) is given by: [58]

$$k_{d,rot} = \frac{2}{15} f_M \left(\frac{\mu_0}{4\pi}\right)^2 \cdot \frac{\gamma_n^2 g_e^2 \mu_B^2 S(S+1)}{r^6} \tag{15}$$

where r is the distance between the electronic and nuclear spins in the bound position, and f_M is the mole fraction of the analyte in the complexes state.

Modulation of isotropic, intermolecular hyperfine coupling with the target nucleus results from molecular collisions, which can be described analytically by the so-called pulse model. [54,67] This model invokes the formation of a polarizing agent-analyte transient complex stabilized by non-covalent interaction, a prerequisite for Fermi contact that relies on orbital overlap and through-bond radical-to-analyte spin polarization transfer. Intermolecular collision events can be described by Poisson statistics, with each collision represented by a peak ("pulse") in the hyperfine coupling at the nucleus, [68] while possessing characteristic collision frequency τ_p^{-1} and collision duration τ_{col} (Fig. 2).

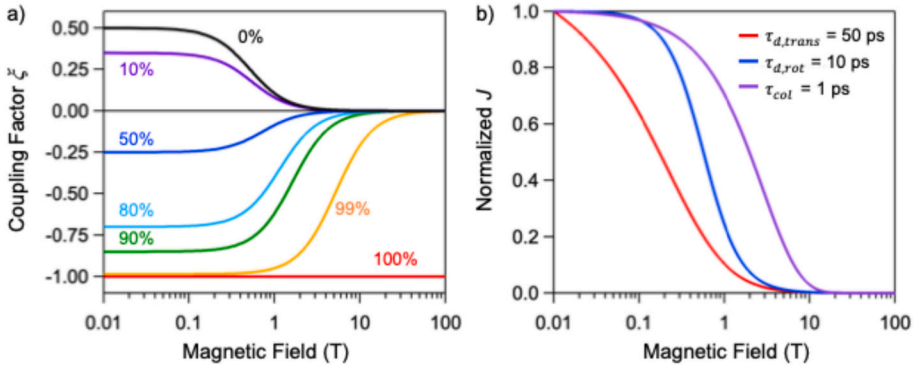

Fig. 3. (a) Magnetic field dependence of the coupling factor calculated with eq. (18) as a function of $100 \times (R_{1,scalar}/R_{1,para})$ for mixed scalar and dipolar relaxation, using one single correlation time $\tau_d = \tau_{sc} = 20$ ps as well as Lorentzian spectral densities. (b) Magnetic field dependence of normalized spectral densities for translational diffusion (HSFF model, red), rotational diffusion (Lorentzian model, blue), and molecular collision (pulse model, purple) with correlation times relevant for small molecules in solutions (given in the inset). (For interpretation of the references to colour in this figure legend, the reader is referred to the web version of this article.)

When the pulses are approximated by Lorentzian profiles, the spectral density function for scalar relaxation can be derived analytically as: [54,67]

$$J_{sc}(\omega_e) = \sum_i \frac{4\pi^2}{\tau_{p,i}} \frac{\langle A_i^2 \rangle}{h^2} \left[\tau_{col,i} \exp\left(-\omega_e \tau_{col,i}\right)\right]^2 \tag{16}$$

where $\langle A_i^2 \rangle$ is the mean squared amplitude of the isotropic hyperfine interaction (in energy units), and the sum runs over different types of collisions i. The prefactor in eq. (8d) takes the form $k = 2S(S+1)/3$, which becomes 1/2 for an $S = 1/2$ polarizing agent. This mechanism has been shown to produce substantial enhancements at intermediate [69] and high magnetic fields (up to 14 Tesla). Quantitative studies of representative systems, such as complexes of the nitroxide 4-oxo-2,2,6,6-tetramethylpiperidin-1-oxyl (TEMPONE) with chloroform ($CHCl_3$) and CCl_4, 1,3-bisdiphenylene-2-phenylallyl (BDPA) with triphenylphosphine, as well as galvinoxyl (see Scheme 2 for polarizing agent structures) with hexafluorobenzene are reviewed in detail in section 5.1. For these systems, $\tau_{p,i}$ are approximately 10^1 ps, and $\tau_{col,i}$ are on the order of 10^{-1} to 10^1 ps. Importantly, among the three processes discussed above, scalar coupling behaves as the only one that can be modulated on the sub-picosecond timescale. Indeed, collision is expected to produce small changes in bond lengths and orbital overlap, which are sufficient for inducing considerable changes in the spin polarization transfer mediated by molecular orbital overlap. For eq. (16), one can readily see that the maximum of each contribution is found at $\omega_e \tau_{col,i} \approx 1$ for fixed ω_e. At 9.4 T, where the OE-DNP frequency is $\omega/2\pi \approx 263$ GHz, we expect most efficient relaxation at $\tau_{col,i} \approx 0.6$ ps. Therefore, sub-picosecond dynamics becomes key for improving the efficiency of liquid-state OE-DNP at high magnetic fields.

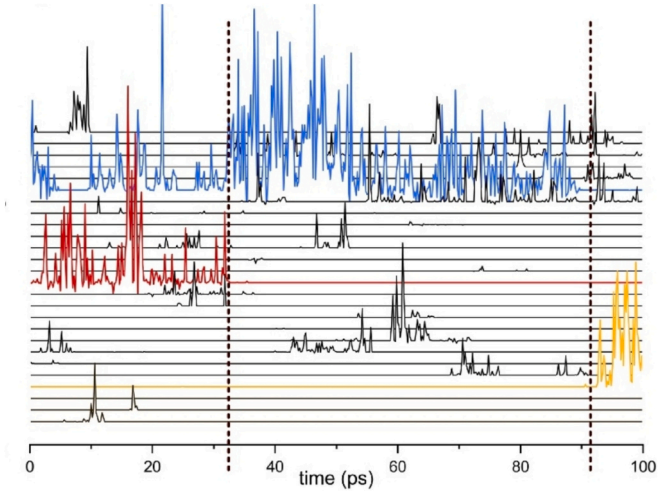

Fig. 4. Selected time-dependence traces of the ^{13}C isotropic hyperfine interaction between $CHCl_3$ molecules and the TEMPONE polarizing agent, as evaluated by MD and DFT analysis (time resolution 0.2 ps). Cluster of spikes of the hyperfine constant $A_{iso}(t)$ represents hydrogen bond-like polarizing agent-analyte interaction. Dashed lines mark time points when hydrogen bond-like complex jumps from one $CHCl_3$ molecule to another. The traces of $CHCl_3$ that form a long (> 20 ps) transient complex with TEMPONE are highlighted in colors. Adapted from ref. [64].

2.4. Field dependence of OE-DNP enhancements

Combining eqs. (6) and (8), the OE-DNP coupling factor can be expressed as:

$$\xi = \frac{5k_d \cdot J_d(\omega_e \tau_d) - k_{sc} \cdot J_{sc}(\omega_e)}{7k_d \cdot J_d(\omega_e \tau_d) + 3k_d \cdot J_d(\omega_n \tau_d) + k_{sc} \cdot J_{sc}(\omega_e)} \tag{17}$$

We note that the similar expression derived by Hausser and Stehlik [3] contains an additional term describing the scalar relaxation of the second kind, i.e. when the electron spin relaxation T_{1e} becomes a source of time dependence for the scalar coupling and subsequently induces nuclear transitions. However, experimental evidence shows that for organic polarizing agents T_{1e} is on the order of $\gtrsim 100$ ns (see section 3) and $\tau_{col} \lesssim 1$ ps for molecular collisions (see section 2.3), thus precluding the need of this additional term.

Since dipolar and scalar relaxation generally coexist and contribute with opposing effects, the OE-DNP efficiency depends critically on the chemical system and the involved spectral densities of molecular motion. For instance, for ^1H OE-DNP, only dipolar-driven enhancements have been reported to date up to 14 Tesla, and scalar relaxation is essentially negligible. However, for heteronuclei such as ^{13}C, ^{19}F, and ^{31}P, both dipolar and scalar mechanisms have been observed, with several examples discussed in section 5.

For a better understanding of the field dependence, ξ can be expressed in terms of the measurable relaxation rate $R_1 = {}^1/_{T_1}$ and its paramagnetic and diamagnetic components, $R_1 = R_{1,para} + R_{1,dia}$, with: [16]

$$\xi = \frac{5}{7}\left[1 - \frac{3k_d \cdot J_d(\omega_n \tau_d)}{R_{1,para}}\right] - \frac{12}{7}\frac{R_{1,scalar}}{R_{1,para}} \tag{18}$$

Within this formulation, the coupling factor can be computed as a function of the scalar contribution $R_{1,sc}$ to the total paramagnetic relaxation, $R_{1,scalar}/R_{1,para}$. Fig. 3a plots a representative field

dependence of ξ as a function of $R_{1,scalar}/R_{1,para}$, calculated with $\tau_d = \tau_{sc} =$ 20 ps, assuming Lorentzian spectral density functions for both $J_{sc}(\omega_e, \tau_{sc})$ and $J_d(\omega_n, \tau_d)$. As can be seen, ξ decays more slowly at high magnetic fields as $R_{1,scalar}/R_{1,para}$ (increases).

In reality, however, different molecular processes lead to different spectral densities as illustrated in section 2.3. This is illustrated in Fig. 3b, where the spectral densities are calculated using realistic models and correlation times discussed in section 2.3 – HSFF model for translational diffusion (eqs. (12−13)), Lorentzian function for rotational diffusion (eqs. (14–15)), and pulse model for molecular collision (eq. (16)). The calculations evidently show that at high magnetic field, scalar relaxation remains as the only mechanism for inducing OE-DNP.

2.5. Molecular dynamics predictions of OE-DNP

While analytical models provide a phenomenological description of molecular dynamics (MD) of the polarizing agent/analyte pair and allow interpretation of the experimental data, a more accurate description with atomistic details can only be obtained with MD simulations. Compared to an analytical approach, numerical methods become beneficial if the complexity of the system exceeds what a model can describe, for instance, when multiple types of interactions and molecular motions coexist, [61] or when complex local and internal motions, as well as chemical interactions, must be taken into account.

So far, computational analysis of liquid-state OE-DNP has been reported only for a few selected systems, mainly focusing on ^{1}H and ^{13}C. Multiple studies by Sezer and coworkers have investigated the interaction of nitroxide radicals with water, acetone, and $CHCl_3$ at various magnetic fields. [70–74] A recent report by Orlando and coworkers [64] employed MD simulations in combination with density function theory (DFT) calculations to predict the time-dependent hyperfine couplings A (t) for ^{13}C in the $CHCl_3$/TEMPONE system. The computed A_m(t) trajectories (Fig. 4) for multiple ^{13}C nuclei labeled by m were used to numerically evaluate the autocorrelation function $G(t)$ (see also eq. (10−11)):

$$G(t) = \sum_m G_m(t) \sim \sum_m \langle A_m(\tau) \cdot A_m(\tau + t) \rangle_\tau \tag{19}$$

The corresponding spectral density function was subsequently obtained by a numerical one-sided Fourier transform of $G(t)$: [71]

$$J_{SC}(\omega_e) = Re\left\{ \int_0^\infty G(t) \exp(-i\omega_e t) dt \right\} \tag{20}$$

This approach enabled the direct comparison of experimentally measured, field dependent coupling factors with simulations based on analytical expressions (eq. (16)), the BRW theory (see section 2.6), and the numerical predictions from molecular dynamics.

One important insight from this report is that slow (10^1 ps) processes, for instance, those involving hydrogen bonds, do not exclude the existence of fast (< 1 ps) dynamics, the latter of which are crucial for achieving OE-DNP at high magnetic fields. Indeed, sub-picosecond fluctuations have been observed on top of a slow, tens-of-ps process related to $CHCl_3$-nitroxide hydrogen bonds (Fig. 4).

Classical MD, however, inherently neglects quantum mechanical effects, such as structural change and electronic spin density redistribution upon formation of polarizing agent-analyte transient complexes. Towards this end, Dai and coworkers applied a quantum mechanics/molecular mechanics (QM/MM) approach to study the ^{13}C OE-DNP effect of indole and CCl_4 induced by nitroxide radicals. [75] Indeed, QM/MM revealed sub-picosecond fluctuation of molecular structure and electron spin density distribution, and suggested that polarizing agent-analyte hydrogen bonding exerts a major influence on the OE-DNP effect of indole. Nevertheless, no clear correlation between these fluctuations and the ^{13}C DNP enhancements could be established for the different carbons of indole, reflecting the complexity of the liquid-state OE-DNP process. Additionally, it is worth noting that simulating molecular motions relevant to OE-DNP usually involves computational description of the system over multiple orders-of-magnitude in timescale, from 10^3 ps down to ~0.01 ps, posing significant challenge for computational modeling.

2.6. Numerical methods for Bloch-Redfield-Wangsness theory

The derivation of liquid-state OE-DNP enhancements based on the theory of Solomon, Bloembergen, Hausser, and Stehlik considers a specialized case of one $S = 1/2$ electron coupled to one $I = 1/2$ nucleus. The relevant Hamiltonians include Zeeman and hyperfine interactions. In reality, NMR analytes almost always consist of multiple NMR-active nuclei. Other perturbations, such as chemical shift anisotropy, g-anisotropy, electronic or chemical exchange, quadrupolar effects, and potential cross-correlation might induce electron-nuclear cross-relaxation as well. For a more generalized description of the OE-DNP process, reports have explored BRW relaxation theory, of which the Solomon-Bloembergen description is a special case.

BRW theory assumes that the stochastic processes responsible for the time-dependent coefficients in the perturbation Hamiltonian are stationary random functions. [76,77] The perturbation Hamiltonian is split into a static part $\hat{H}_0$ and a stochastic part $\hat{H}_1(t)$. The hat symbol corresponds to operators in Hilbert space. In this section, the Hamiltonians are given in angular frequency units. The rate of change of the density matrix of the spin system in Liouville space is:

$$\frac{d\hat{\rho}}{dt} = -i\hat{\hat{H}}_0\hat{\rho} - \hat{\hat{R}}\left(\hat{\rho} - \hat{\rho}_{eq}\right) \tag{21}$$

where $\hat{\hat{R}}$ is the relaxation superoperator, $\hat{\hat{H}}_0$ is the static Hamiltonian superoperator of $[\hat{H}_0, \rho]$, $\hat{\rho}$ is the Liouvillian density operator, and the subscript eq represents thermal equilibrium. For mathematical convenience, the stochastic Hamiltonian is expressed as a linear combination of spin basis superoperators (often irreducible spherical tensors) $\hat{\hat{Q}}$ times the spatial component $D(t)$: $\hat{\hat{H}}_1(t) = \sum_{kq} D_{kq}(t)\hat{\hat{Q}}_{kq}$. $\hat{\hat{R}}$ then becomes:

$$\hat{\hat{R}} = -\sum_{k,q}\sum_{k',q'}\int_0^{+\infty} \left\langle D_{kq}(0) D^*_{k'q'}(\tau) \right\rangle \hat{\hat{Q}}_{kq} \exp(-i\hat{\hat{H}}_0\tau)\hat{\hat{Q}}^{\dagger}_{k'q'} \exp(i\hat{\hat{H}}_0\tau) d\tau \tag{22}$$

with k, q the spherical harmonics indices, and the average of the hyperfine fluctuation incorporated into $\hat{H}_0$.

From a computational point of view, the most expensive object in the simulation of liquid state OE-DNP experiments is the relaxation superoperator. When an analytical expression for $\hat{\hat{H}}_1(t)$ is available, three major avenues exist for evaluating $\hat{\hat{R}}$. First, when $\hat{H}_0$ is simple enough to diagonalize, $\hat{Q}_{kq}$ satisfies

$$\exp(-i\hat{H}_0\tau)\hat{Q}_{kq}\exp(i\hat{H}_0\tau) = \exp(-i\omega_{kq}\tau)\hat{Q}_{kq} \tag{23}$$

where ω_k is defined by the commutator $\left[\hat{H}_0, \hat{Q}_{kq}\right] = \omega_{kq}\hat{Q}_{kq}$. [76,77] The integral in eq. (22) then reduces to a sum of Fourier transforms:

$$\hat{\hat{R}} = -\sum_{k,q}\sum_{k',q'}\hat{\hat{Q}}_{kq}\hat{\hat{Q}}^{\dagger}_{k'q'}\int_0^{+\infty}\left\langle D_{kq}(0)D^*_{k'q'}(\tau)\right\rangle \exp(-i\omega_{kq}\tau)d\tau \tag{24}$$

Specific assumptions about the stochastic process in $\hat{\hat{H}}_1(t)$ have been reviewed in the NMR literature [78]. The disadvantage of this method is the need to solve $\left[\hat{H}_0, \hat{Q}_{kq}\right]$, which becomes impractical for large spin systems when $\hat{H}_0$ contains terms beyond simple Zeeman interactions. Second, eq. (22) could be solved by brute-force numerical integration under common magnetic resonance conditions (transition frequencies below 1 THz; $\langle D(0)D^*(\tau)\rangle$ decay below 100 ns), where numerical

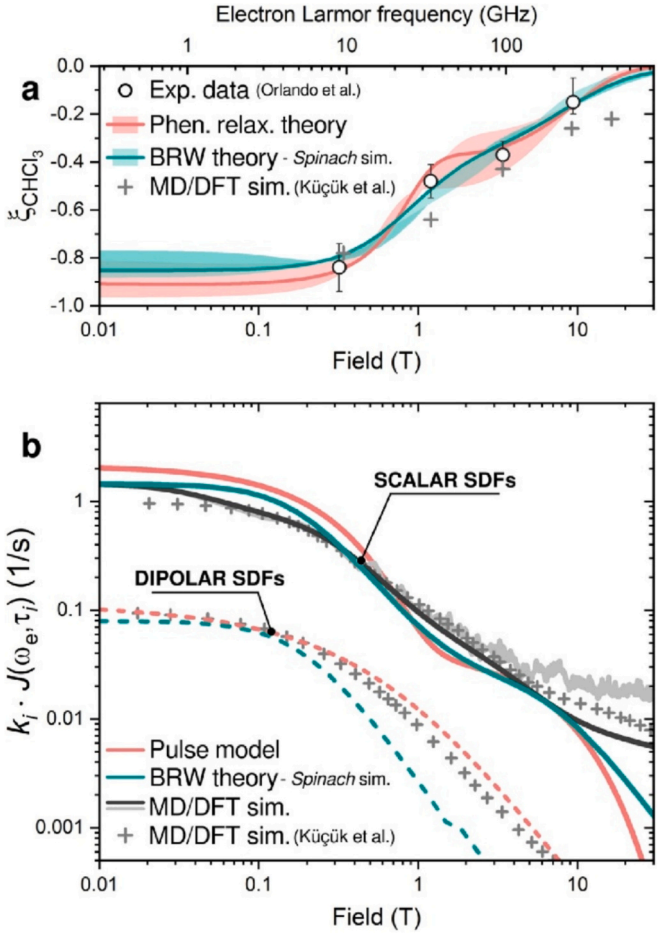

Fig. 5. (a) ^{13}C coupling factor as a function of the external magnetic field for $CHCl_3$ doped with TEMPONE. Comparison of simulations based on semi-classical relaxation theory and with the full BRW treatment with *Spinach*, which include a distribution of collisional times (shaded area). The best agreement (solid lines) was obtained with $2\tau_{sc,1} = 0.5$ ps and $2\tau_{sc,2} = 24$ ps for the semi-classical model and $2\tau_{sc,1} = 0.8$ ps and $2\tau_{sc,2} = 30$ ps for the full BRW treatment. The coupling factor calculated with numerical simulations (MD/DFT) is from ref. [74]. (b) Scalar and dipolar spectral density functions from the models used to simulate the coupling factors. Reproduced from ref. [64].

quadratures work well. [79] This route avoids diagonalization and is compatible with restricted Liouville space, [80] which has thus enabled the first Liouville-space time-domain NOESY simulation of an entire protein. [81] Nevertheless, this approach can still require thousands of expensive matrix operations. The third option is the auxiliary matrix method. When the autocorrelation function can be expressed as a linear combination of exponentials, $\sum_n a_n e^{-\lambda_n t}$, Redfield's integral may be computed in one matrix operation using the general block matrix relation: [82–84]

$$\exp\left[\begin{pmatrix} \boldsymbol{A} & \boldsymbol{B} \\ \boldsymbol{0} & \boldsymbol{C} \end{pmatrix} t\right] = \begin{pmatrix} e^{\boldsymbol{A}t} & e^{\boldsymbol{A}t}\int_0^t e^{-\boldsymbol{A}\tau}\boldsymbol{B}e^{\boldsymbol{C}\tau}d\tau \\ \boldsymbol{0} & e^{\boldsymbol{C}t} \end{pmatrix} \tag{25a}$$

In the context of liquid-state OE-DNP, this translates into: [85]

$$\int_0^T e^{-i\boldsymbol{H}_0\tau}\boldsymbol{Q}e^{i(\boldsymbol{H}_0\tau+i\lambda\boldsymbol{1})\tau}d\tau = \boldsymbol{F}^{\dagger}\boldsymbol{G}$$

$$\begin{pmatrix} \boldsymbol{F} & \boldsymbol{G} \\ \boldsymbol{0} & \ldots \end{pmatrix} = \exp\left[\begin{pmatrix} i\boldsymbol{H}_0 & \boldsymbol{Q} \\ \boldsymbol{0} & i\boldsymbol{H}_0 - \lambda\boldsymbol{1} \end{pmatrix} T\right] \tag{25b}$$

with T chosen to be large enough to converge on the upper limit (in this equation, $\boldsymbol{H}_0$ was used instead of $\hat{H}_0$ for simplicity). Since all matrices appearing in this equation are very sparse and only their products are needed, this method is efficient and GPU-friendly. The auxiliary matrix method is implemented in the spin dynamics simulation package *Spinach*, where the capability is only limited by storing the resulting matrix, not by the superoperator dimension. [85].

Another attractive aspect of BRW theory is its readiness for integration with numerical simulation methods based on MD and DFT, as discussed above. For complete numerical analysis, the Redfield integral is evaluated without being opened up: [86,87]

$$\hat{\hat{R}} = -\left\langle \int_0^{\infty} \hat{\hat{H}}_1(0)\exp(-i\hat{\hat{H}}_0\tau)\hat{\hat{H}}_1(\tau)\exp(i\hat{\hat{H}}_0\tau)d\tau \right\rangle \tag{26}$$

To evaluate this integral, two further numerical convergence conditions are required: [86].

(a) The upper limit of the improper integral should satisfy:

$$\left\| \int_0^T (\ldots)d\tau \right\| >> \left\| \int_T^{\infty} (\ldots)d\tau \right\| \tag{27a}$$

for sufficiently long but finite time T.

(b) The squared standard deviation of the mean must be much smaller than the mean-squared:

$$\frac{1}{N}\left\|\langle(\ldots)(\ldots)^{\dagger}\rangle - \langle(\ldots)\rangle\langle(\ldots)^{\dagger}\rangle\right\| \ll \left\|\langle(\ldots)(\ldots)^{\dagger}\rangle\right\| \tag{27b}$$

where the dots in round brackets in eqs. (27) represent the integral in eq. (26) and N is the number of samples. In practice, a sufficiently long MD trajectory is required. It may be cut into enough statistically independent strips to satisfy eq. (27b), while each strip is simultaneously long enough to satisfy eq. (27a). This routine is implemented in the ngce.m function of *Spinach*, [88] where calculation of the scalar autocorrelation function can be avoided. While this method is gaining popularity with increasingly affordable MD and electronic structure calculations, particularly with neural network frame interpolation, [89] the procedure does not allow interpretation of the physics of the relaxation dynamics. For OE-DNP involving two hyperfine-coupled spin-1/2 centers, BRW theory has been validated for ^1H for several protonated solvents by Sezer and coworkers [73,74] and for ^{13}C for $CHCl_3$ by Orlando and coworkers [64], as described in the previous section. In case of $CHCl_3$, assuming that cross-relaxation is dominated by the scalar hyperfine interaction, the stochastic part of the Hamiltonian, discussed above, was given by $\hat{H}_1(t) = A(t) \bullet \hat{H}^{sc}$ with $\hat{H}^{sc}$ being the scalar part of the hyperfine Hamiltonian as defined in eq. (2a). The autocorrelation function was expressed as a linear combination of exponential decays with different weights and the cross-relaxation rate resulted in a Lorentzian spectral density function. Comparison of the BRW and Solomon approaches against variable-field experimental spectral densities and coupling factors did not show an obvious preference for either theory, also when rotational and translational correlation, respectively, were used to describe dipolar relaxation, see Fig. 5. The results supported the semi-classical approach used so far to model OE-DNP coupling factors. Nevertheless, the semi-classical approach becomes too simple for molecular systems with multiple nuclei and more complex dynamics.

One interesting insight from BRW theory is the potential advantage of cross-correlation between hyperfine interactions and chemical shift anisotropy in inducing DNP effects in the liquid-state at high magnetic fields. Cross-correlation is a consequence of synchronous tumbling of different interaction tensors caused by a common molecular motion, such as rotational diffusion. In NMR spectroscopy, cross-correlation between inter-nuclear dipolar interactions and chemical shielding tensors is responsible for the TROSY effect (TROSY = transverse relaxation-optimized spectroscopy) [90], used in the determination of structures of thousands of proteins. [91] Cross-correlation between g-tensors and

hyperfine tensors is capable of inducing CIDNP, [18] and is responsible for variation in the EPR line widths across hyperfine multiplets in liquids. [92] In terms of liquid-state DNP, Concilio and coworkers recently showed that the overall rate of the following process under MW irradiation: [93]

$$\widehat{S}_z \overset{MW}{\rightarrow} \widehat{S}_{\pm} \xrightarrow{HF-g} 2\widehat{S}_{\pm}\widehat{I}_z \overset{MW}{\rightarrow} 2\widehat{S}_z\widehat{I}_z \xrightarrow{HF-CSA} \widehat{I}_z \tag{28a}$$

actually increases with the magnetic field (here HF-*g* and HF-CSA represent cross-correlation between hyperfine-*g* tensor and hyperfine-chemical shift tensor, respectively), because the rate of the HF-*g* cross-correlation process increases with the field due to the combination of the electron Zeeman interaction with the field-independent $J(0)$ term in the spectral density: [93]

$$w(\widehat{S}_{\pm}\rightarrow 2\widehat{S}_{\pm}\widehat{I}_z) \propto [4J(0) + 3J(\omega_e)], J = \frac{\tau}{1+\omega_e^2\tau^2} \tag{28b}$$

To date, no experimental observations of this mechanism have yet been reported. However, it poses an interesting alternative for overcoming a common challenge in high-field liquid-state DNP.

2.7. Other mechanisms for DNP in liquids

Liquid-state OE-DNP becomes most efficient when molecular motions that modulate electron-nucleus hyperfine coupling occur on the same timescale as the electronic spin resonance frequency, which is in the sub-picosecond time scale. One way around this challenge might be to tune the electronic spin resonance frequency to lower frequencies by introducing a strong interaction, for instance a second electronic spin. The ensuing electron-electron exchange coupling is an isotropic interaction that is strong enough [94,95] and easily tunable, as it depends exponentially on the inter-electron distance [96]. In principle, it is easier to handle than zero-field splitting, which has much more complex anisotropic properties.

That is the idea behind the liquid-state JDNP mechanisms proposed by Concilio and coworkers, [93,97–100], who proposed theoretically that, in the presence of large inter-electron exchange coupling, a nuclear-state-dependent difference appears in the relaxation rates of electron singlet and triplet states. For a system with two electrons and a nucleus undergoing stochastic rotational diffusion, when the exchange coupling is set to $\omega_{ex} = \omega_e \pm \omega_n$ and the magnetic field is high enough that $(\omega_e \pm \omega_n)^2\tau^2 >> 1$, differences appear in the relaxation rates of the two-electron singlet and triplet manifolds according to BRW theory: [93,97–100]

$$R[\widehat{S}_{\beta}] - R[\widehat{S}_{\alpha}] \approx \frac{\aleph_{\Delta Z,\Delta A}B_0}{15}J(\omega_n) + \frac{\Delta^2_{\Delta A}}{36}J(2\omega_n) \tag{29a}$$

$$R[\widehat{T}_{\{\pm,0\},\beta}] - R[\widehat{T}_{\{\pm,0\},\alpha}] \approx \frac{\aleph_{\Delta Z,\Delta A}B_0}{15}J(\omega_n) - \frac{\Delta^2_{\Delta A}}{36}J(2\omega_n) \tag{29b}$$

where $\widehat{S}_{\beta}$ denotes the two-electron singlet state with nuclear spin β, $\widehat{T}_{+,\alpha}$ the upper projection of the two-electron triplet state with nuclear spin α, etc., Δ^2 is the second-rank norm-square and $\aleph_{A,B}$ is the scalar product of the interaction tensors [101]. Such differences generate non-equilibrium nuclear populations.

One key implication of such relaxation rate differences is that the nuclear polarization can be transiently driven out of equilibrium without external perturbations like MW irradiation, after the radicals are mixed into the NMR sample [97]. While it alone remains "single-shot" because electronic and nuclear populations will eventually reach equilibrium (essentially a TROSY-type cross-correlation process [102]), it has been theoretically proposed that the polarization can be continuously pumped into the nuclear subspace by field cycling. [98–100] So far, JDNP has not been observed experimentally, because its matching requires broadly but precisely sweepable superconducting magnets. Nevertheless, it remains as an attractive alternative to be explored for liquid-state hyperpolarized NMR.

An interesting alternative for hyperpolarizing viscous liquid-state samples has been recently explored in the context of ^{1}H DNP. In

Table 1
Isotropic *g* factors of selected polarizing agents obtained from CW-EPR spectra collected at 9.4 T. N@C_{60} or BDPA-d_{21} were used as internal standards. Reproduced with permission from [40].

Polarizing agent	Solvent	g_{iso}
BDPA-d_{21}	Toluene	2.0025
N@C_{60}	CCl_4	2.0022
N@C_{60}	$CHCl_3$	2.0022
Galvinoxyl	Toluene	2.0044
TEMPONE-^{15}N-d_{16}	Toluene	2.0059
TEMPONE-^{15}N-d_{16}	CCl_4	2.0062
TEMPONE-^{15}N-d_{16}	$CHCl_3$	2.0060
TEMPONE-^{15}N-d_{16}	H_2O	2.0057

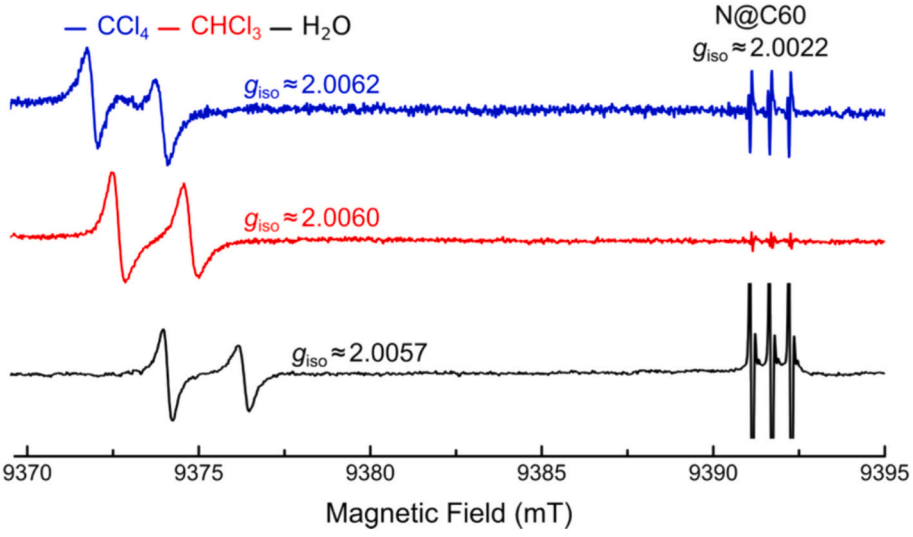

Fig. 6. 263 GHz CW EPR spectra of TEMPONE-^{15}N-d_{16} in CCl_4 (blue, $C \approx 2$ mM), $CHCl_3$ (red, $C \approx 2$ mM), and H_2O (black, $C \approx 10$ mM) with N@C_{60} as *g* factor reference, which was calibrated in-house to a carbon fiber [113]. Reproduced from [40]. (For interpretation of the references to colour in this figure legend, the reader is referred to the web version of this article.)

viscous media, where restricted molecular motion prevents complete averaging of the anisotropic dipolar electron-nuclear hyperfine interaction, the system can exhibit solid-effect (SE) DNP while retaining liquid-state NMR characteristics. [103–107] In this case, the polarizing agent's rotational correlation time is slow on the EPR timescale but still fast on the NMR timescale. The proposed SE-DNP hyperpolarization mechanism possesses analogy to its solid-state counterpart – initial direct transfer occurs from the polarizing agent to nearby nuclei by direct excitation of the zero- or double-quantum transitions, followed by polarization propagation via molecular diffusion as opposed to spin-diffusion in solids. [104] Besides a suitable molecular motion, SE-DNP in viscous liquids requires a narrow-line polarizing agent and high MW power, such that the forbidden transitions can be excited sufficiently. Detailed theoretical descriptions have successfully modelled SE-DNP behavior in these systems, [106,108] including a transition back to OE-DNP when a fast-tumbling radical (4-hydroxy-2,2,6,6-tetramethylpiperidin-1-oxyl; TEMPOL) is used to hyperpolarize a lipid bilayer [109].

3. Electronic saturation and the role of EPR in liquid-state OE-DNP

Optimization of OE-DNP enhancements requires EPR characterization of the polarizing agents, including knowledge of their saturation factor with the available MW B_{1e} at the sample position. This involves determination of the isotropic (average) g factor and hyperfine splittings of the polarizing agent in specific solvent environments, as well as their T_{1e} and T_{2e} at the OE-DNP magnetic field. In addition, estimation of the MW B_{1e} delivered by the specific hardware configuration is also required. To date, several studies have presented EPR measurements within liquid-state OE-DNP setups utilizing specialized probe heads with EPR capabilities. Alternatively, determination of g factors and saturation can be performed ex situ. An EPR-based approach of quantifying electronic saturation may rely on techniques such as CW EPR, pulsed EPR, or electron-electron double resonance (ELDOR). In contrast, an NMR-based approach estimates saturation based on paramagnetic shift changes of the analytes upon MW irradiation. These methods will be reviewed below.

3.1. Characterization of the polarizing agents

In the context of liquid-state OE-DNP, common polarizing agents are characterized by EPR linewidths on the order of a few MHz. Therefore, saturation of the electron spin resonance necessitates precise knowledge of radical g factors. At a magnetic field of 9.4 T, an offset of $\Delta g = 0.001$ from the free-electron g factor translates to ~13 MHz shift in the resonance frequency near 263 GHz. This shift already surpasses the spectral width ($\leq$ 1 MHz) of a typical CW gyrotron. [110–112] The EPR line shape, and subsequently the line width, results from several factors, including the g factor, hyperfine interaction, their anisotropies, the sample inhomogeneity, molecular dynamics, and electron spin relaxation times. Many of these parameters cannot be extracted from measurements at lower magnetic fields. Consequently, direct EPR measurements at the OE-DNP magnetic field becomes the most reliable way of determining optimal saturation conditions.

Characterization of polarizing agents at high magnetic field ($\geq$ 3 T) in the context of liquid-state OE-DNP has so far been focused on selected organic radicals (Scheme 2), particularly nitroxides [40,63,69,114–117]. Other radicals, such as BDPA [43] and galvinoxyl [39,40,118], have also sometimes been employed in high-field OE-DNP experiments. As evident from high-field EPR studies (Fig. 6), the radical isotropic g factors are solvent dependent. This effect is well-documented in the EPR literature and can arise from stabilization or destabilization of the singly-occupied molecular orbital (SOMO) of the radical due to differences in solvent polarity, solvation shell structure, or radical-solvent non-covalent interaction. [119–123] For example, Levien and

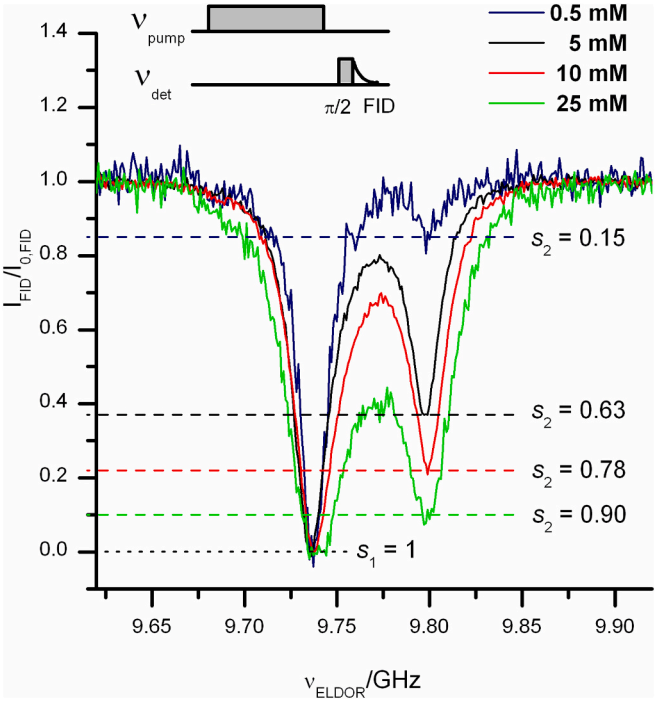

Fig. 7. ELDOR experiment for TEMPONE-^{15}N-d$_{16}$, which has two hyperfine lines, in water at room temperature at X-band frequency. The pulse sequence is depicted in the inset. The normalized EPR FID intensity of the hyperfine line at 9.74 GHz is plotted as a function of the frequency of the saturating pulse and for different concentrations of the radical. Adapted with permission from ref. [127].

coworkers reported isotropic g factors for TEMPONE-^{15}N-d$_{16}$ dissolved in CCl_4, $CHCl_3$, and H_2O, recorded using a 263 GHz EPR spectrometer and with either N@C$_{60}$ or BDPA-d$_{21}$ as internal g factor references (Fig. 6, Table 1). [40] The g factor of N@C$_{60}$ was calibrated at 263 GHz against carbon fiber [113], whereas that of BDPA-d$_{21}$ was taken from ref. [124]. In this case, solvent variation led to a shift of about 65 MHz (corresponding to 2.3 mT) in the EPR resonance frequency. This sample-dependent shift underscores the necessity of frequency-tunable MW sources or a sweepable NMR magnet for high-field liquid-state OE-DNP experiments.

3.2. Determination of saturation factors by EPR methods

The saturation factor is a critical parameter in OE-DNP, as it contributes multiplicatively with the coupling factor in determining the enhancement ε (eq.(4)). Therefore, a saturation factor close to unity can partially compensate for a weaker coupling factor. This is the case for polarizing agents such as BDPA or galvinoxyl, where small hyperfine couplings to ^{1}H result in a single, inhomogeneously broadened EPR line. Such an EPR profile is generally easier to saturate than the three-line EPR spectra of nitroxide radicals (or two-line if ^{15}N labeled). Additionally, better saturation is often encountered when the polarizing agent possesses relatively long T_{1e} and T_{2e} relaxation times. In this section, we review the current understanding of the saturation behavior of polarizing agents, with a focus on nitroxide radicals, which have been most extensively studied at both low and high magnetic fields.

For a spin-1/2 polarizing agent with a homogeneous EPR line that is continuously irradiated on-resonance, the OE-DNP saturation factor can be calculated from the Bloch equation as: [125]

$$s = \frac{S_0 - \langle \widehat{S}_z \rangle}{S_0} = 1 - \frac{1}{1 + \gamma_S^2 B_{1e}^2 T_{1e} T_{2e}} = \frac{\gamma_S^2 B_{1e}^2 T_{1e} T_{2e}}{1 + \gamma_S^2 B_{1e}^2 T_{1e} T_{2e}} \tag{30a}$$

where $\langle \hat{S}_z \rangle$ denotes the expectation value of the electron spin in z-direction along the external magnetic field, and S_0 is its value at thermal equilibrium. B_{1e} is the MW field strength, while T_{1e} and T_{2e} are the electron longitudinal and transverse relaxation times. The saturation factor takes values between 0 and 1, with unity corresponding to maximal saturation. If the electron spin is hyperfine coupled to nearby nuclear spins, pumping of one hyperfine transition can lead to partial saturation of the other transitions through Heisenberg spin exchange mediated by intermolecular radical-radical collision. At room temperature and in liquids, the nuclear spin ($T_{1n} \sim 0.1$–100 s) relaxes much more slowly than the electronic spin ($T_{1e} \sim 100$–1000 ns). Subsequently, the nuclear spin appears static on the timescale of electron spin relaxation, allowing the cross-relaxation rates to be approximated by a single exchange-induced rate, $w_{ex} = w_2 \approx w_0 = cK_x$, with c being the polarizing agent concentration and K_x being the concentration-normalized exchange rate. [126] Following this approximation, Türke and coworkers derived the analytical expression for the effective saturation factor s_{eff} of a perdeuterated, ^{15}N-enriched two-line nitroxide radical: [127,128]

$$s_{eff} = \frac{s_1 + s_2}{2} = \frac{\frac{1}{4}\gamma_e^2 B_{1e}^2 T_{2e}[2(w_e + w_n) + cK_x]}{\frac{1}{4}\gamma_e^2 B_{1e}^2 T_{2e}(4w_e + 2w_n + cK_x) + w_e[2(w_e + w_n) + cK_x]} \tag{30b}$$

Here, s_{eff} represents the average saturation of the individual EPR transitions, while $w_e = 1/2T_{1e}$ and $w_n = 1/2T_{1n}$ are the electronic and nuclear spin-lattice relaxation rates, respectively. Perdeuteration eliminates large hyperfine couplings to ^{1}H, such that the two ^{15}N hyperfine lines can be considered as homogeneously broadened. Similar, albeit more complex, expressions have also been derived for a three-line nitroxide radical (with ^{14}N) assuming full saturation of the irradiated transition. [65].

One method for directly measuring the effective saturation factor, s_{eff}, is electron-electron double resonance (ELDOR), which requires a pulse EPR instrument operating with two independent MW channels and a resonator, whose bandwidth is comparable to the radical spectral width. [127–129] During an ELDOR experiment, the radical is saturated with a long pulse (i.e., a pump) at a frequency offset from the detection frequency, while the EPR signal is detected at a fixed probe frequency. During the experiment, the pump frequency is swept stepwise across the full EPR spectrum of the polarizing agent (inset of Fig. 7). The saturation levels of each individual EPR transition, s_i, can be directly calculated by comparing the ELDOR effect, i.e., reduction of the signal intensity, with a reference background collected with the pump frequency set off-resonance (Fig. 7). The resultant s_{eff} is the arithmetic mean of s_i:

$$s_{eff} = \frac{1}{n}\sum_{i=1}^{n} s_i \tag{31}$$

To date, a few reports have applied ELDOR for quantifying the saturation factor of nitroxide radicals, including ^{15}N-labeled Frémy's salt at 0.35 T [128]; TEMPONE-^{15}N-d$_{16}$ (both e-^{15}N systems) at 0.35 T [127,130], 1.2 T [114,131], 3.4 T [69]; TEMPOL at 0.34 T [62,65]; fullerene nitroxide derivative (both e-^{14}N systems) at 0.34 T [62,65], 1.2 T [114]; BDPA at 1.2 T [131]; as well as galvinoxyl (both e-^{1}H systems) at 1.2 T [39]. Among these examples, ELDOR measurements at 0.34–3.4 T were performed "in situ" using the same instrument and cavity as for the corresponding OE-DNP experiments. In contrast, for high-field liquid-state OE-DNP, in situ characterization of the saturation factor has so far not been possible due to challenges in constructing suitable EPR/NMR probe heads.

Alternatively, the OE-DNP saturation factor can be calculated from eqs. (30a-30b) if T_{1e}, T_{2e}, and B_{1e} (and K_x if Heisenberg exchange is significant) are known or can be determined independently. As T_{1e} and T_{2e} of the polarizing agent only depend on the sample conditions and MW frequency, but not on B_{1e}, they can be measured ex situ with EPR instrumentation. When pulsed EPR is available, T_{1e} can be determined

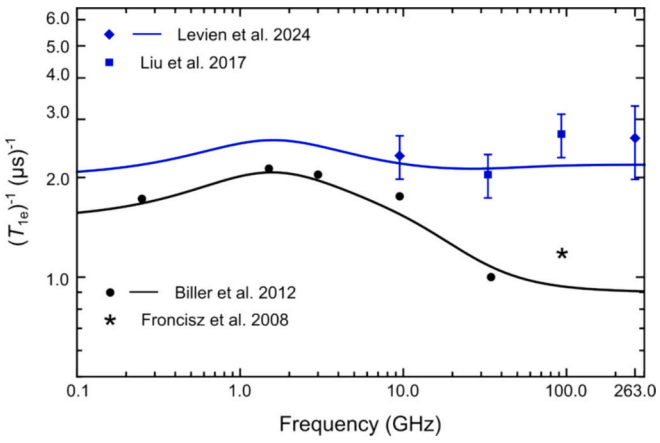

Fig. 8. T_{1e} of TEMPONE-^{15}N-d$_{16}$ in CCl_4 (blue) and TEMPONE in water (black) as functions of EPR resonance frequency. Markers represent experimental data points (diamond: ref. [40]; square: ref. [69]; circle: ref. [140]; asterisk: ref. [144]). Solid lines represent simulation (blue upper trace: ref. [40]; black lower trace: ref. [140]). Adapted from ref. [40].

by inversion recovery experiments in liquids at room temperature [40,69,127], whereas K_x, which is independent of the MW frequency, can be obtained at low frequencies. For radicals with homogeneously broadened EPR lines, T_{2e} may be extracted from the free induction decay. At high EPR fields and frequencies, however, pulse experiments present several challenges: first, OE-DNP is usually performed with high radical concentrations (≥ 5 mM), whereby T_{2e} approaches the timescale of EPR pulse lengths (10–50 ns); second, sample deoxygenation, crucial for achieving large T_{1e}, T_{2e}, and s_{eff}, complicates EPR sample preparation due to sample volume restrictions in MW cavities (10–50 nL for pulsed EPR at 9.4 T with resonant cavities). [40] Alternatively, T_{2e} can be determined from the EPR line width of CW EPR spectra. For a homogeneous, non-saturated EPR line, T_{2e} is given by: [132] [52]

$$T_{2e} = \frac{2}{\sqrt{3}\Delta B_{pp}\gamma_e} \tag{32}$$

where ΔB_{pp} is the peak-to-peak linewidth. Note that protons may inhomogeneously broaden the EPR line through hyperfine interactions. Consequently, most OE-DNP saturation studies with nitroxide radicals use perdeuterated species such as TEMPONE-d$_{16}$ or TEMPOL-d$_{16}$.

The product of the relaxation times, $T_{1e}T_{2e}$, can also be determined from a power-saturation experiment, where the peak-to-peak intensity I_{pp} of the CW-EPR signal derivative of an absorptive Lorentzian line is measured as a function of MW power $P_{MW} \sim B_{1e}^2$: [132]

$$I_{pp}(B_{1e}) = I_{pp}^0 \bullet B_{1e} \bullet \frac{1}{\left(1 + \gamma_S^2 B_{1e}^2 T_{1e} T_{2e}\right)^{3/2}} \tag{33}$$

where I_{pp}^0 is the slope in the linear regime of $I_{pp}(B_{1e})$ below saturation. Signal intensity is usually plotted against $\sqrt{P_{MW}}$, which gives rise to a linear increase below saturation, whereas the amplitude becomes proportional to $(P_{MW})^{-1}$, and therefore decreases, when strongly saturated. [115,133] Furthermore, it is also important to estimate the MW B_{1e} averaged over the sample volume in the OE-DNP setup. For a freely-propagating MW beam, B_{1e} can be estimated from the MW power. [134] In a MW cavity with quality factor Q, B_{1e} can be extracted from the Rabi oscillation, or from $B_{1e} = c\sqrt{Q \bullet P_{MW}}$ if the cavity conversion factor c is known. More generally, B_{1e} has been estimated indirectly from electromagnetic field simulations, [40,117,135–138] the details of which will not be discussed here.

Early examples of electron spin relaxation measurements in the context of high-field liquid-state OE-DNP were carried out by Prisner and coworkers. For instance, Prandolini and coworkers reported T_{2e} =

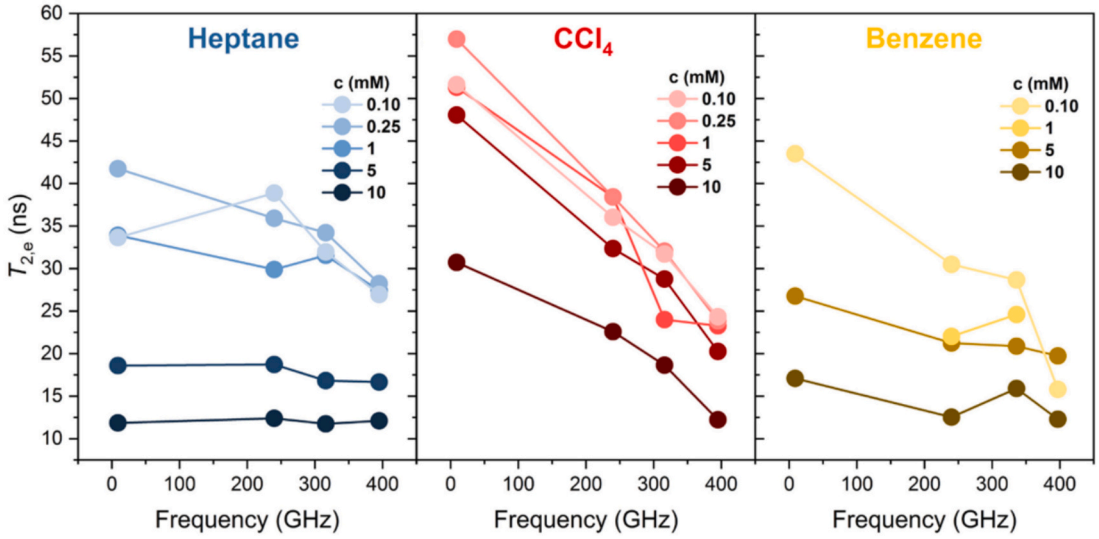

Fig. 9. T_{2e} of TEMPO in heptane, CCl_4, and benzene at various concentrations as functions of EPR resonance frequency. Error in T_{2e} was estimated to be 15%. Adapted with permission from ref. [117].

28 ns for a 0.6 M aqueous solution of TEMPOL-^{15}N at 9.2 T and room temperature, based on CW-EPR measurements collected directly using a DNP spectrometer equipped with a TE_{011} resonator operating at the same field. [116] The authors estimated $T_{1e} = 120$ ns based on $T_{1e}T_{2e} = 35 \times 10^{-16}$ s^2 obtained from power saturation experiments and a MW conversion factor of 1.0 mT/W^{-2} [115]. A similar method was applied to Fremy's salt in aqueous solution, yielding $T_{2e} \approx 140$ ns for the narrowest observed linewidth (0.5 G at concentrations near 200 μM) and $T_{1e} \sim$ 120–350 ns across a concentration range of 200 μM to 65 mM at 9.2 T, accounting for a Heisenberg exchange rate of $K_x = 1.3 \times 10^9$ s^{-1} between the ^{14}N hyperfine transitions. [139].

An example of extracting s in a non-resonant DNP probe head was recently reported by Levien and coworkers at 9.4 T. [40] In this study, T_{1e} and T_{2e} were measured ex situ in a 263 GHz EPR spectrometer, using either a TE_{011} or TE_{012} resonator for pulse measurements, which allowed MW pulses <100 ns, or a non-resonant probe head for CW experiments, providing a larger sample volume and better signal-to-noise. For 5–20 mM TEMPONE-^{15}N-d_{16} solutions in CCl_4, $CHCl_3$, and water, T_{2e} = 10–25 ns was obtained from the CW-EPR peak-to-peak linewidth following eq. (32), and T_{1e} = 200–400 ns was measured through inversion-recovery experiments. With $B_{1e} \sim 0.05$ mT estimated from electromagnetic field simulations and a molar Heisenberg exchange rate of $K_x = 2.5 \times 10^9$ M^{-1} s^{-1} [69], eq. (30b) led to $s \approx 0.3$, in good agreement with the value estimated from the DNP enhancement of CCl_4. Additionally, T_{1e} analysis at 263 GHz offered new insight into the electron spin relaxation theory, which predicts a flat field dependence of T_{1e} at high magnetic fields (Fig. 8). [140–142] Simulation of the T_{1e} field dependence revealed contributions from spin rotation, hyperfine anisotropy, g anisotropy, and thermally-activated processes. [40,143].

In the context of evaluating the performance of a non-resonant OE-DNP probe head, recent reports have characterized electron spin relaxation for 2,2,6,6-tetramethylpiperidin-1-oxyl (TEMPO) at multiple magnetic fields between 8 and 14.1 T. Based on B_{1e} calculated from the energy density of the incident MW beam, Dubroca and coworkers estimated $T_{1e}T_{2e} = 1.8 \times 10^{-15}$ s^2 for 10 mM TEMPO in n-pentane-d_{12}. [134] Orlando and coworkers obtained T_{2e} = 10–60 ns for 0.1–10 mM TEMPO in various solvents (CCl_4, benzene, and heptane) at 240 GHz, 316 (or 336) GHz, and 395 GHz, based on Lorentzian line widths from CW-EPR measurements using $T_2 = (\pi\gamma\Delta B_{avg})^{-1}$, where ΔB_{avg} represents the average linewidth of the three nitroxide hyperfine lines. [117] A general trend of decreasing T_{2e} with increasing magnetic field was observed (Fig. 9).

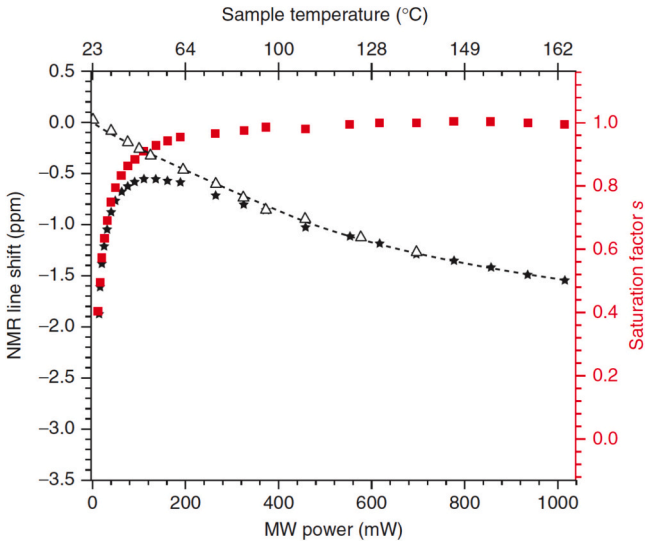

Fig. 10. Chemical shifts of pure water (triangles) and a water solution of 1 M TEMPOL (star), plotted against the incident MW power and sample temperature. The red squares represent the saturation factors calculated by subtracting the temperature-induced shift of neat water from the chemical shift of the TEMPOL-doped water under MW irradiation. Reproduced with permission from ref. [152]. (For interpretation of the references to colour in this figure legend, the reader is referred to the web version of this article.)

3.3. Exploration of pulsed microwave excitation

For solid-state DNP, many examples have explored the use of pulsed MW excitation to achieve superior enhancements. [145,146] So far, liquid-state pulsed OE-DNP has been investigated only at low magnetic fields (≤ 1.2 T). Early conceptualization was proposed by Alecci and Lurie [147], and detailed theoretical models have since been developed for the excitation scheme of a train of equally-spaced pulses with duration τ_p and repetition time τ_r, for systems with or without Heisenberg exchange. [148,149] In this framework, eqs. (4–5) remain valid, but requires an alternative description for the saturation factor, which is related to a combination of T_{1e}, T_{2e}, ω_e, $\delta\omega_e$ (resonance offset for electron), τ_p, τ_r, as well as the number of hyperfine transitions. For single-line, homogeneously broadened polarizing agents such as trityl,

theoretical analysis so far suggests that pulsed excitation is less efficient than CW excitation under the same average power, due to the reduced duty cycle. In contrast, for polarizing agents with inhomogeneously broadened and hyperfine-split EPR lines, pulsed excitation is expected to generate superior enhancements than CW if the electronic spins are coherently excited by multifrequency excitation – including short pulses with strong-B_{1e}, frequency-jumping, or polychromatic pulses generated by arbitrary waveform generators (AWG). [149,150] For instance, ~ 25-fold enhancement has been experimentally observed for a 1 mM aqueous solution of TEMPOL at 1.2 T using $\tau_p = 70$ ns and a 6.9% duty cycle in an ENDOR (ENDOR = electron nuclear double resonance) resonator, corresponding to a ~ 40% increase relative to the predicted CW OE-DNP enhancements acquired with the same average MW power. [150] Here, pulsing at τ_p close to T_{1e} and T_{2e} while providing sufficient power for electronic spin inversion, likely plays a significant role in pushing beyond the efficiency of CW irradiation. For high-field liquid-state OE-DNP, pulsed excitation schemes still remain unexplored due to technical challenges. Such schemes, however, might represent an avenue to optimize saturation factors in future applications.

3.4. Determination of saturation factors by NMR methods

When EPR-based methods are not accessible, the saturation factor can be determined from NMR measurements, based on the polarizing agent-induced isotropic paramagnetic shift and the suppression of such shift upon continuous irradiation of the EPR resonance. An early example of this approach was demonstrated by Wind and coworkers for studying the OE-DNP effect of metals, in which case the Knight shift of the metal nuclei induced by conducting electrons was suppressed when the EPR transition of these electrons were saturated. [151] Later, Prisner and coworkers adapted this method for use with liquid-state systems at high magnetic fields. [152] The authors monitored OE-DNP enhancements and NMR chemical shifts of an aqueous sample doped with 1 M TEMPOL-^{14}N at 9.2 T as a function of MW power, showing that a saturation level exceeding 0.9 could be achieved at MW powers >100 mW in a cavity. Importantly, thermally-induced chemical shifts were corrected by measuring neat water under identical MW conditions (Fig. 10, triangles). The same approach was adopted more recently by Kuzhelev, Denysenkov and coworkers for evaluating saturation for a series of nitroxide radicals based on ^{1}H chemical shift. [63,114,136].

4. High-field liquid-state OE-DNP instrumentation

In liquid-state OE-DNP, the polarizing agent is saturated on-resonance by MW irradiation, while the nuclei of interest are detected in situ through conventional NMR methods. Optimal OE-DNP performance therefore requires hardware design that can efficiently deliver MW to liquid samples, while concomitantly enabling efficient radio frequency (RF) excitation and detection. On the MW side, eqs. (30a) and (30b) provide an estimate of the required B_{1e} for maximizing electron spin saturation. As an example, for 25 mM TEMPONE-^{15}N-d$_{16}$ dissolved in CCl_4 at 9.4 T, which is characterized by $T_{1e} \approx 380$ ns, $T_{2e} \approx 25$ ns, and $K_x \approx 2.5 \times 10^9$ s^{-1} M^{-1}, [40] $B_{1e} \gtrsim 0.3$ mT is required to attain an effective saturation factor of $s_{eff} \gtrsim 0.9$. Achieving such MW field strength at sub-terahertz frequencies (e.g., $\nu(e^-) = 263$ GHz at 9.4 T) in liquids, while preserving NMR sensitivity and field homogeneity, presents a significant challenge. In this section, we discuss the implications imposed by MW penetration in liquids, review available MW sources, and summarize proposed strategies for constructing high-field liquid-state OE-DNP probe heads.

4.1. Microwave penetration in liquids

One major technical bottleneck of implementing liquid-state OE-DNP with millimeter and sub-millimeter MWs arises from the dielectric loss and sample heating associated with the electric field component of the MW at the sample position. These effects reduce the saturation factor while imposing potential constraint on sample stability and homogeneity. The propagation of an electromagnetic wave at a given frequency through a sample is determined by the dielectric properties of the medium. Attenuation of the MW field amplitude in a dielectric lossy medium follows an exponential decay with a characteristic decay coefficient α, called absorption coefficient, and its inverse called penetration depth d. [153] These quantities depend on the MW frequency ν and the relative permittivity ($\varepsilon_r = \varepsilon/\varepsilon_0$) of the medium $\varepsilon_r = \varepsilon_r' + i\,\varepsilon_r''$, where ε_0 and ε are the absolute electric permittivity in vacuum and the medium, respectively. Dielectric losses are usually quantified by the loss tangent, $\tan\delta = \varepsilon_r''/\varepsilon_r'$, which together with α becomes zero in a perfect lossless medium ($\varepsilon_r'' = 0$).The MW wavelength in the medium, λ_{MW}, is determined by the vacuum wavelength λ_0 and the refractive index of the medium n following $\lambda_{MW} = \lambda_0/n$. For example, λ_{MW} lies in the range of 0.8 to 0.5 mm for typical OE-DNP solvents, such as CCl_4, $CHCl_3$, at 9.4 T.

When MW propagate as a free wave, the electric and magnetic field components are orthogonal and in phase. The instantaneous energy density in a region of space is equally divided between the two fields. In contrast, when a MW forms a standing wave, the two fields become spatially and temporally separated: at the position of a magnetic field maximum, the electric field becomes zero. Under such condition, there is no energy flow, but only local accumulation and dissipation. This principle provides the basis of the use of resonant structures, which can mitigate MW loss by positioning the sample at the magnetic field maxima (section 4.3.1). To quantify dielectric constants and losses in an OE-DNP probe design, Scott and coworkers [154], as well as Orlando and coworkers [117] recently reported measurements of reflection interference patterns using a Fabry-Pérot interferometer. From the reflection patterns the refractive index n and the extinction coefficient k were extracted, allowing determination of the loss tangent. These studies investigated several solvents and sample tube materials, including CCl_4, pentane, hexane, toluene, fused quartz (or fused silica), FEP, and sapphire. Alternatively, high-frequency dielectric properties of a medium can be extrapolated from lower-frequency data using a Debye model. [155,156] Subsequently, MW propagation inside an OE-DNP probe head can be evaluated by finite-element numerical electromagnetic wave simulations, for instance, using commercial software like CST Microwave Studio®. Table 2 summarizes the dielectric properties and MW penetration depths of selected media relevant for high-field liquid-state OE-DNP. Importantly, the MW penetration depth d in liquids depends dramatically on the solvent. In non-polar solvents like CCl_4, the penetration depth at 263 GHz can reach few centimeters, while it reduces to less than 1 mm in $CHCl_3$, and to approximately 100 μm in water.

Table 2
Dielectric properties of selected materials and solvents relevant for high-field liquid-state OE-DNP, including the real part of the relative dielectric constant (ε_r'), the loss tangent ($\tan\delta$), absorption coefficient (α) and penetration depth (d) at MW frequencies of 263 and 395 GHz. For CCl_4 and $CHCl_3$, data at 263 GHz was extrapolated from experimental dielectric constants at 3 GHz using the Debye model. [40] Data for water at 264 GHz was taken from previously reported experimental values. [155] The derived data corresponds to experimental values determined at 30 °C. Data at 395 GHz was experimentally determined at 20–25 °C. [117].

Medium	ν_{MW} (GHz)	ε'	$\tan\delta$	α (cm^{-1})	d (cm)
Fused quartz	263	3.74	0.00037	–	–
Fused quartz	395	4.16	0.00098	0.338	3.0
FEP	395	2.13	0.00157	0.278	3.6
H_2O	264	5.36	1.20	~ 105	~ 0.01
$CHCl_3$	263	3.52	0.122	~ 12	~ 0.08
CCl_4	263	2.17	0.00041	~ 0.3	~ 3.4
CCl_4	395	2.13	0.00507	0.895	1.1
Toluene	395	2.43	0.00969	1.957	0.5
Pentane	395	1.96	0.00153	0.248	4.0
Hexane	395	2.07	0.00183	0.315	3.2

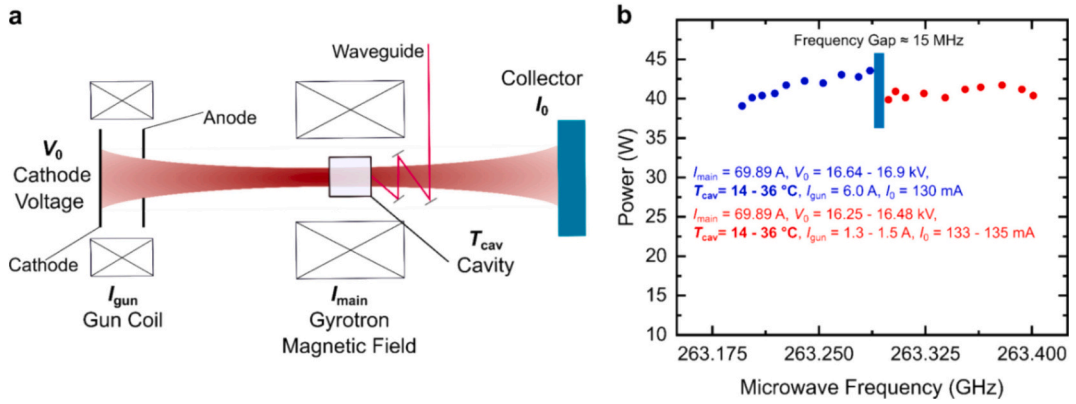

Fig. 11. (a) Schematic of a gyrotron tube; (b) Average output power of a frequency tunable gyrotron as a function of output frequency, which is varied by adjusting the cathode voltage, gun coil current, cavity temperature, and the collector current. Reproduced from ref. [40].

Correspondingly, MW absorption increases for samples with stronger polarity, which relates to the amount of heat produced in the sample, posing constraints on the OE-DNP experiments of these samples.

4.2. Microwave sources

To date, high-field OE-DNP experiments have mainly been performed with three types of MW sources: solid-state oscillator sources, extended interaction oscillators or klystron amplifiers (EIO or EIA), and gyrotrons. In this section, we summarize the advantages and limitations of each type, and refer the readers to a recently published review for a more detailed discussion. [157] Solid-state sources mainly consist of voltage-controlled oscillators stabilized by phase-locked loops. [158–160] They offer broad frequency tunability (up to tens of GHz), and the sub-THz frequency range required for high-field OE-DNP can be generated in an amplifier-multiplier chain supplied with lower-frequency sources. While earlier designs suffered from a large frequency drift, thus preventing efficient excitation of polarizing agents with narrow EPR lines ($<$ 0.1 mT), recent variants offer superior frequency stability. [45,115,116] One additional benefit of solid-state sources is the compatibility with pulse shaping, for instance, by combining or replacing the low-frequency source with an arbitrary-waveform generator. [161,162] However, the power output of solid-state sources is limited ($\leq$ 250–300 mW at 263 GHz), thus posing a significant challenge for applications in liquid-state OE-DNP unless combined with MW cavities. EIO/EIA are attractive alternatives that rely on electron beam-wave interaction, in which an accelerated electron beam transfers energy to a resonant MW field. Whereas the EIO contains an internal oscillator, the EIA amplifies MW produced by an external source, often a solid-state generator. EIO/EIA are compact and possess relatively large bandwidth (up to several GHz), [163,164] although they require efficient cooling during operation. Typical delivered power is less than 30 W. [157] Additionally, a recent report described the use of a traveling wave tube (TWT) amplifier in conjunction with a solid-state source for DNP at 140 GHz, achieving 4.4 W output power and about 1 GHz frequency tuning range. [165].

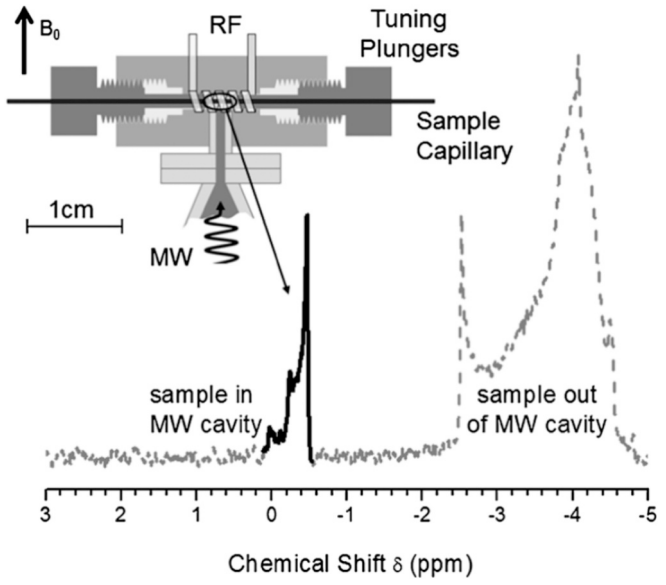

Fig. 12. Upper left: schematic of the cylindrical helical resonator for performing liquid-state OE-DNP at ~9 T. [115] B_0 represents the external magnetic field direction. Lower right: exemplary ^{1}H OE-DNP spectrum of water doped with TEMPOL. Note the strong signal from sample outside the MW cavity. Reproduced with permission from ref. [152].

Gyrotrons are currently the most powerful MW sources implemented in DNP, delivering continuous power output up to 50 W. [166] They have been adopted for liquid-state OE-DNP, where high power is required to generate sufficiently strong B_{1e} [40,46,137,167], as well as for solid-state DNP applications. [168] In a gyrotron, MW is generated by the energy exchange between a resonant cavity and an azimuthally accelerated electron beam induced by its cyclotron motion inside the cavity in a static magnetic field. This differs from the mechanism of an EIO/EIA, where the electron velocity is modulated along the electron beam axis. Compared to other sources, one key limitation of gyrotrons is their relatively restricted frequency tunability while maintaining constant output mode and power. Most gyrotrons operate at a fixed frequency, which may require adjustment of the NMR main magnetic field to access the EPR resonance of different polarizing agents. Nevertheless, frequency-tunable gyrotrons operating in the sub-THz range have been developed, allowing 0.5–1.5 GHz frequency variation at average output power $>$ 10 W. [40,169] In these cases, frequency tunability can be achieved by varying the operating voltage, gun coil and collector currents, as well as the temperature of the broadband cavity (Fig. 11). Another challenge for gyrotron-based DNP systems is the high demands for installation and maintenance. Apart from dedicated cooling infrastructure for the active MW components, gyrotron operation relies on superconducting magnets, which requires additional cryogenic cooling.

4.3. OE-DNP probe head designs

4.3.1. Resonant probe head

MW irradiation into an OE-DNP probe can be optimized by the use of MW resonant structures. A resonator concentrates energy at specific spatial locations by forming standing waves, thus promoting B_{1e}. The separation of electric and magnetic fields further reduces sample heat-

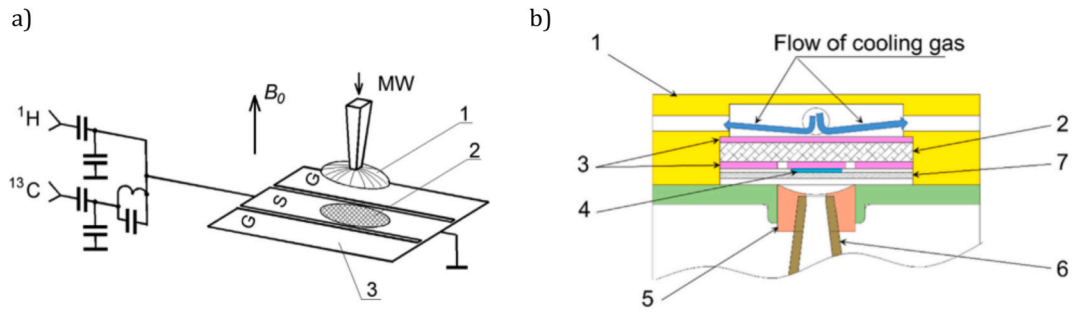

Fig. 13. (a) Schematics of the probe head capable to excite the liquid sample at 3 frequencies simultaneously: $\nu(^1\text{H}) = 400$ MHz, $\nu(^{13}\text{C}) = 100$ MHz, and ν(electron) = 263 GHz. 1- elliptical mirror; 2- sample; 3- stripes of the coplanar line (GSG: ground-signal-ground). Capacitors at the inputs of the channels are used to tune and match the resonance circuits. The C-L parallel circuit in the ^{13}C channel is a notch-filter tuned to 400 MHz. (b) Detailed design of the triple resonance structure. 1- housing, 2- ceramic AlN substrate, 3- copper/gold layer (the lower one is used as the coplanar stripline and the flat mirror of the FP, the higher one is used as ground) 4- sample, 5- elliptical mirror of the FP resonator, 6- mw waveguide taper and iris, 7- quartz cover plate for the sample. Adapted with permission from ref. [136]. (For interpretation of the references to colour in this figure legend, the reader is referred to the web version of this article.)

ing. On the other hand, resonator dimensions and sample positioning are limited by the MW wavelength, and the presence of metallic components can adversely affect the static NMR magnetic field homogeneity. Nevertheless, depending on the application, resonators can be advantageous for maximizing electronic saturation, particularly in solvents with high dielectric losses such as water.

Initial high-field liquid-state OE-DNP probe designs predominantly relied on resonant cavities. Pioneering developments were carried out by Griffin as well as Prisner and coworkers. One such design is a single-mode cylindrical helical resonator originally developed by Griffin and coworkers for operation at 140 GHz/5 T [124], and later adapted by Prisner and coworkers at 260 GHz/9 T (Fig. 12) [115]. In this configuration, the helical structure serves as both the MW resonator (supporting

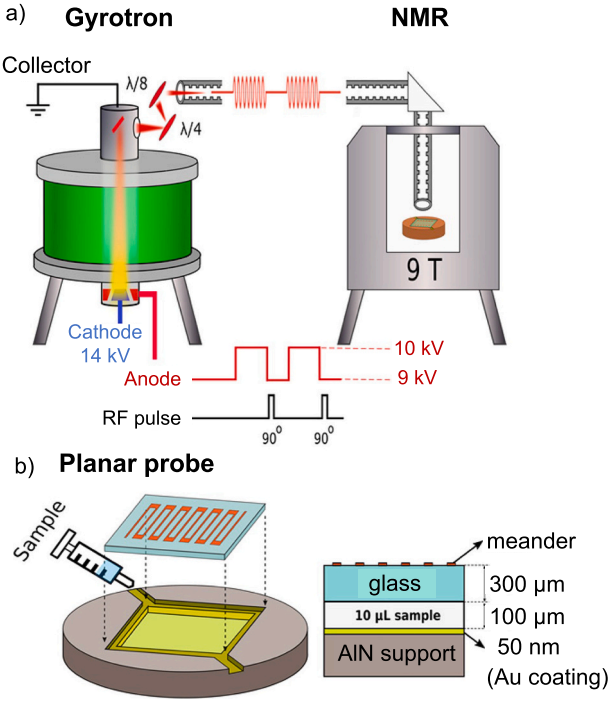

Fig. 14. (a) Schematic of a liquid-state OE-DNP spectrometer at 9.2 T. MW is delivered from a triode-gun gyrotron into the DNP probe head through a corrugated waveguide, with polarization adjusted by the $\lambda/4$ and $\lambda/8$ rotating grooved mirrors. The gyrotron output can be synchronized with the NMR acquisition, as shown by the pulse scheme. (b) Schematic of the planar probe. The red trace represents the meander RF planar coil. Adapted with permission from ref. [138]. (For interpretation of the references to colour in this figure legend, the reader is referred to the web version of this article.)

TE_{011} or TE_{012}-modes) and the RF coil for NMR detection. The resonator can be tuned by moving the two plungers positioned at either end of the helix, while coupling to MW waveguide is achieved through a centered elliptical iris. For measurement at ~260 GHz, the sample is loaded in a quartz capillary with inner diameter of 20–100 μm, corresponding to an effective sample volume of ~0.5–35 nL. [46,114,116,152] Owing to the high conversion factor and high quality factor (Q ~ 600–650 when unloaded) of the cavity [115], $B_{1e} \approx 0.15$ mT was achieved using only 110 mW of MW power [46], enabling efficient saturation of polarizing agents such as nitroxide radicals (see Section 3). In addition, this probe head is integrated with the capability of EPR detection, including a field-modulation coil. [45,115] This is a significant advantage for developing OE-DNP methodology, as it allows measurement of the EPR spectrum and provides access to the saturation factor in situ. The design of the cylindrical helical resonator was later adopted by Zhang and coworkers in a DNP setup operating at 5 T. [165].

An alternative probe head design developed by Prisner and coworkers is based on the principle of Fabry-Pérot interferometry. [135,136,170] Fabry-Pérot interferometers (or resonators) consists of two metal mirrors between which standing wave is formed by interference. [171] While operating efficiently in the quasi-optical regime, these resonators support less confined electromagnetic field modes than a cylindrical cavity. Nevertheless, Fabry-Pérot resonators can accommodate larger sample volumes, making them advantageous for liquid-state OE-DNP compared to conventional EPR cylindrical cavities. Specifically, Denysenkov and coworkers designed a Fabry-Pérot resonator (Fig. 13) comprising a spherical mirror coupled to the MW waveguide and a flat stripline that serves as both the resonator mirror and a dual-channel RF probe for ^{1}H and ^{13}C NMR operation. [135] [136] The resonator can accommodate sample volumes of ~100–200 nL and produces large OE-DNP enhancements, particularly for strongly polar samples such as aqueous solutions. [75] Compared to the cylindrical resonator, the Fabry-Pérot design also enables improved sample cooling.

Recently, Smirnov and coworkers demonstrated a photonic band-gap (PBG) resonator [172–175], which was constructed from periodically stacked discs with alternating dielectric constants. In this design, local MW B_{1e} amplification is achieved by breaking the periodicity at the flat sample position. [172] These resonators can reach high quality factors (Q ≈ 1500 when unloaded [164]) and are compatible with microliter sample volumes, thus offering potential advantages over cylindrical and Fabry-Pérot resonators. So far, the highest field at which a PBG resonator has been demonstrated is 7 T, enabling proof-of-principle continuous-wave liquid-state ^{31}P OE-DNP on 1 μL toluene solution of PPh_3 doped with BDPA. [175] It should be noted, however, that PBG resonators require precisely-manufactured dielectric discs with thicknesses of $(2n + 1)\lambda/4$ (where λ is the MW wavelength in each dielectric medium) and diameters significantly larger than the thicknesses. This

could potentially pose practical challenges in fabrication when moving to higher fields.

While resonant probe heads have displayed the largest enhancements for high-field liquid-state OE-DNP (e.g. $\varepsilon(^{13}C, CCl_4) = 430 \pm 50$ at 9.4 T [114]), and have been instrumental in understanding the OE-DNP mechanisms, they also suffer from notable limitations. The presence of conductive materials near the active sample volume degrades magnetic field homogeneity, leading to NMR line broadening (for instance, on the ppm-level for ^{1}H and ^{13}C at 9.4 T [63,75,114]). Furthermore, resonator dimensions and the electric field distribution restrict the sample volume to the sub-μL range [115,135,136], often necessitating isotopic enrichment for measuring low-abundant nuclei like ^{13}C. [136].

4.3.2. Non-resonant probe heads

One alternative approach for achieving larger sample volumes in high-field liquid-state OE-DNP is the use of non-resonant probe heads. One such design was developed by Yoon and coworkers at 9.2 T, utilizing a planar probe capable of ^{1}H and ^{31}P detection (Fig. 14). [138] The planar probe consists of a layer of gold-coated aluminum nitride (AlN) support and fused silica glass, with the liquid sample confined in between, leading to an active sample volume of approximately 10 μL. NMR excitation and detection are performed by a meander planar RF coil placed on the glass cover. Despite the non-resonant configuration, this probe head delivers strong B_{1e} at high MW power (~ 0.25 mT at 70 W input), while efficient heat dissipation is enabled by high thermal conductivity of the support. As a result, enhancements of $\varepsilon(^{1}H, H_2O) = -10$ and $\varepsilon(^{31}P, P(C_6H_5)_3; PPh_3) = 200$ were reported. However, substantial NMR line broadening on the order of ~10 ppm was observed under DNP, which poses issues for applications in liquid-state high resolution NMR. A similar design was reported by Annino and coworkers, consisting of an RF transducer for NMR detection and a grating polarizer, which is partially transparent to MW and acts as a Fabry-Pérot resonator. [176,177] Nevertheless, the setup still contains conductive material in the sample vicinity.

Another non-resonant probe head design was reported by Dubroca and coworkers at 14.1 T ($\nu(e^-) = 395$ GHz, $\nu(^{1}H) = 600$ MHz, $\nu(^{13}C) = 150$ MHz). [178] Compared to a conventional liquid-state NMR probe, a waveguide is positioned right below the sample compartment, which houses the sample tube (3 mm outer diameter; made of fluorinated ethylene propylene (FEP) or quartz [117]) and the RF coils. MW is directed onto the sample tube from the bottom, and the beam polarization is controlled by a Martin-Puplett interferometer placed between the gyrotron and the probe head. During DNP operation, sample cooling is achieved by a cold nitrogen gas flow through the waveguide. Electromagnetic wave simulations identified $B_{1e} = 0.04$ mT in a CCl_4–^{13}C/TEMPO sample when 12 W was provided by the gyrotron source. [117] This design accommodates sample volume of 50–100 μL and has enabled enhancements of $\varepsilon(^{31}P) = 160$ for PPh_3 in deuterated benzene, and $\varepsilon(^{13}C) = 70$ for $CHCl_3$ diluted in n-pentane-d_{12}. [134,137] However, due to the specific sample geometry, measurements with this setup have been limited to solvents with very low polarity, such as benzene, pentane, and hexane. NMR linewidth reported so far varies from tens of Hz to several ppm for ^{13}C and ^{31}P.

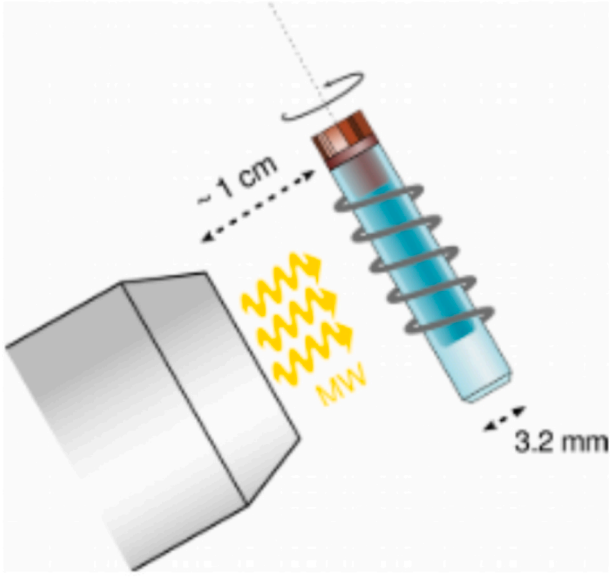

Fig. 15. Sketch of the MAS-DNP probe head. Adapted with permission from ref. [114]. See ref. [166] for more details about the setup.

One approach introduced by Yoon [138] and Dubroca [137] for alleviating sample heating in non-resonant probe heads is through the use of circularly instead of linearly polarized MW excitation. For a linearly polarized MW field, only one of the two circularly polarized MW B_{1e} components couples with the electron spin transition [179,180], such that only half of the power of the linearly polarized field contributes to EPR saturation of the sample. In contrast, circularly polarized MW propagating along the magnetic field axis can, in principle, achieve equivalent OE-DNP enhancements with only half the power. In practice, Dubroca and coworkers reported a 40% increase in enhancement over linear polarization at identical MW power, with the deviation from the ideal case attributed to polarization loss within the probehead. [137].

Finally, high-field liquid-state OE-DNP can also be performed using commercial MAS solid state DNP hardware. This idea was first demonstrated by Orlando and coworkers at 14.1 T [114] and subsequently adopted at 9.4 T by Rao and coworkers [181–183]. MAS-DNP setups typically employ a single RF solenoid coil connected to multiple tuning channels, [166] and the coil geometry can be designed to function as a diffraction grating to improve MW exposure of the sample. [166] In this approach, liquid samples are loaded into sapphire solid-state rotors (3.2 mm outer diameter) and irradiated by MW propagating orthogonally to the rotor axis (Fig. 15). Sample temperature is regulated by a combination of variable temperature nitrogen gas flow (100−200 K), as well as bearing and drive nitrogen gas flows (both ~298 K). To minimize temperature gradients, the sample volume is limited to 10–25 μL, and MAS rates of 1–8 kHz are employed. Specifically, spinning distributes the liquid as a thin film along the rotor wall, thereby improving MW penetration through the sample. This approach takes advantage of established DNP hardware, thus, in principle, is compatible with modern NMR-DNP methodology, including multi-channel and multi-dimensional experiments. It further allows simultaneous interrogation of solid-state and liquid-state samples [183] (see section 5). Nevertheless, the poor saturation factor (estimated to be around 0.1 for TEMPONE-^{15}N-d_{16} in CCl_4 and $CHCl_3$ [114]) limits the achievable enhancements. For neat $CHCl_3$ doped with TEMPONE-^{15}N-d_{16}, $\varepsilon(^{13}C) = 51$ and 18 have been reported at 9.4 and 14.1 T, respectively. In comparison, $\varepsilon(^{13}C) = 320 \pm 60$ was obtained at 9.4 T for neat $CHCl_3$ using the cylindrical helical resonator described in Fig. 12.

4.3.3. NMR-optimized high-field liquid-state OE-DNP setup

To benefit from the advantages of non-resonant probe head designs – namely larger sample volume and superior NMR magnetic field homogeneity – Bennati and coworkers recently reported a high-field liquid-state OE-DNP setup that combines optimized NMR performance with improved MW saturation (Fig. 16). [39,40,184] The setup comprises a modified commercial two-channel liquid-state NMR probe (Bruker) and a frequency-tunable gyrotron as the MW source. In this probe, linearly-polarized MW is directed onto the sample tube from the side by a set of four gold-coated Macor® ceramic mirrors (M1-M4 in Fig. 16). Mirror M3 is specifically designed to spread the MW beam profile along the longitudinal dimension of the sample tube, which is situated in the center of two sets of saddle coils as in conventional liquid-state NMR. Importantly, mirrors M3 and M4, situated on either side of the sample, act

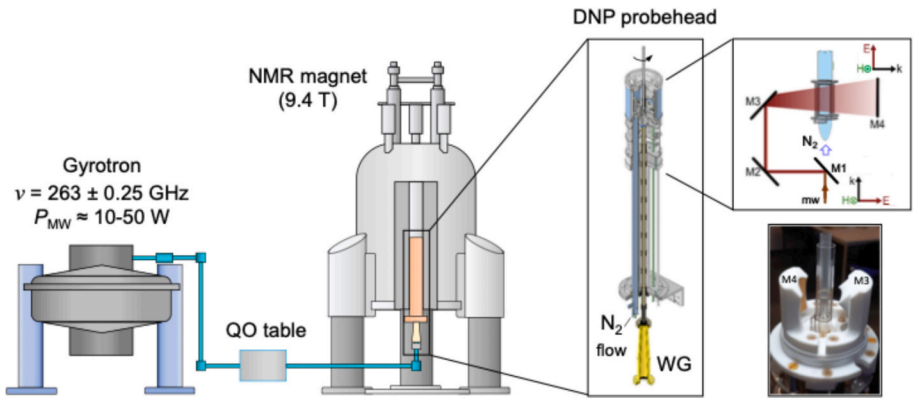

Fig. 16. Schematic of an NMR-optimized liquid-state OE-DNP setup at 9.4 T. [40] The expanded views on the right side provide details on the probe head design, including MW beam path, MW propagation vector (k), linearly polarized magnetic (H) and electric (E) field vectors, sample configuration, and the cooling scheme. WG marks the waveguide. M1, M2, M3 and M4 indicate gold-coated Macor® mirrors. (For interpretation of the references to colour in this figure legend, the reader is referred to the web version of this article.)

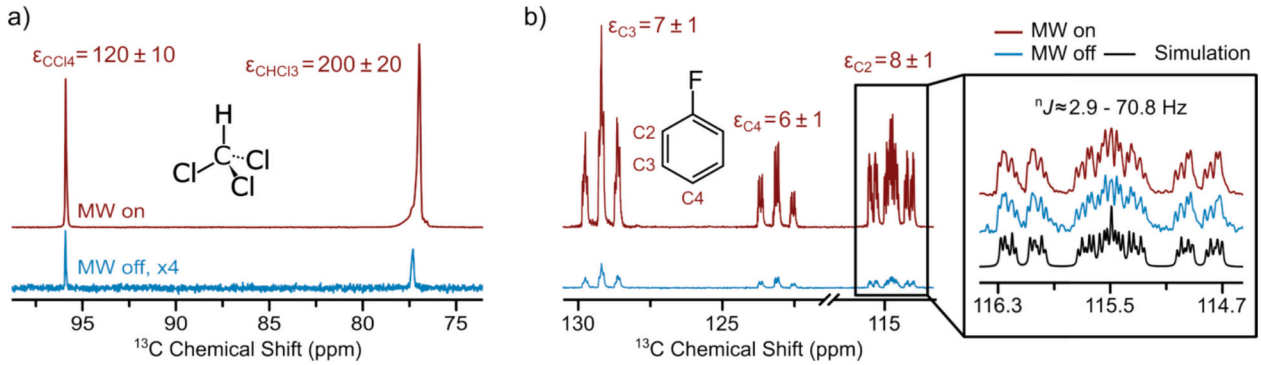

Fig. 17. OE-DNP enhanced ^{13}C NMR spectra and ^{13}C enhancements of CCl_4 solutions of (a) 0.2 M $CHCl_3$-^{13}C and (b) 0.5 M fluorobenzene-$^{13}C_6$ doped with TEMPONE-^{15}N-d_{16} at 9.4 T. Red and blue traces represent spectra collected under DNP and thermal Boltzmann conditions, respectively. Black trace in (b) represents simulation. Insets display chemical structures of the compounds. Adapted from ref. [40]. (For interpretation of the references to colour in this figure legend, the reader is referred to the web version of this article.)

Table 3
Electron-to-nucleus ratio of gyromagnetic ratios for different nuclei.

Nuclei	$\lvert\gamma_e\rvert/\gamma_n$
^{13}C	2617
^{1}H	658
^{19}F	699
^{31}P	1624

together with the quartz sample and shielding tubes as a series of low-Q quasi-Fabry-Pérot resonators, whereby interference of the incident and reflected MW beam led to a B_{1e} increase. [40,184] Particularly, electromagnetic field simulation estimated $B_{1e} \approx 0.05$ mT for neat CCl_4 doped with TEMPONE-^{15}N-d_{16} when 50 W continuous MW irradiation was employed, corresponding to $\varepsilon(^{13}C, CCl_4) = 120 \pm 10$ and $s \approx 0.3$.

To minimize sample heating and improve MW penetration, the liquid sample is confined between two concentric quartz tubes, resulting in a sample thickness controllable in the range 25–75 μm, depending on the sample dielectric loss. This probe head design is compatible with an effective irradiated sample volume of approximately 6–20 μL, achieved through 20 Hz spinning of the sample tube assembly, which is further cooled by cold nitrogen gas flow for temperature regulation. Altogether, these measures enable sample temperature stabilization between 190 and 340 K with a gradient of ±10–20 K during OE-DNP experiments. Due to controlled sample heating and superior magnetic field homogeneity, this probe head design enables ^{13}C linewidths of ~6 Hz for CCl_4 and ~16 Hz for $CHCl_3$ under OE-DNP for a CCl_4 solution of $CHCl_3$-^{13}C doped with TEMPONE-^{15}N-d_{16} (Fig. 17a). Furthermore, ^{13}C—^{13}C J-coupling constants as small as ~3 Hz can be resolved for fluorobenzene-$^{13}C_6$ when hyperpolarized with the same polarizing agent (Fig. 17b). [40] A further feature of this setup is its compatibility with modern multidimensional NMR methodology, including 2D correlation and coherence transfer experiments. Representative examples of these experiments will be discussed in the following section.

5. Experimental demonstrations of high-field liquid-state OE-DNP

To date, high-field liquid-state OE-DNP has been most extensively studied for ^{13}C and ^{1}H. Recent studies have further expanded the scope of the method to include ^{19}F as well as ^{31}P. In this section, we review the OE-DNP performance of ^{13}C, ^{1}H, ^{19}F, and ^{31}P at high fields, firstly from a mechanistic point of view (section 5.1), and secondly in terms of application to practically relevant systems (section 5.2). The maximal OE-DNP enhancements theoretically achievable are proportional to the ratio of electronic and nuclear gyromagnetic ratios (eq. (4)), which are listed in Table 3. Liquid-state OE-DNP has also been explored for other nuclei, such as ^{15}N at 5 T [43] and 0.33 T [185], ^{205}Tl at 0.34–1.32 T [186], ^{23}Na at 0.35 T [187], ^{29}Si at 0.33 T [188], as well as ^{2}H [189], ^{7}Li [190–192], ^{119}Sn [193] at around 7 mT. However, to date, knowledge of these systems is more limited, and will not be discussed in this review.

5.1. High-field liquid-state OE-DNP performance of selected nuclei

5.1.1. Carbon-13

Carbon-13 NMR provides crucial information in structural elucidation of organic molecules and biomacromolecules by directly reporting on the carbon skeleton, while also being beneficial for resolving complex mixtures due to chemical shift dispersion. However, compared to high gamma nuclei like ^{1}H and ^{19}F, ^{13}C suffers from additional sensitivity penalties. As the only NMR-active isotope of carbon, ^{13}C has 1.1% natural abundance, a gyromagnetic ratio 25% of that of ^{1}H, and longer T_1 relaxation times as compared to ^{1}H. Subsequently, 2D and higher-dimensional ^{13}C—^{13}C correlation spectroscopy often requires isotopic enrichment, or becomes prohibitively time-consuming. ^{13}C has a theoretical maximum OE-DNP enhancement of 2617 (Table 3). If even only partially achieved, such an enhancement would compensate for the lower gyromagnetic ratio and natural abundance, or even surpass the sensitivity of conventional ^{1}H NMR. As a result, ^{13}C has been the subject of considerable OE-DNP investigation since the 1960s. Our current knowledge of ^{13}C OE-DNP in the liquid-state reveals promise for high-field NMR ($\geq$ 9.4 T) thanks to efficient scalar-driven electron-nuclear cross-relaxation. In the next part (section 5.1.1.1), we first discuss the model systems CCl_4 and $CHCl_3$, which have been the most thoroughly studied. Subsequently (section 5.1.1.2), we review the ^{13}C DNP performance of molecules with other carbon functionalities. Overall, these reports provide guidelines for elucidating the mechanism and expanding the application of OE-DNP, for instance, in designing hyperpolarized molecular probes, similar to what has been performed with other hyperpolarization techniques. [36,194–196].

5.1.1.1. The CCl_4 and $CHCl_3$ model systems. CCl_4 and $CHCl_3$ have long served as prototypical systems for OE-DNP. Extensive investigations have examined the leakage, saturation, and coupling factors, as well as the spectral densities governing the relaxation dynamics, based on measurement at multiple magnetic fields. These efforts have yielded a detailed understanding of their OE-DNP processes, yet at the same time have revealed the complexity of OE-DNP of these nominally simple compounds. Early mechanistic studies of CCl_4 were carried out in the 1970s at low field (0.02–800 mT) by Müller-Warmuth and coworkers. [54] They attributed the OE-DNP behavior to a combination of dipolar relaxation induced by translational diffusion, and scalar relaxation driven by molecular contact, as described by the pulse model. Picosecond timescale molecular motions were identified as a major source of scalar relaxation. CCl_4 and $CHCl_3$ were further characterized by Dorn and coworkers in the 1990s using TEMPO as polarizing agent in a flow OE-DNP setup, where the sample was hyperpolarized at 0.33 T and subsequently transported and detected at 4.7 T. [197] Maximal enhancements up to 2200 $\pm$ 330 were extrapolated at 0.33 T. However, the experimentally observed enhancement was two orders of magnitudes lower, due to polarization loss during sample transport, magnetic field change, and non-optimal s and f. It was only in 2017 that a remarkable 10^3-fold ^{13}C enhancement was experimentally achieved for CCl_4 at 3.4 T by Liu and coworkers using TEMPONE as the polarizing agent. [69] The report established picosecond-timescale dynamics as the key for generating efficient scalar relaxation at these intermediate magnetic fields. More importantly, it provided a proof-of-concept that ^{13}C OE-DNP could be effective even at higher magnetic field: while dipolar relaxation becomes inefficient (see section 2.4), zero-quantum scalar relaxation remains operative. In the same study, enhancements of 550–680 were observed for neat $^{13}CHCl_3$. Later reports by Dubroca [134], Orlando [114], Dai [75], Rao [181], Soundararajan [178], Levien [40], Yang [198] and others reproduced the large enhancements in these model systems at 9.4 T and 14.1 T. Among these, Orlando and coworkers showed $\varepsilon(^{13}C, CCl_4) = 430 \pm 50$ and $\varepsilon(^{13}C, CHCl_3) = 320 \pm 60$ at 9.4 T using a probe equipped with cylindrical MW resonator (Fig. 12) in which both s and f approached their maximal values of 1. [114] Levien, Yang and others reported $\varepsilon(^{13}C, CCl_4) = 120 \pm 10$ and $\varepsilon(^{13}C, CHCl_3) = 200 \pm 20$ at 9.4 T using an NMR-optimized probe without a MW cavity (Fig. 16), which had an estimated saturation factor of 0.3. [40,198] At 14.1 T, all measurements to date have been carried out only with non-resonant probe heads. [114,134] 17- to 70-fold ^{13}C enhancements were again achieved for these model systems when nitroxide polarizing agents were used. Tables 4 and 5 summarize the enhancements and the associating coupling, saturation, and leakage factors for CCl_4 and $CHCl_3$ between 1.2 and 14.1 T with TEMPONE as the polarizing agent. Care should be taken when comparing the two model systems, because the MW B_{1e} is reduced in samples with higher polarity. Consequently, literature reports generally show $\varepsilon(CCl_4) > \varepsilon(CHCl_3)$ when the compounds are measured neat [114], while $\varepsilon(CCl_4) < \varepsilon(CHCl_3)$ is often found when the analytes are diluted in non-polar solvents [40,134].

Starting from the results of these studies, further analyses have shown that the ^{13}C relaxation for CCl_4 and $CHCl_3$ are mediated by the carbon-bonded atoms that are accessible by the polarizing agent – Cl for CCl_4, or Cl and H for $CHCl_3$. [64,69,114] For $CHCl_3$, this phenomenological interpretation implies two distinct sets of correlation times for the scalar spectral density functions:

$$J_{sc}^{CHCl_3}(\omega_e) = \frac{4\pi^2}{h^2}\left(\frac{\langle A_{Cl}^2\rangle}{\tau_{p,Cl}}\left[\tau_{col,Cl}exp\left(-\omega_e\tau_{col,Cl}\right)\right]^2 + \frac{\langle A_H^2\rangle}{\tau_{p,H}}\left[\tau_{col,H}exp\left(-\omega_e\tau_{col,H}\right)\right]^2\right) \quad (34)$$

The process with longer τ_{col} is associated with a hydrogen-bond-like interaction between $CHCl_3$ and TEMPONE, whereas that with shorter τ_{col}

Table 4
^{13}C OE-DNP performances of CCl_4 under various magnetic fields using TEMPONE-^{15}N-d_{16} as polarizing agent.

B_0 (T)	MW setup	c(PA) / mM	ξ	s	f	ε
1.2	Cavity	10	−0.41	0.25	0.925	250 ± 30
3.4	Cavity	30	−0.47	0.75	1	930 ± 100
9.4	Cavity	100	−0.17	1.0	0.98	430 ± 50
14.1	MAS-DNP	10	−0.1*	–	0.9	23 ± 5

Note: this table only includes reports where coupling factors were evaluated experimentally or computationally. Data at 1.2, 9.4 and 14.1 T is from [114]; 3.4 T from [69]; f at 14.1 T is from [134]. *predicted based on spin dynamics model in ref. [114].

Table 5
^{13}C OE-DNP performances of $CHCl_3$ under various magnetic fields using TEMPONE-^{15}N-d_{16} as polarizing agent.

B_0 (T)	MW setup	c(PA) / mM	ξ	s	f	ε
1.2	Cavity	10	−0.46	0.25	0.85	260 ± 40
3.4	Cavity	20	−0.37	0.63	0.9	550 ± 60
9.4	Cavity	100	−0.16	0.8	0.93	320 ± 60
14.1	MAS-DNP	10	−0.07*	–	–	17.5 ± 2

Note: see note of Table 4.

Table 6
Parameters used to fit the variable-field OE-DNP coupling factors of CCl_4 and $CHCl_3$ using TEMPONE as the polarizing agent. $F_i = 4\pi^2\langle A_i^2\rangle/h^2\tau_{p,i}$ (i = Cl or H).

	F_{Cl} [rad^2/s^2]	$\tau_{col,Cl}$ [ps]	F_H [rad^2/s^2]	$\tau_{col,H}$ [ps]	$r_{d,Cl}$ [Å]	$\tau_{d,Cl}$ [ps]	$r_{d,H}$ [Å]	$\tau_{d,H}$ [ps]
CCl_4*	1.69 × 10^{24}	0.5	–	–	4.0	114	–	–
$CHCl_3$†	0.35 × 10^{24}	0.4–0.7	0.03 × 10^{24}	8–20	4.0	53	3.4	39

*from [114]; †from [64];

is attributed to random elastic collisions potentially mediated favorably by Cl. [64] Accordingly, two sets of dipolar relaxation terms were also required to reproduce the field-dependence of the coupling factor for $CHCl_3$ (Table 6), reflecting encounters that occur either through chlorine or through hydrogen. More recent molecular dynamics simulations for $CHCl_3$ revealed a more complex dynamics, where short contact interactions/rapid fluctuations may occur also during hydrogen bond or halogen bond complexation (section 2.5). [64,74] Additionally, because spectral density functions intimately depend on the underlying molecular interactions, the coupling factor of a given analyte varies when different polarizing agents are employed. This effect has been observed experimentally by Levien and coworkers, who reported the variation of ξ of $CHCl_3$, CCl_4, and toluene at 0.34 T and 1.2 T for different nitroxide radicals. [199] Additionally, a computational study by Küçük and coworkers found that $CHCl_3$ exhibited a slower ξ decay with increasing magnetic field when TEMPOL was used instead of TEMPONE. [74].

Another instructive model compound was carbon tetrabromide (CBr_4). First characterized in CCl_4 solution by Orlando and coworkers with TEMPONE using a resonant probe head at 9.4 T, the compound displayed an ^{13}C enhancement of 600 ± 60, approximately 1.4-fold larger than that of CCl_4. [114] This is the largest ^{13}C OE-DNP enhancement reported so far at this magnetic field. Yang and coworkers later corroborated this trend using a non-resonant probe head (with $s \approx 0.3$) at the same field, which showed $\varepsilon(CBr_4) = 180 \pm 18$ and $\varepsilon(CCl_4) = 121 \pm 10$, corresponding to $\varepsilon(CBr_4)/\varepsilon(CCl_4) \approx 1.5$. [198] Available evidence so far indicates that this enhancement trend persists at 14.1 T – using a solid-state MAS-DNP probe head (with $s \approx 0.1$), Orlando and coworkers observed $\varepsilon(CBr_4) = 35 \pm 3$ and $\varepsilon(CCl_4) = 23 \pm 5$. [114] Comparison of the three model systems suggested that ^{13}C enhancement of these halomethanes are promoted by the non-covalent interaction between the polarizing agent and the analyte – specifically, weak hydrogen bond (C–H…O–N) or halogen bond (C–X…O–N; X = Cl or Br) when nitroxide radicals are employed. Additional discussion on the functional group dependence of ^{13}C OE-DNP will be provided in the following section.

5.1.1.2. Carbon-13 in various chemical environments. Recent developments in hardware design and the underlying physical understanding of OE-DNP have extended the scope of ^{13}C OE-DNP application beyond simple model systems to a range of practically relevant molecules, including amino acids, natural products, pharmaceuticals, and molecular probes such as enzyme inhibitors and X-ray contrast agents. [40,75] Measured in a range of solvents of varying polarity – including CCl_4, benzene, $CHCl_3$, water, and DMSO – carbon enhancements up to 20 have been reported using TEMPONE-^{15}N as the polarizing agent. These ^{13}C enhancements are strongly influenced by the local chemical environment. A survey of the ^{13}C enhancements at 9.4 T reveals site specificity, with trends that could guide future design of both polarizing agents and analytes for high-field OE-DNP. Tables A1 to A5 in the appendix summarize the literature-reported ^{13}C enhancements, grouped by instrumentation.

Specifically, higher ^{13}C enhancements were consistently observed when the carbon of interest is adjacent to atoms participating in non-covalent interactions, such as hydrogen or halogen bonds, with nitroxide radicals. These interactions facilitate spin polarization transfer by enabling the generation of ^{13}C isotropic hyperfine coupling. For

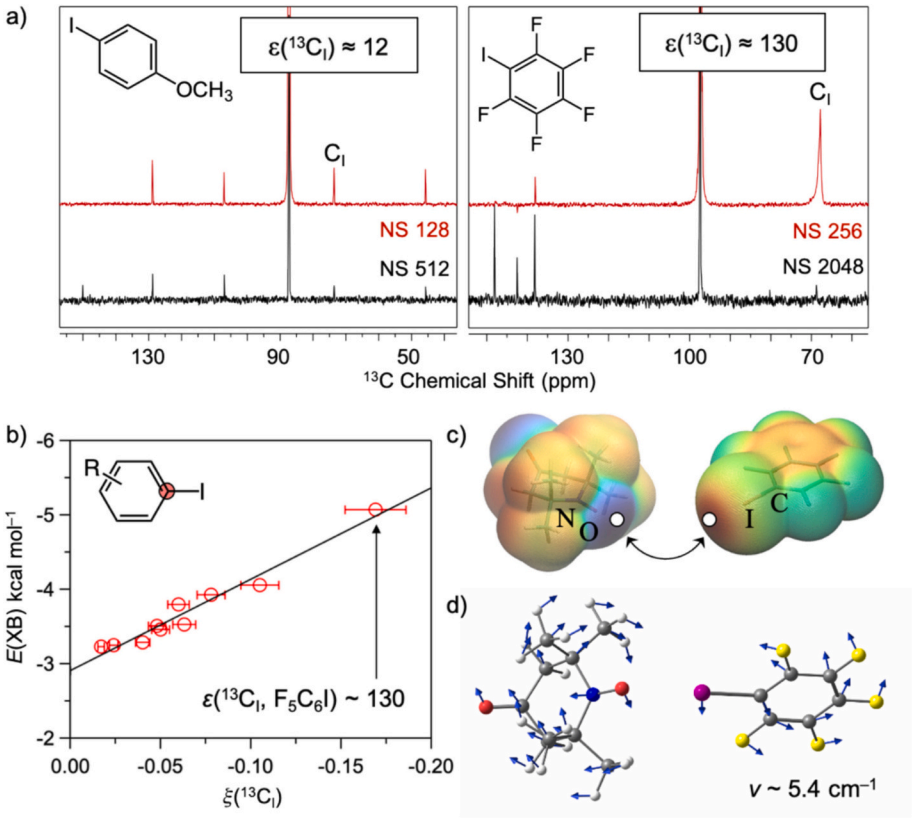

Fig. 18. Role of polarizing agent-analyte halogen bond in facilitating high-field liquid-state ^{13}C OE-DNP enhancement. (a) ^{13}C NMR spectra of CCl_4 solutions of 4-iodo-methoxylbenzene (0.3 M) and pentafluoroiodobenzene (0.6 M) doped with 25 mM TEMPONE-^{15}N-d_{16} under OE-DNP (red) and thermal Boltzmann (black) conditions. (b) Correlation between $^{13}C_I$ coupling factors and DFT-calculated analyte-TEMPONE halogen bond strengths of iodobenzene derivatives. Solid black line is an empirical fit with $r^2 = 0.97$. (c) Electrostatic potential of TEMPONE and C_6F_5I. The blue electronegative region of TEMPONE interacts preferentially with the red electropositive region of C_6F_5I. White dots represent electrostatic potential maximum (i.e. C—I σ-hole, see text) or minimum. (d) Example of low-energy vibrational mode of the TEMPONE-C_6F_5I transient complex. Adapted from ref. [198]. (For interpretation of the references to colour in this figure legend, the reader is referred to the web version of this article.)

protonated carbons, illustrative examples include small aromatic molecules, where protonated aromatic carbons ($\varepsilon \approx 3$–20 using the setup in Fig. 16) exhibit higher enhancements than non-protonated aromatic carbons functionalized bearing nitro, alkyl, methoxy, nitrile, carbonyl, and fluorine substituents ($|\varepsilon| < 1$) under comparable conditions. Additional examples include protonated carbons α- to electron-withdrawing groups, such as the methyl and methylene groups α- to carbonyl moieties, as well as the methylene carbon in diethyl malonate; these typically yield larger enhancements than non-functionalized alkyl carbons (e.g., in cyclopentane, cyclohexane, hexane, and heptane). A similar trend is observed for electron-withdrawing groups bearing protonated carbons. For instance, the aldehyde carbon of phenylacetaldehyde, and the terminal alkyne carbon of phenylacetylene ($\varepsilon \approx 10$–20) display markedly higher enhancements than their non-protonated analogs, such as the ketone or internal alkyne carbons (Tables A1-A3). Overall, these observations can be summarized as follows: protonated carbons exhibit superior ^{13}C enhancements than non-protonated ones, and carbons bearing more acidic (i.e. smaller pK_a) protons tend to show larger enhancements. This is consistent with observations made at lower magnetic fields. [55] While measurements at 14.1 T have so far been limited to a small number of analytes, including CCl_4, $CHCl_3$, CBr_4, hexane, and phenylacetylene [114,134], evidence so far indicates that a similar dependence on chemical functionality persists at higher fields.

5.1.1.3. Role of non-covalent bonds to nitroxide polarizing agents. The observations above indicate that non-covalent interactions with nitroxide radicals facilitate the generation of ^{13}C-isotropic hyperfine coupling at adjacent ^{13}C nuclei, thereby promoting scalar-driven cross-relaxation, which is a critical mechanism for preserving OE-DNP efficiency at high magnetic fields. Although weaker than O—H, N—H, or F—H variants, hydrogen bonds involving C—H have been well documented. [200] The impact of hydrogen bonding becomes more pronounced for acidic protons, which are known to favor stronger hydrogen bonding interactions. The possible involvement of C–H…N–O hydrogen bonds in OE-DNP has already been examined at lower magnetic fields by Müller-Warmuth, Bates, Dorn and others. [4,54,55,185,197,201] While many studies aimed to correlate ^{13}C DNP enhancements with the induced isotropic hyperfine constants arising from C–H…O–N interactions, the related molecular dynamics also contribute in important ways. For example, Orlando and coworkers recently showed that the C–H…O–N interaction in the $CHCl_3$…TEMPONE transient complex generates spectral density at both tens-of-picosecond timescales – through stabilizing the transient complex – and also at sub-picosecond timescales. [64] Despite these insights, the influence of non-covalent interactions on molecular dynamics relevant for high-field liquid-state OE-DNP still remains only partially understood and requires more systematic analysis.

Another important class of non-covalent interaction facilitating ^{13}C OE-DNP is the halogen bond, initially proposed for CCl_4, $CHCl_3$, and CBr_4. The recent report by Levien and coworkers [40] identified increased enhancements for polychlorinated and mono-iodinated carbons, including those in iodobenzene, adenyl cyclase inhibitor ST034307, mitotane, amiodarone hydrochloride, and sodium diatrizoate. Halogen bonds can be described as an attractive interaction between the electronegative oxygen of the nitroxide radical and the electropositive "σ-hole", which refers to a region along the extension of a C–X bond (X = Cl, Br, I). [202] The role of polarizing agent-analyte halogen bond in high field liquid-state OE-DNP has been investigated in depth by Yang and coworkers. [198] In this study, the authors systematically modulated the halogen bond strength between TEMPONE and a series of iodobenzene derivatives by introducing electron-withdrawing substituents onto the aromatic system. Up to 10-fold boost of the ^{13}C DNP enhancements was observed for iodinated and brominated aromatic carbons upon functionalization with stronger electron-withdrawing groups (Fig. 18a). Notably, a 130-fold enhancement was obtained for the $^{13}C_I$ site of pentafluoroiodobenzene, surpassing that of CCl_4 ($\varepsilon \approx 120$) measured on the same spectrometer (i.e., under comparable saturation conditions). This represents the first example of a non-halomethane molecule exhibiting a ^{13}C enhancement exceeding two orders of magnitude at 9.4 T in the liquid state.

Computational studies illustrated that polarizing agent-analyte transient complexes stabilized by the C–I…O–N halogen bond induce isotropic hyperfine interactions at least an order-of-magnitude stronger than those arising from alternative non-covalent interactions. Further investigation by Yang and coworkers revealed linear correlations between the polarizing agent-analyte C–I…O–N halogen bond strength (Fig. 18b), $^{13}C_I$ spin population, ^{13}C isotropic hyperfine constants, and the experimental $^{13}C_I$ coupling factors for a series of iodobenzene derivatives in different solvents. Recognizing that the accuracy of DFT hyperfine calculations is system- and functional-dependent [203,204], the authors further validated these correlations using multiple DFT methods as well as the DLPNO-CCSD (domain-based local pair natural orbital coupled-cluster with singles and doubles) method, which yields high-accuracy EPR parameters at the expense of increased computation cost. [205,206] Altogether, these results provide compelling evidence that polarizing agent-analyte halogen bonding is a key in boosting the ^{13}C enhancements of the halogenated carbons. In addition to electronic effects, the report identified potential influences of halogen bonds on the polarizing agent-analyte molecular dynamics. These include modification of the analyte electrostatic potential surface (Fig. 18c), as well as the presence of low-energy halogen-bond-related vibrations of the polarizing agent-analyte transient complex (Fig. 18d), occurring on the optimal timescale for high-field OE-DNP (~0.6 ps at 9.4 T, corresponding to ~8.8 cm^{-1}). These dynamic aspects manifest in a more complex halogen-bond dependency of the DNP performances of several chlorinated and brominated compounds. [198].

5.1.2. Hydrogen-1

^1H NMR is perhaps the most widespread NMR method across both academic and industrial settings due to the near-universal presence of protons (> 99.9% natural abundance) and their high NMR sensitivity. Nevertheless, ^1H NMR hyperpolarization remains desirable when conventional NMR sensitivity becomes insufficient for chemical analysis, for instance, for low concentration samples in biological [1,36,207] and environmental sciences [208,209], for in situ chemical reaction monitoring [210,211], or when ^1H serves as a polarization reservoir for

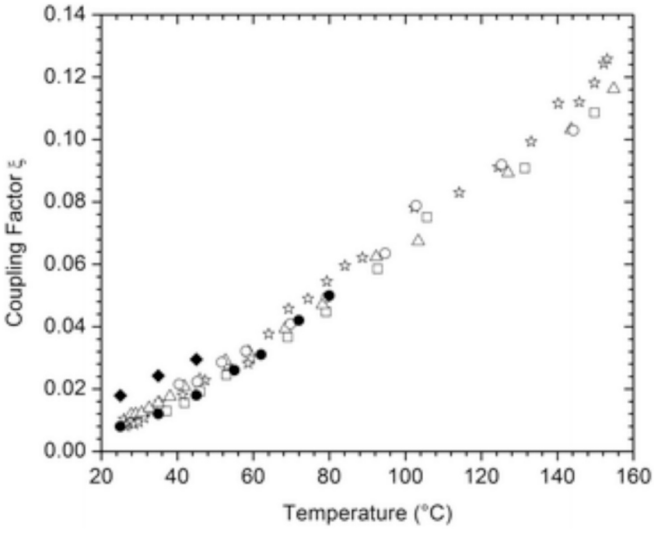

Fig. 19. Coupling factor between the TEMPOL radicals and water protons as a function of sample temperature. The coupling factors assessed from DNP experiments (□,○,△,☆) are compared to coupling factors determined through NMRD measurements (●) and by molecular dynamics (◆). Reproduced with permission from ref. [152].

enhancing other nuclei [194]. In the context of OE-DNP, ^{1}H has undergone extensive study – in fact, it was the first nucleus explored at magnetic field ≥3 Tesla, as demonstrated by Bennati, Prisner and coworkers. [44,115] Unlike ^{13}C, which could experience both scalar and dipolar OE-DNP relaxation, ^{1}H OE-DNP has been almost exclusively reported as dipolar-dominant when using nitroxide or galvinoxyl polarizing agents, except for rare cases involving reversible protonation of the polarizing agent [212] or protons anchored on conductive materials [213] at low fields. As such, the theoretical maximum ^{1}H OE-DNP enhancement is approximately −328 (Table 3), corresponding to $\xi_{max} = 0.5$.

Dipolar relaxation may arise from translational or rotational diffusion. Because the correlation times of these processes are diffusion-controlled and typically lie in the 1 to 100 ps range, dipolar-driven OE-DNP is more efficient at lower magnetic fields. Indeed, early studies in the 1970s conducted below 1.5 T sometimes could achieve substantial enhancements approaching the theoretical limit. [3,4,214,215] However, most ^{1}H NMR-based structural elucidation requires high chemical shift resolution, thus necessitating high magnetic field operation (usually >9 T). To circumvent this mismatch between the optimal OE-DNP condition and the desired magnetic field for high-resolution analysis, Dorn and coworkers developed a two-field flow system where the sample was hyperpolarized at 0.33 T using an X-band EPR resonator and then flowed to a liquid-state NMR spectrometer at 4.7 T for detection. [42,55,216] Lingwood, Krummenacker, Denysenkov, and others have adapted the flow-based OE-DNP methodology to enhance MRI contrast of phantoms at 1–2 T. [217–220] More recent examples by Münnemann and coworkers integrated flow OE-DNP with benchtop NMR spectroscopy (~ 1.0 T) to compensate for the reduced sensitivity compared to high-field instruments. [221–224] A similar principle was explored by Bennati, Griesinger, and coworkers in the form of a shuttle system between a 0.34 T commercial EPR spectrometer (or later, the stray field of a superconducting magnet with specialized shimming) and a 14.1 T liquid-state NMR spectrometer. [225–227] Despite efficient low-field ^{1}H OE-DNP hyperpolarization, the two-field approach faces intrinsic drawbacks, including relaxation loss during sample transfer (as accelerated by the polarizing agent and magnetic field change), and increased thermal polarization when reaching the high-field detector. Further OE-DNP experiments carried out at intermediate magnetic fields, 3.4 T, revealed one or two orders-of-magnitude enhancements for ^{1}H in water [44,228] and toluene [229] doped with nitroxides at elevated sample temperatures when solvents reach boiling or supercritical states. [230].

The first high-field (9.2 Tesla) liquid-state ^{1}H OE-DNP experiment was performed by Prisner, Prandolini, Denysenkov, and coworkers using the cylindrical resonator described in Fig. 12 on TEMPOL doped water. [45,115] Initial measurements employing a 45 mW continuous-wave solid-state MW source yielded a ^{1}H enhancement of −4 for water. [45,115] Under similar conditions, Krummenacker and coworkers observed only modest enhancements of $\varepsilon(^{1}H) \approx -1$, corresponding to a signal inversion, for cancer-related metabolites of pyruvate, lactate, and alanine. [219] Subsequent adoption of high-power gyrotron MW irradiation enabled $\varepsilon(^{1}H) \approx -10$ for water at ~318 K [46,152], and $\varepsilon(^{1}H) \approx -83$ (Fig. 19) when the sample was heated to ~433 K [152]. Alternatively, an enhancement of $\varepsilon(^{1}H) \approx -10$ for water could be achieved by the use of narrow-line polarizing agents, such as Fremy's salt, under low (45 mW) MW power. [116] Similar degrees of enhancement were later achieved also by Yoon and coworkers using TEMPOL and a non-resonant probe head (Fig. 14) capable of delivering maximum $B_{1e} \approx 2.5$ G at the sample position. [138] Comparison between coupling factors determined from ^{1}H OE-DNP enhancements of TEMPOL in various organic solvents at 9.2 T and NMRD revealed substantial contributions to the coupling factor by fast sub-picosecond dynamics of the polarizing agent-analyte (i.e. solvent) complex, especially in more viscous solvents such as DMSO. [61,231,232] Recent work by Kuzhelev and coworkers [63] revealed correlation between the rotational correlation times of a series of polarizing agents dissolved in DMSO and the ^{1}H enhancements of DMSO, with longer $\tau_{d,rot}$ producing smaller $|\varepsilon(^{1}H)|$ through their influences on the inner-sphere rotational diffusion of the polarizing agent-analyte transient complex. This observation aligns well with an earlier study by Levien and coworkers, which associated $\varepsilon(^{1}H)$ changes with the molecular mass of the polarizing agents. [62] The above studies are further consistent with earlier results by Neugebauer and coworkers, who reported an increase in the proton coupling factor for a water-TEMPOL system from 0.008 to 0.14 upon heating from 25 °C to 155 °C (Fig. 19). [152] Such an increase was attributed to faster translational diffusion and, more critically, faster inner-sphere reorientation occurring at the picoseconds timescale at elevated temperatures. Collectively, these reports provided mechanistic insight into high-field liquid-state ^{1}H OE-DNP, while highlighting temperature as an important operational parameter.

Additionally, studies have shown that NMR spectral features are altered by the use of supercritical fluid (SF) as the solvent, which is generated under high pressure, and endows much shorter molecular correlation times for the dissolved substances. [233] This principle has been investigated in the context of ^{1}H OE-DNP of small organic molecules at 1.4–3.4 T in SF ethylene and SF CO_2, generated by maintaining the sample compartment under 60–300 bar pressure. [55,230,234] Particularly, Dorn and coworkers reported ~2.5-fold increase in $\varepsilon(^{1}H)$ of benzene at 0.33 T by changing the solvent from C_6D_6 to SF CO_2. [55] van Bentum and coworkers predicted a diffusion correlation time ≤ 1 ps and $\varepsilon(^{1}H) < -100$ for toluene at 14.1 T. [230] Nevertheless, high-field OE-DNP performed with SF solvents have not yet been demonstrated experimentally.

5.1.3. *Fluorine-19*

Fluorine-19 is the second most sensitive stable nucleus in the NMR periodic table. It has 100% natural abundance and a gyromagnetic ratio approximately 94% that of ^{1}H. Combined with a broader chemical shift dispersion than ^{1}H, ^{19}F plays an important role in NMR-based chemical analysis. While chemically less ubiquitous than ^{1}H or ^{13}C, fluorine comprises a key structural element in many pharmaceuticals [235,236], agrochemicals [237,238], and solution-processable polymers [239,240]. Moreover, ^{19}F NMR has become an invaluable tool for studying biological systems, because it can serve as a sensitive spin label for distance and orientation measurements while contributing minimal background signal. [241–244] Hyperpolarization of ^{19}F is particularly beneficial for applications demanding exceedingly low limits of detection, such as biolabel detection, environmental analysis, and MRI contrast agent development. [209,245] To this end, photo-CIDNP, dissolution DNP, and parahydrogen-based methods have been investigated as possible viable options. Recently, Gomez and coworkers demonstrated 1D and 2D ^{19}F NMR enhanced by photo-CIDNP. [246] Bernarding and coworkers further showed a detection limit that was below nanomole quantities of an antiviral drug favipiravir using 1D ^{19}F photo-CIDNP-MRI. [247] Silva Terra and coworkers reported up to 5700-fold ^{19}F signal enhancement of a 1D acquisition via SABRE combined with multiplet refocusing. [248] Hilty and coworkers utilized ^{19}F dissolution DNP in reaching ^{19}F enhancements of several thousands to measure the binding affinity of ligands. [249,250] Nevertheless, as with other nuclei, these hyperpolarization approaches are generally single-shot in nature, thereby making OE-DNP an attractive route for obtaining regenerable hyperpolarization.

Extensive investigation of ^{19}F OE-DNP has been performed over the last few decades. George [118], Neudert [251], Peksoz [252], Webb [253], Poindexter [215,254], Müller-Warmuth [67], Dey [255], Loening [43], and others have carried out in-depth mechanistic studies of compounds with a range of fluorine functionalities using both resonant and non-resonant probe head configurations. Depending on the analyte and polarizing agents (including nitroxides, galvinoxyl, BDPA, 2,3,5,6-tetrachlorosemiquinone, and 2,4,6-triphenyl pyrylyl), both scalar- and dipolar-dominated cross-relaxation were observed. Chandrakumar and

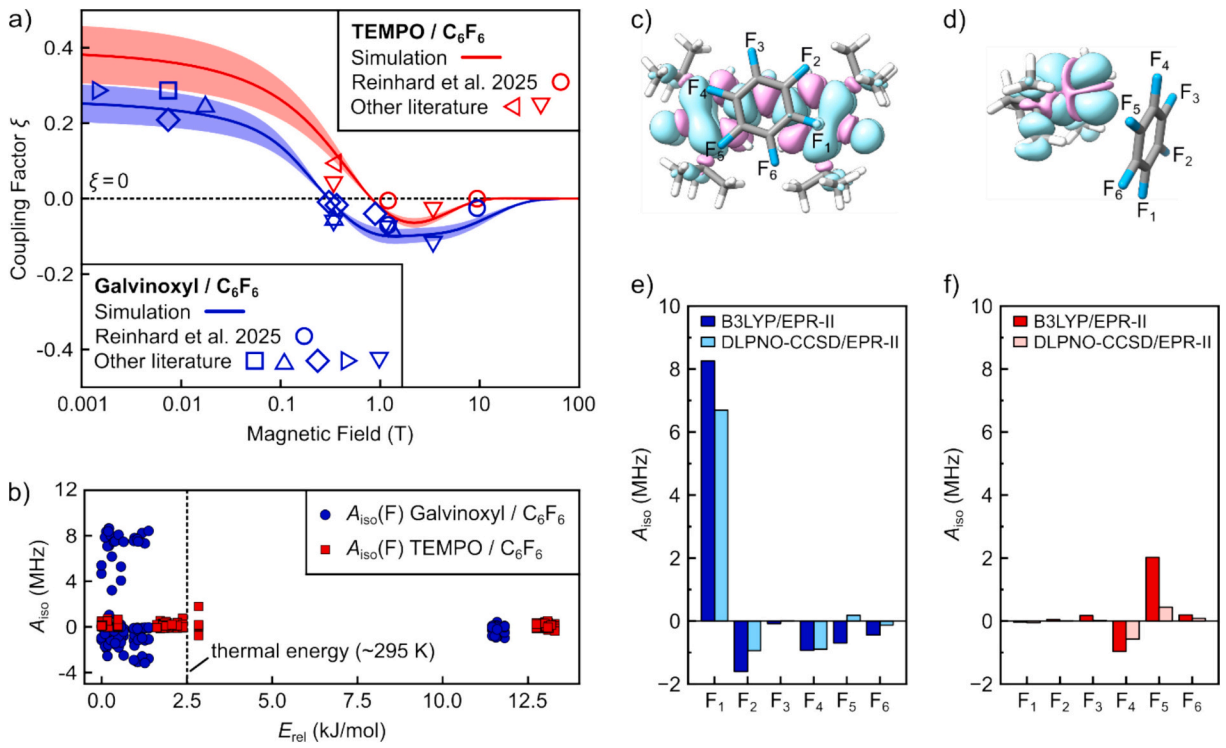

Fig. 20. (a) Magnetic field dependence of the ^{19}F coupling factor of C_6F_6 when hyperpolarized with TEMPO (red) or galvinoxyl (blue). Solid lines are simulations. Shading represents ±20% uncertainty. (b) Isotropic hyperfine coupling constants of optimized polarizing agent-analyte complexes (blue for galvinoxyl-C_6F_6, red for TEMPO-C_6F_6) plotted against the relative single-point energies of the complexes. (a) and (b) were adapted from ref. [39]. (c-d) DFT-optimized structures of (c) galvinoxyl-C_6F_6 and (d) TEMPO-C_6F_6 complexes with their calculated spin density distribution (both isosurface thresholds are ±0.0005 e/Å^3). (e-f) Comparison of the calculated isotropic hyperfine couplings to ^{19}F of the respective complexes shown in (c-d) using DFT (B3LYP/EPR-II) and coupled-cluster level of theory (DLPNO-CCSD/EPR-II). (For interpretation of the references to colour in this figure legend, the reader is referred to the web version of this article.)

Table 7
Parameters describing the variable-field OE-DNP performances of hexafluorobenzene using galvinoxyl and TEMPO as the polarizing agent. Collision of type i is described by duration $\tau_{col,i}$ and $F_i = 4\pi^2\langle A_i^2\rangle/h^2\tau_{p,i}$. Indices $i = 1, 2$ are used here because their molecular origins are unknown. Data is taken from ref. [39].

Polarizing Agent	Molecular collision				Translational diffusion		Rotational diffusion	
	F_1 [rad^2/s^2]	$\tau_{col,1}$ [ps]	F_2 [rad^2/s^2]	$\tau_{col,2}$ [ps]	r_d [Å]	τ_{trans} [ps]	k_{rot} [s^{-2}]	τ_{rot} [ps]
Galvinoxyl	16.8×10^{24}	0.3	0.25×10^{24}	4.1	2.75	50	1×10^{10}	40
TEMPO	1.69×10^{24}	1.0	–	–	2.8	50	–	–

coworkers later extended these studies to intermediate magnetic fields of 0.34–3.4 T. [118] Up to 20-fold ^{19}F enhancements were observed when the OE-DNP experiments were performed with galvinoxyl rather than nitroxide radicals. Leveraging these 1D enhancements, the authors reported the first OE-DNP enhanced 2D NMR of ^{19}F—^{19}F COSY and ^{19}F—^{13}C HETCOR experiments.

Only recently has liquid-state ^{19}F OE-DNP been demonstrated at 9.4 Tesla, by Levien, Reinhard, and others using the NMR-optimized $^{13}C/^{1}H$ two-channel DNP setup (Fig. 16), where ^{19}F was detected through the ^{1}H circuit. [39,40] Consistent with the earlier studies by Chandrakumar and coworkers at lower magnetic fields, galvinoxyl proved to be a superior polarizing agent for ^{19}F OE-DNP compared to nitroxides. [118] Scalar-dominant OE-DNP with $\varepsilon(^{19}F) = 5$–20 was routinely achieved across a variety of small molecules containing various fluorine functionalities and chemical environments, whereas nitroxides yielded more modest enhancements of $0 < \varepsilon(^{19}F) \leq 4$. Analysis of the field dependence of the ^{19}F coupling factors of the hexafluorobenzene model system across 0.0015, 0.0074, 0.34, 1.2, 3.4, and 9.4 T revealed that the ^{19}F OE-DNP was governed by processes involving spectral densities arising from translational diffusion, rotational diffusion, and molecular collision (Fig. 20a, Table 7). [39] Compared to the OE-DNP process induced by TEMPO, an additional fast (sub-picosecond) collision term, and the rotational diffusion component were required to describe that of galvinoxyl. Importantly, the amplitude of the term F of the major collision-induced spectral density contribution of galvinoxyl is an order of magnitude larger than that of TEMPO. Further DFT computation revealed that galvinoxyl induces stronger ^{19}F isotropic hyperfine couplings in the thermodynamically more stable structures of its transient complexes with hexafluorobenzene (Fig. 20b). Comparison of the electronic effects of representative TEMPO- and galvinoxyl-hexafluorobenzene complexes evaluated by DFT and DLPNO-CCSD showed good agreement between the two methods (Fig. 20c-f). Finally, extrapolation of the magnetic-field-dependent coupling factor [39] suggested that sizable ^{19}F OE-DNP enhancements may be attainable at magnetic fields higher than 9 T.

5.1.4. *Phosphorous- 31*

Phosphorous is another important element studied by NMR. Found in diverse chemical environments, phosphorous is commonly employed in supporting ligands for organometallic catalysts, as well as active sites for organocatalysis. [256,257] In biological systems, phosphorous contributes in energy metabolism, cellular biochemistry, and genetic

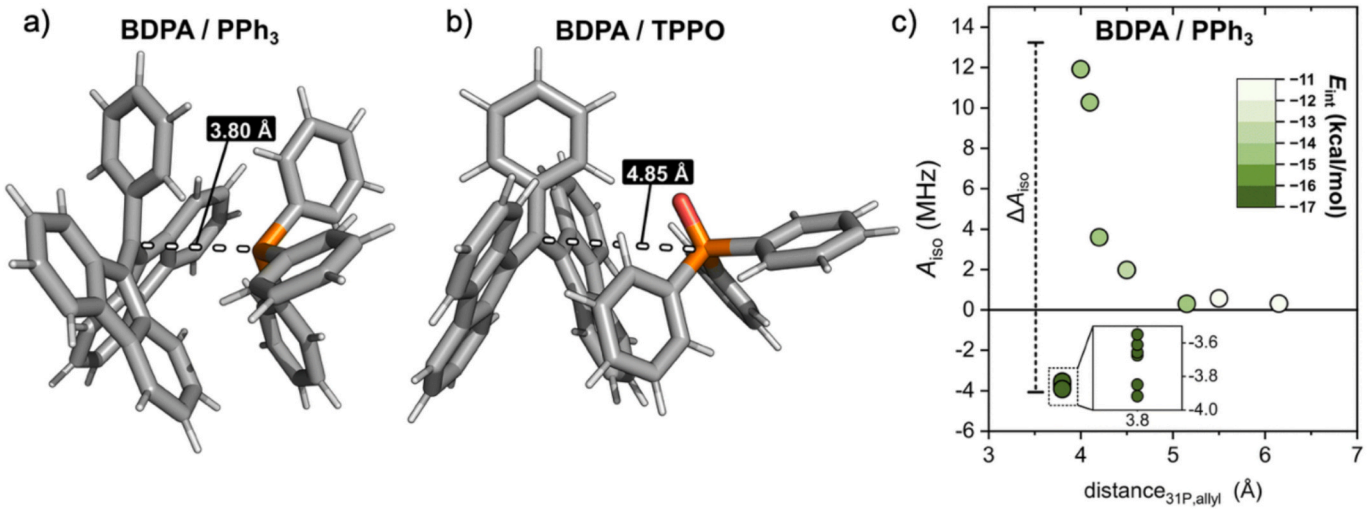

Fig. 21. DFT-optimized structures of transient complexes of BDPA and (a) $P^{III}Ph_3$ and (b) $P^{V}OPh_3$. Distances between P and the central allyl carbon are marked with their values. (c) Calculated ^{31}P isotropic hyperfine constants and single-point energies of DFT-optimized BDPA-$P^{III}Ph_3$ complexes plotted against the ^{31}P-allyl group distance. Adapted from ref. [131].

coding. [258–260] As the only stable isotope of phosphorous, ^{31}P is a spin-1/2 nucleus with a gyromagnetic ratio and sensitivity lying between those of ^{1}H and ^{13}C. In terms of ^{31}P OE-DNP, both scalar- and dipolar-dominant cross-relaxation mechanisms have been observed, with triphenylphosphine (PPh_3) routinely reaching $\varepsilon \sim 10^2$ under a wide range of magnetic fields (0.0074–14.1 T). [43,131,134,138,182] ^{31}P OE-DNP has a theoretical maximum signal enhancement of 1624 when dominated by scalar relaxation.

Early studies on ^{31}P OE-DNP date back to the 1970s, when compounds with diverse phosphorous chemical environments were systematically examined at low magnetic fields (< 0.1 T). [261–267] Scalar-dominated ^{31}P enhancements were observed for protonated and halogenated phosphorous centers, as well as those possessing electron lone pairs, when paired with polarizing agents such as galvinoxyl, BDPA, TTBP (2,4,6-tri-tert-butylphenoxyl) and various nitroxide radicals. [263,266] In contrast, ^{31}P shielded by oxo- or aliphatic substituents typically exhibits dipolar-dominated OE-DNP behavior. [264] For example, $P^{III}Ph_3$ (Ph = phenyl group), $P^{V}OCl_3$, and $(MeO)_2(H)P^{V}O$ yielded positive ^{31}P enhancements at 0.0074 T using TTBP, whereas $P^{V}OPh_3$ showed negative DNP enhancements. Such mechanistic distinctions persist at higher magnetic fields.

Recently, Reinhard and coworkers reported enhancements up to 360 for PPh_3 with BDPA at 1.2 T, but no enhancement for $POPh_3$. [131] DFT analysis of the polarizing agent-analyte transient complexes revealed preferential BDPA-$P^{III}Ph_3$ complexation mediated by the phosphorous lone pair, which facilitates a strong isotropic hyperfine interaction and efficient scalar relaxation for ^{31}P (Fig. 21). Such interaction is absent in $POPh_3$ due to involvement of the lone pair in the P═O bond. Owing to the large enhancements achievable with this system, PPh_3-BDPA has become a standard benchmark for OE-DNP instrument performance from 5 T to 14.1 T, routinely producing 100- to 200-fold enhancements. [43,137,138,182] Beyond triphenyl phosphine, detailed mechanistic studies of ^{31}P OE-DNP relevant for high-resolution NMR (≥ 9 T) remain scarce. In contrast to OE-DNP, SE-DNP has been shown to generate enhancements up to $|\varepsilon| \approx 45$ for pentavalent phosphorous species in aqueous solution. [107].

5.2. *Applications of high-field liquid-state OE-DNP*

The main goal of hyperpolarized NMR is its seamless integration into conventional NMR applications, which spans chemical analytics, structural elucidation of small molecules, investigation of biological systems, and studies of catalytic processes. While dDNP has been well-established for metabolic studies and biological imaging, OE-DNP remains in an early stage of development in this regard. The recent advent of high-field OE-DNP over the past decade – with improvements in enhancements

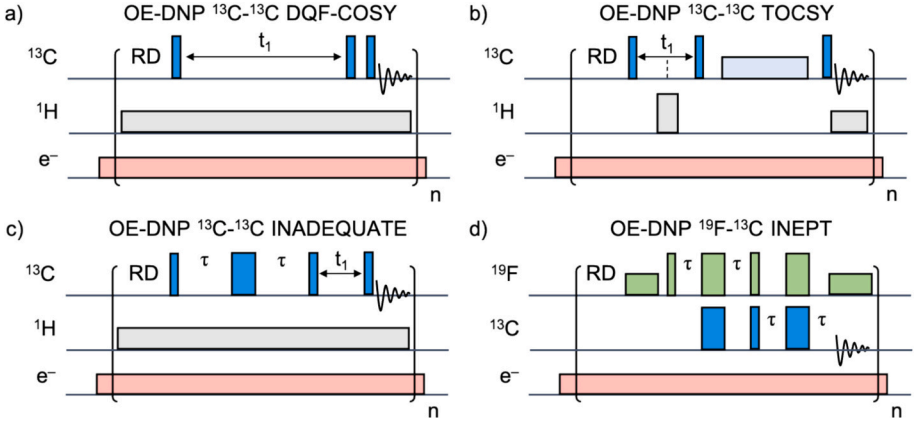

Fig. 22. Pulse sequences reported for OE-DNP enhanced 2D correlation and polarization transfer experiments. [39,40,271] It is worth noting that, apart from the introduction of CW MW irradiation, the pulse sequences for OE-DNP enhanced NMR are analogous to the standard NMR pulse sequences; this favors the implementation of OE-DNP in NMR spectroscopy.

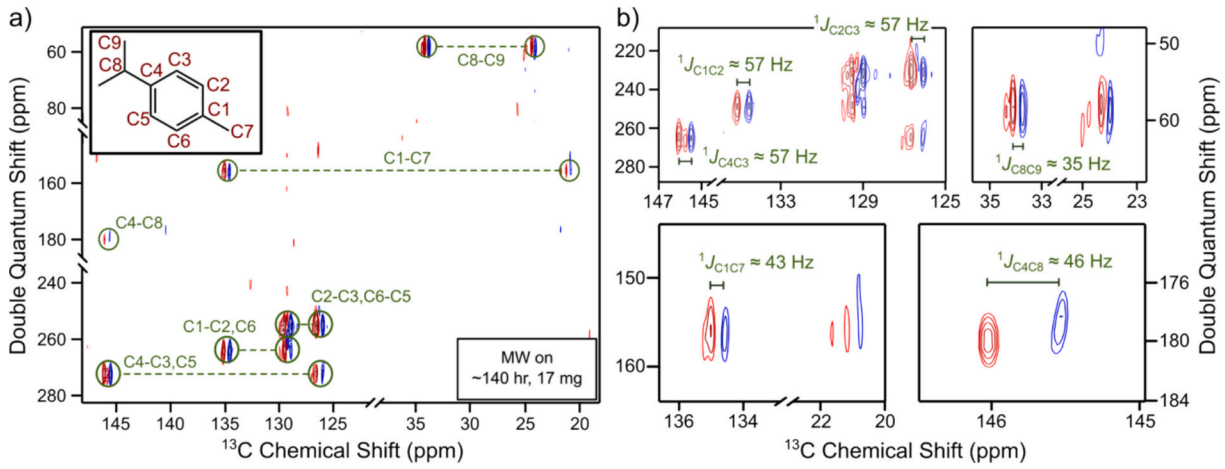

Fig. 23. OE-DNP enhanced 2D $^{13}C—^{13}C$ INADEQUATE (a) of neat *p*-cymene (liquid) doped with 100 mM TEMPONE-^{15}N-d_{16} measured at 9.4 T using the NMR-optimized setup described in Fig. 16. Inset in panel (a) shows structure of *p*-cymene. Expanded views in panel (b) illustrate one-bond $^{13}C—^{13}C$ *J*-coupling constants that can be measured in (a). Adapted from ref. [40].

and spectral resolution for multiple nuclei – has motivated the first applications to more practically relevant systems. In the following section, we summarize developments in this direction.

5.2.1. *OE-DNP for structural elucidation of small molecules*

5.2.1.1. OE-DNP enhanced 2D NMR. While 1D NMR reflects the diversity of chemical environments in a chemical system, assigning resonances often requires implementation of 2D or higher-dimensional correlation experiments. In a multidimensional NMR experiment, information on correlation is encoded into the cross-peaks after Fourier transform of a series of 1D spectra acquired with incremented interpulse delays. Because these experiments require repeated acquisitions and often involve low natural-abundant nuclei, they are time-consuming and often require costly isotopic enrichment. To this end, hyperpolarization techniques can significantly speed up multidimensional NMR acquisition. However, the iterative nature of multidimensional experiments poses challenges for many single-shot hyperpolarization methods. Advanced acquisition and processing methods compatible with single-shot hyperpolarized NMR have been developed, for instance, by taking advantage of fast nuclear spin-lattice relaxation [36,268], combining spatial-encoding with polychromatic excitation [37,269,270], or supplying fresh reaction mixture [38,246]. However, these approaches tend to be system specific, have higher experimental complexity, require adaptation of existing pulse sequences, or involve non-recoverable sample consumption. In contrast, OE-DNP allows continuous in situ generation of hyperpolarization, thus enabling repeated multidimensional acquisition on the same sample. This makes OE-DNP an attractive approach for hyperpolarized multidimensional liquid-state NMR.

To date, 2D OE-DNP NMR has been explored far less extensively than its 1D counterpart. Early demonstrations by Chandrakumar and

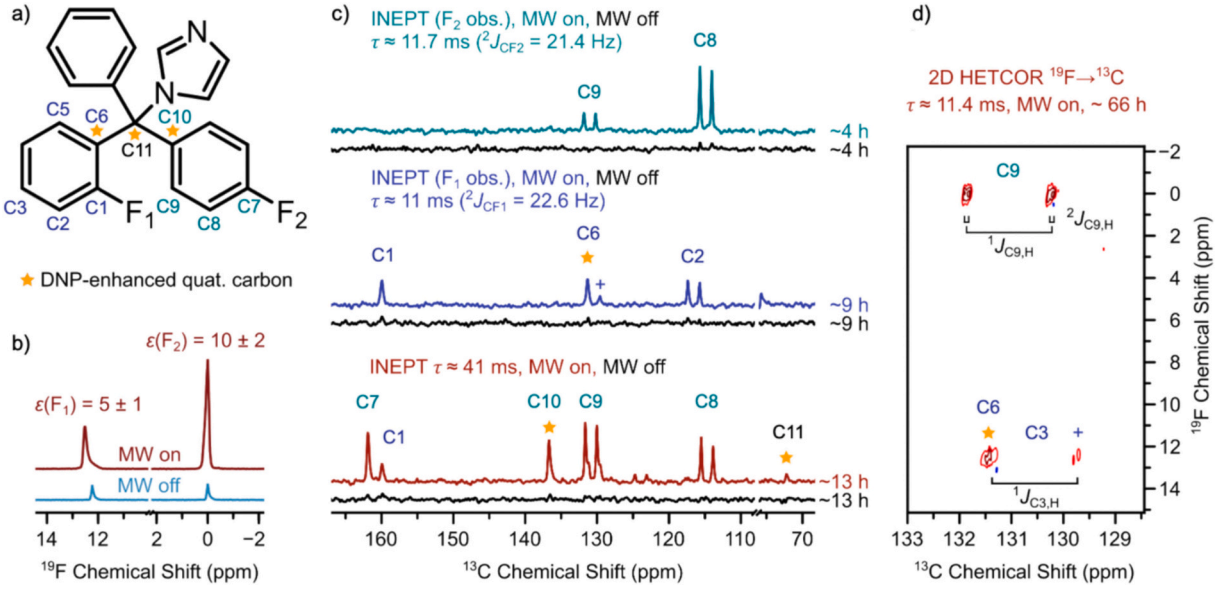

Fig. 24. OE-DNP enhanced $^{19}F—^{13}C$ 1D INEPT and 2D HETCOR of flutrimazole (~ 0.1 M solution in 9:1 *v*/v CCl_4:$CHCl_3$ doped with ~15 mM galvinoxyl). (a) Structure of flutrimazole. Stars denote quaternary carbons. (b) OE-DNP enhanced ^{19}F pulse-acquire spectra. (c) OE-DNP enhanced $^{19}F—^{13}C$ INEPT spectra with selective ^{19}F pre-saturation. Red, blue (F_2 pre-saturated and F_1 observed), and green (F_1 pre-saturated and F_2 observed) traces are enhanced spectra optimized for transfer between different $^{19}F—^{13}C$ pairs. Black traces were collected under thermal Boltzmann conditions. (d) OE-DNP enhanced $^{19}F—^{13}C$ HETCOR spectrum. For (b, c, d), GARP-4 broadband ^{19}F decoupling was implemented during ^{13}C acquisition. Symbol (+) marks one of the C3 doublets. Adapted from ref. [39]. (For interpretation of the references to colour in this figure legend, the reader is referred to the web version of this article.)

coworkers at 0.34, 1.2, and 3.4 T employed ^{19}F—^{19}F COSY (correlation spectroscopy) and ^{13}C—^{1}H HETCOR (heteronuclear correlation spectroscopy) experiments, in which a short DNP excitation (about a second of MW irradiation) was delivered immediately prior to each increment of the NMR pulse sequence. [118,272] Keller and Maly later demonstrated OE-DNP-enhanced ^{1}H 2D *J*-resolved spectroscopy at 0.35 T. [273] These measurements utilized EPR resonators equipped with RF coils.

The first examples of OE-DNP enhanced 2D NMR at 9.4 Tesla – specifically ^{13}C—^{13}C correlation experiments – have been recently reported by Levien and coworkers using the OE-DNP instrument described in section 4 (Fig. 16). [40,184] These works included DQF-COSY (double-quantum-filtered correlation spectroscopy; Fig. 22a) and TOCSY (total correlation spectroscopy; Fig. 22b) acquired on ^{13}C-enriched samples, and INADEQUATE (incredible natural-abundance double quantum transfer experiment; Fig. 22c) acquired on samples at natural ^{13}C abundance. All experiments were performed with standard NMR sequences [274–276] operated under continuous MW irradiation. The resulting OE-DNP enhanced 2D spectra recapitulate the structural information obtainable from conventional NMR, while exhibiting enhanced cross- and diagonal-peaks, whose intensities are modulated by the corresponding 1D enhancement factors. Notably, OE-DNP-^{13}C-INADEQUATE enabled full mapping of the ^{13}C connectivity of the natural product *p*-cymene using 17 mg of sample, while resolving the $^{1}J_{CC}$ coupling constants in the 30–60 Hz range (Fig. 23). A more recent report by Reinhard and coworkers further demonstrated OE-DNP enhanced ^{19}F—^{13}C heteronuclear coherence transfer experiments, as detailed in the next section. [39].

5.2.1.2. Transfer of OE-DNP hyperpolarization between nuclei. OE-DNP enhanced 2D NMR redistributes hyperpolarization across coupled nuclear spin networks through polarization and coherence transfer. For instance, in the enhanced ^{13}C-TOCSY experiment, cross and diagonal peaks sharing the same indirect dimension frequency (i.e. appearing in the same row of a 2D spectrum) possess the same enhancement factors ε. [40] For OE-DNP-^{13}C-INADEQUATE, ε of each cross peak corresponds to the arithmetic mean of the 1D ε of the two coupled carbons. [40] Naturally, such hyperpolarization transfer schemes can also be extended to 1D experiments, allowing enhancement of nuclei that otherwise possess unfavorable ε under direct OE-DNP conditions.

Among the various polarization transfer schemes applied in liquid-state NMR, the coherence transfer methods of INEPT (insensitive nuclei enhanced by polarization transfer) [277] and isotropic mixing (i.e. homonuclear Hartmann-Hahn polarization transfer; the key element of TOCSY) [278,279] have been explored in the context of high-field liquid-state OE-DNP. Dai and coworkers provided an early demonstration of DNP-enhanced non-refocused INEPT at 9.4 T in the liquid state, which was used to transfer polarization onto ^{13}C from scalar-coupled ^{1}H hyperpolarized by SE-DNP in a viscous medium. [105] Compared to the MW-off 1D ^{13}C experiment, the SE-DNP enhanced ^{1}H—^{13}C INEPT experiment exhibited an overall enhancement approximately equal to the product of the 1D ^{1}H DNP enhancement $\epsilon(^{1}H)$ and the conventional thermal INEPT transfer factor, determined by γ_{1H}/γ_{13C} and the number of coupled protons. The amplification factor given by the multiplicative contribution of hyperpolarization and thermal polarization ratios opens up a promising avenue for speeding up structural elucidation by heteronuclear correlation. The same principle was further illustrated in the recent report by Reinhard and coworkers, where OE-DNP enhanced ^{19}F—^{13}C INEPT (Fig. 22d) and its 2D analog, ^{19}F—^{13}C HETCOR, of the antifungal drug flutrimazole (Fig. 24) were reported. [39] In particular, INEPT-mediated hyperpolarization transfer achieved ^{13}C enhancements of as much as 100-fold in fluorinated small molecules relative to thermal pulse-acquire ^{13}C spectra, arising from $\gamma_{19F}/\gamma_{13C} \sim 3.7$ and $\epsilon(^{19}F) \sim 25$. [39] For non-viscous samples, direct ^{1}H OE-DNP is significantly less efficient, thus precluding the analogous ^{1}H-heteronuclear hyperpolarization transfer experiment. Conversely, ^{1}H signal can be enhanced by

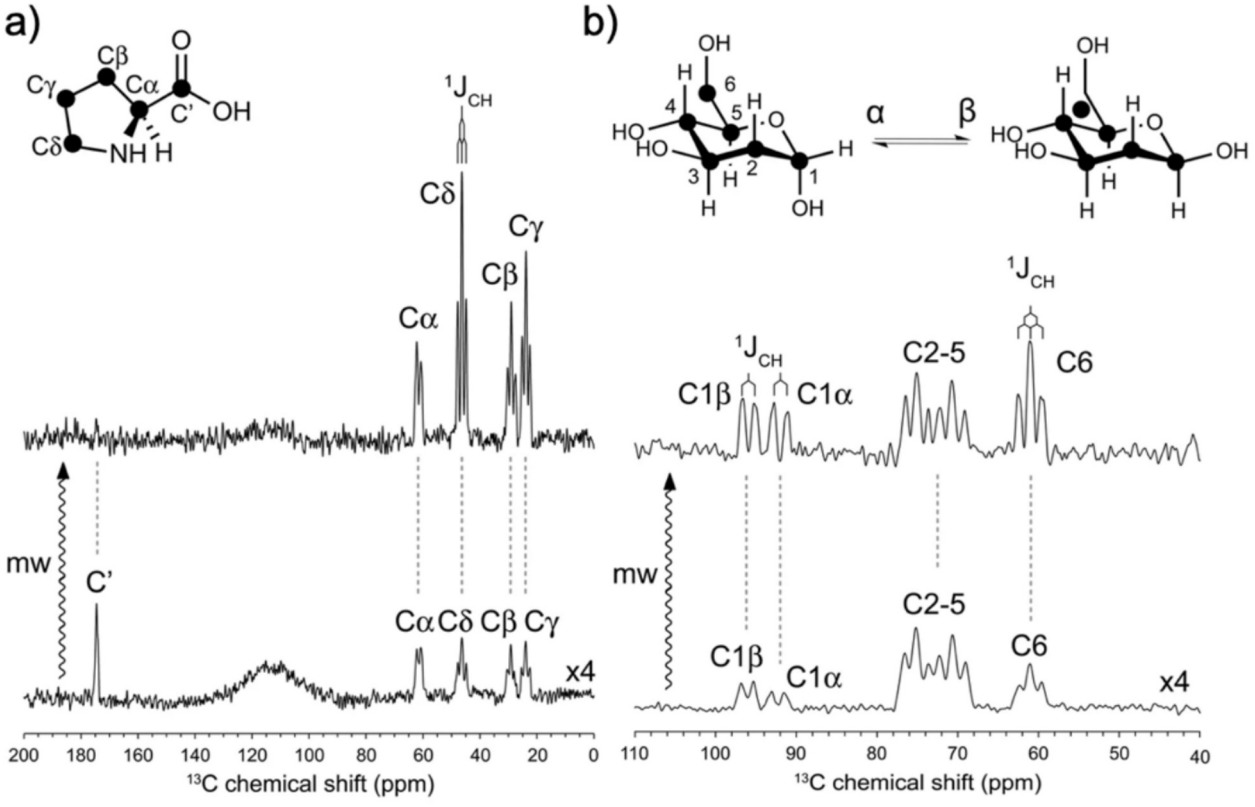

Fig. 25. OE-DNP enhanced (top row) and thermal (bottom row) ^{13}C NMR spectra of aqueous solutions of (a) 2 M proline-$^{13}C_5$ and (b) 2 M glucose-$^{13}C_6$ doped with 0.1 M TEMPOL at 9.4 T. Adapted from ref. [75].

^{13}C—^{1}H hyperpolarization transfer using reverse-INEPT in ^{13}C-enriched compounds, as demonstrated by Rao and coworkers at 9.4 T and by Soundararajan and coworkers at 14.1 T. [178,181].

Incoherent transfer schemes have also been explored for hyperpolarizing solution samples via a solid-to-liquid nuclear Overhauser effect (NOE). Solid-state polarization sources include optically-hyperpolarized 5,12-diazatetracene-doped *p*-terphenyl nanocrystals [280] and nanodiamond [281], as well as micrometer-scale polystyrene particles hyperpolarized by SE-DNP [282], as demonstrated by Matsumoto, Eichhorn, Wi, and others. In these cases, the paramagnetic agent either decays (as a transient triplet state) or is spatially separated (solid-to-liquid) from the target nuclei during the NOE step, thereby avoiding strong paramagnetic relaxation that would otherwise dominate. Nevertheless, the polarization transfer efficiency across the solid-liquid interface still needs further investigation and improvement. Developing a practical protocol for NOESY (nuclear Overhauser effect spectroscopy) hyperpolarization transfer under the conditions of OE-DNP is still an open challenge (particularly if the aim is to use semi-quantitative interpretation of NOESY cross-peak intensity data to aid structure determination [283,284]).

5.2.2. OE-DNP study of biological small molecules

Recent developments of liquid-state OE-DNP have brought forth structural analysis of a variety of biologically active molecules with ^{1}H, ^{13}C, and ^{19}F hyperpolarization. Early investigation by Krummenacker and coworkers observed relatively modest ($|\varepsilon| < 2$) ^{1}H enhancements for the metabolites of pyruvate, lactate, and alanine in aqueous solution at 9.2 T using the helical cylindrical resonator described in Fig. 12. [219] Later studies by Orlando and coworkers achieved $\varepsilon = 13 \pm 3$ for the methyl carbon of pyruvic acid using the same resonant probehead design. [114] More recently, hardware developments have further enabled analysis of biologically active molecules with improved chemical shift resolution and sensitivity. For instance, Dai and coworkers performed ^{13}C OE-DNP on glucose and amino acids in water using nitroxide polarizing agents and a resonant probehead equipped with a Fabry-Pérot resonator (Fig. 13), resulting in 2–10-fold enhancements (Fig. 25). [75] Levien, Reinhard, and others reported 2- to 25-fold ^{13}C and ^{19}F enhancements for several pharmaceuticals and inhibitors in various solvents using an NMR-optimized setup (Fig. 16). [39,40,285] Nevertheless, demonstrations so far have been mainly focused on molecules with low molecular weight ($\leq$ 600–700 Da). Achieving efficient OE-DNP enhancement for biological macromolecules, which exhibit much slower dynamics, will likely require development of polarizing agents with tailored non-covalent interactions (see sections 2.3 and 5.1.1). Alternatively, an OE-DNP hyperpolarized (non-viscous) solvent matrix may act as an intermediate, enhancing the analyte NMR signal by polarization transfer. Similar strategies have been employed in dissolution DNP and solution-state photo-CIDNP to extract information about solvent accessibility, protein-ligand binding structure, selectivity, and dynamics, by studying biological macromolecules in presence of hyperpolarized solvent or ligand. [13,36,196,286–288] Valentine and coworkers demonstrated that the ^{1}H NMR signal of water can be enhanced by about two orders-of-magnitude ($\varepsilon(^{1}H) = -93 \pm 23$) at 0.35 T when encapsulated together with flavodoxin protein inside reverse micelles dispersed in perdeuterated hexane. [289] Although biological macromolecular hyperpolarization was not demonstrated experimentally, the authors proposed that incoherent polarization transfer from the hyperpolarized water matrix should polarize the protein. One potential challenge for investigating biological samples using liquid-state OE-DNP is that the biological matrix per se, consisting of aqueous buffers, likely induces large dielectric loss. This reduces MW and DNP efficiency while generating a strong heating effect, even with a resonant probe head design (for example, see section 5.1.2). The sample preparation method reported by Valentine and coworkers presents a possible solution to this issue – encapsulation in reverse micelles and dispersion in a low-dielectric-loss solvent could help mitigate MW attenuation and heating for measuring aqueous samples. [289] So far, experimental demonstration of this strategy at high magnetic fields still remains an open challenge.

Another important aspect of NMR analysis of complex mixtures is the quantification of different chemical components based on their respective signal intensities. In OE-DNP, quantification becomes less straightforward because the enhancement factors tend to be specific to the nuclear chemical environment. A recent work by van der Ham attempted to recover the peak intensity proportionality of different ^{13}C in the same molecule by back-extrapolation – OE-DNP spectra were collected with gradually reduced duration of MW irradiation, and the peak intensities were fitted to a DNP build-up curve governed by nuclear T_{1n}. [290] Application of this method to a model system of iodobenzene-$^{13}C_6$ solution in toluene doped with TEMPONE-^{15}N-d_{16} showed good agreement with the expected relative integrals of the two molecules. Alternatively, Phuong and coworkers developed a quantification scheme for ^{1}H and ^{13}C OE-DNP-enhanced acetonitrile-water binary mixtures using a flow-OE-DNP setup (hyperpolarization at 0.35 T, detection at 1.0 T). [291] The authors established a series of calibration curves with respect to the analyte molar fractions, which were non-linear due to possible influences from non-uniform enhancement and relaxation during sample transport. However, quantification in the conventional sense, i.e., extraction of the absolute concentration/mass of a compound in a static hyperpolarized mixture [292], has not yet been demonstrated for OE-DNP.

In comparison to the OE-DNP mechanism, which has highest efficiency at high magnetic field for molecular motions with very short correlation times, the DNP effects induced by anisotropic dipolar hyperfine coupling present a promising alternative for hyperpolarizing systems with slow dynamics. An early example was presented by Jakdetchai and coworkers, where OE-type ^{1}H enhancement up to -15 was achieved at ambient temperature for the acyl chain protons of aligned 1,2-dioleoyl-*sn*-glycero-3-phosphocholine (DOPC) lipid bilayer doped with nitroxide radical. [109] Kuzhelev and coworkers showed SE-type ^{1}H enhancement up to ± 12 when BDPA was used to hyperpolarize 1,2-dimyristoyl-*sn*-glycero-3-phosphocholine bilayer. [103] SE-DNP of slowly-tumbling liquid samples also allowed ^{1}H enhancements of 35–55 for a tripeptide dissolved in glycerol, and ^{31}P enhancements of $\sim$20 for a 25-mer DNA duplex dispersed in deuterated water. [107] The above evidence indicates that SE-DNP could serve as a complimentary mechanism for continuous hyperpolarization of slow-tumbling liquid and viscous samples, which is particularly relevant for studying biological systems. Finally, it should be noted that ^{1}H OE-DNP has been extensively used by Han, Franck, Armstrong, McCarney and others to study local water dynamics of lipid vesicles, proteins, and polymers. [293–295] As small molecule spin probes, such as nitroxide polarizing agents, are doped into biomacromolecules and soft matter, they experience different translational and rotational diffusion correlation times depending on whether they are situated at the surface or interior of the substrate. Subsequently, this leads to differences in OE-DNP coupling factors, which are best characterized at X-band. However, this topic has already been comprehensively reviewed in the past literature [51,296,297], thus will not be further discussed here.

5.2.3. Application of OE-DNP in reaction monitoring and surfaces

One important application of liquid-state NMR is the monitoring of chemical reactions, thanks to its non-invasive nature, ability to resolve chemical structure, provide quantitative information, and evaluate reaction dynamics. Towards this end, hyperpolarization could further promote this application by enabling detection of low-concentration reaction intermediates and acceleration of reaction screening, which are critical for mechanism elucidation [298], catalysis optimization [299], drug discovery [300,301], process control [302], and related fields. To date, multiple examples of reaction monitoring using hyperpolarized liquid-state NMR, specifically dissolution DNP and PHIP/SABRE, have been demonstrated, including studies of organic [303,304], hydrogenation [211,305,306], polymerization [307], and enzymatic [308] reactions. Nevertheless, due to the single-shot nature of

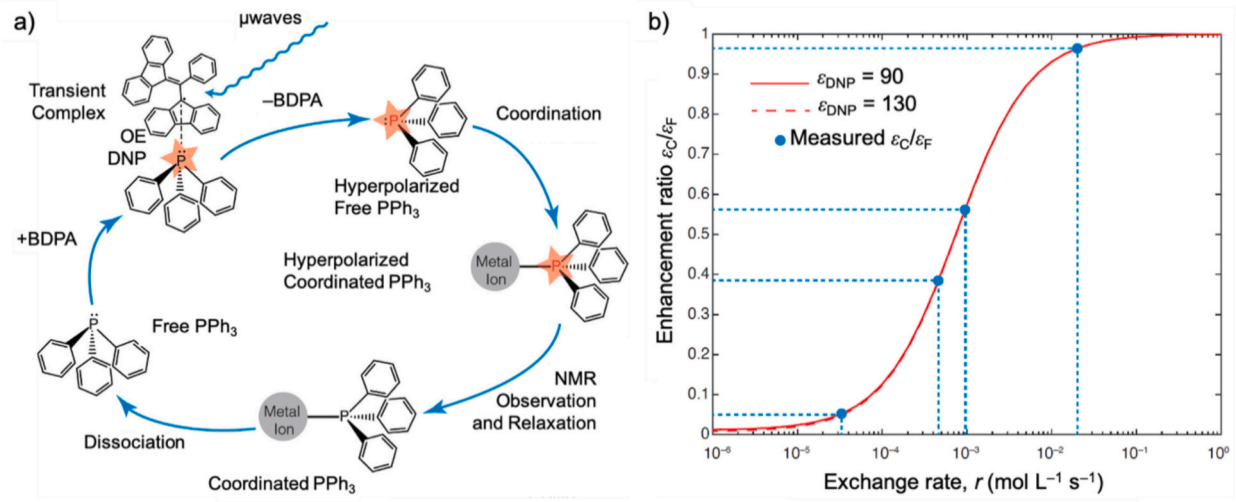

Fig. 26. (a) Schematic of hyperpolarization of transition metal bound PPh_3 through chemical exchange with OE-DNP enhanced free ligand. (b) Enhancement ratio of bound (ε_C) and free (ε_F) PPh_3 (blue dots) as a function of the ligand exchange rate obtained from pre-saturated OE-DNP pulse-acquire experiments. Adapted from ref. [182].

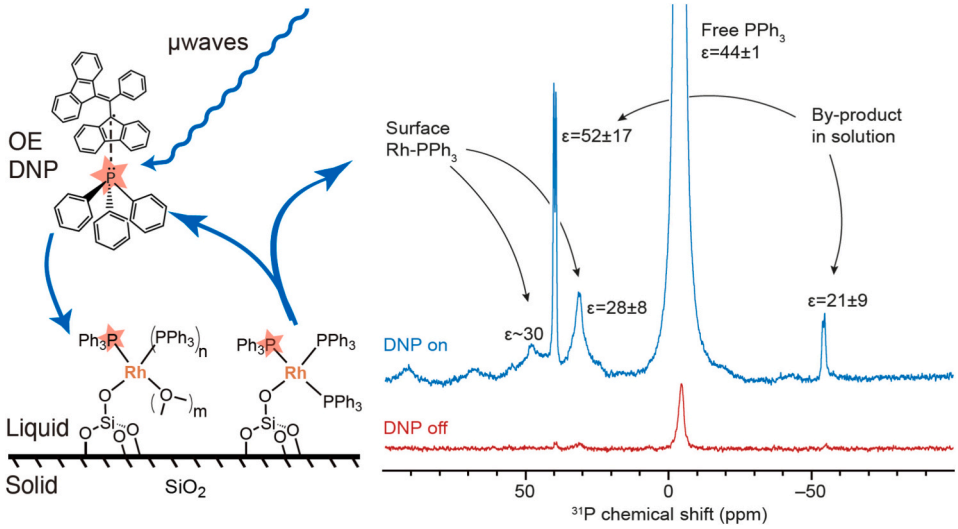

Fig. 27. Schematic representation of the exchange-mediated polarization transfer pathway for enhancing NMR signals of surface species at solid-liquid interfaces, together with the OE-DNP-enhanced ^{31}P NMR spectrum (blue) acquired using this strategy. The NMR spectrum measured with off-resonance MW irradiation (red) is provided as a reference in the absence of DNP. Adapted with permission from ref. [183]. (For interpretation of the references to colour in this figure legend, the reader is referred to the web version of this article.)

these techniques, observation windows are typically limited to the nuclear T_1 relaxation time, and quantification must rely on NMR peak ratios [308] or careful modeling of the nuclear spin relaxation dynamics [304,305,307].

Because OE-DNP allows a continuous supply of hyperpolarization, in principle this method is suited for monitoring chemical reactions. Rao and coworkers demonstrated this capacity by tracking ligand exchange reactions of the homogeneous catalysts $[Rh(PPh_3)_3Cl]$, $[Ru(PPh_3)_3Cl_2]$, $[Pd(PPh_3)_2Cl_2]$ and $[Pt(PPh_3)_2Cl_2]$, using ^{31}P OE-DNP at 9.4 T. [182] For this system, metal-bound PPh_3 is challenging to hyperpolarize directly because the phosphorous lone pair responsible for efficient OE-DNP (see section 5.1.4) is engaged in metal complexation. Nevertheless, hyperpolarization was successfully relayed to the bound ligands via chemical exchange with free PPh_3, which exhibits strong OE-DNP efficiency (Fig. 26a). This strategy led to 50- to 130-fold enhancements for the bound PPh_3, with the latter value close to the enhancement of free PPh_3. Furthermore, kinetic modeling of the DNP and ligand exchange processes allowed estimation of the exchange rates as a function of temperature (275–314 K) for the $[Pd(PPh_3)_2Cl_2]$ model system. The exchange rate relates to the enhancements and T_1 of the free and bound PPh_3 when pulse-acquire acquisitions were performed with pre-saturation (Fig. 26b). An activation energy of 28 ± 10 kcal/mol was subsequently extracted, in agreement with literature reports obtained by spectroscopic and computational methods. [182] Additionally, it is worth noting that conventional NMR analysis of chemical exchange based on saturation transfer typically detects <70% differences relative to the thermal Boltzmann signal. [309,310] OE-DNP, in contrast, provides 10^1–10^2-fold enhancements, thus enabling much higher signal-to-noise for analyzing exchange processes.

More recently, this combined approach of OE-DNP and chemical exchange has been applied by the same authors to probe PPh_3 bound to the surface of silica at the solid-liquid interface. [183] Conventional DNP SENS (Surface Enhanced NMR Spectroscopy [311,312]) requires sample freezing to enable efficient solid-state DNP mechanisms and

polarization transfer, thus limiting its applicability to study interfaces under operational conditions. OE-DNP, when combined with chemical exchange, provides an alternative room-temperature approach for enhancing NMR signals at solid-liquid interfaces. Using a silica-supported Rh(I)-phosphine complex, Rao, Gioffrè, and co-workers demonstrated ^{31}P DNP enhancement of the ligands of surface sites by up to a factor of 30 at 9.4 T. [183] In this approach, hyperpolarized PPh_3 is exchanged between the liquid solution and the solid-liquid interface, enabling the detection and monitoring of various species, including surface Rh-PPh_3 sites, free PPh_3 in solution, and a cyclometalated byproduct (Fig. 27).

6. Outlook

The past decade has witnessed developments of high-field liquid-state OE-DNP as a promising method for enhancing the sensitivity of high-resolution NMR for routine chemical analysis. Emerging examples are showcasing the practical applications of OE-DNP, as in structural elucidation of small molecules, reaction monitoring, and study of biological systems in the context of chemical and biological analysis. These potential applications span the characterization of pharmaceuticals, natural products, small quantities of synthetic material, such as *per*- and polyfluoroalkyl substances (PFAS) in the context of environmental sciences, as well as homo- to heterogeneous catalysis. Particularly, OE-DNP is compatible with enhancing routine one- and two-dimensional liquid-state NMR spectroscopy. Enhancements of up to two orders of magnitude have been achieved on ^{13}C and ^{19}F for small molecules, and the nuclear polarization can be transferred from highly enhanced sites across networks of coupled nuclei through conventional NMR coherence transfer experiments. Evidence so far suggests no discernible sample degradation during OE-DNP experiments when the sample temperature is adequately controlled through active cooling.

Although direct OE-DNP enhancements in liquids are typically two to three orders of magnitude smaller than those obtained with other hyperpolarization methods, the in situ and steady-state nature of OE-DNP offers several advantages. OE-DNP is compatible with long-term signal averaging (e.g. over days), indirect-dimension incrementation in multidimensional NMR experiments, and repeated polarization transfer to other nuclei on timescales surpassing the nuclear T_{1n} relaxation times. At present, the direct OE-DNP approach is most efficient for small molecules, and a key future challenge is achieving hyperpolarization to macromolecules. In this regard, polarization transfer methods based on ligand exchange, in analogy to those developed for dissolution DNP, may prove promising for OE-DNP.

On the mechanistic side, we foresee that advances in computational methods – including molecular dynamics simulations, hyperfine coupling calculations, and, eventually, modeling of coupling factors – will play a central role in optimizing OE-DNP polarizing agents and experimental conditions for specific analytes of interest. For instance, nitroxide radicals were found to be highly efficient for ^{13}C OE-DNP, yet comparatively inefficient for ^{19}F OE-DNP, whereas BDPA exhibits superior efficiency for hyperpolarizing ^{31}P of PPh_3. These observations underscore that polarizing agents must be tailored to the electronic structures and chemical properties of the target analyte. On the other hand, experimental screening of polarizing agents with various electronic properties in liquids at high magnetic fields remains a challenge, due to the short electron relaxation times and, in particular, the narrow EPR resonances that are *g* factor dependent. These constraints are often difficult to satisfy with fixed MW frequencies and NMR magnetic fields. Therefore, rational, model-guided searches of polarizing agents will likely become a more productive approach for the future.

On the hardware side, future developments will likely focus on improving the electron saturation factors, and simultaneously on increasing sample volumes – which are currently still at least 10-fold smaller than those of a standard 5 mm NMR tube. Present high-field OE-DNP setups that can accommodate large ($\geq$ μL) sample volumes have reported saturation factors no higher than ~0.3 for nitroxides. This indicates that an approximately three-fold increase in the enhancements should still be attainable. In the meantime, reducing MW losses could also allow the use of lower-cost MW sources while maintaining sufficient electron saturation. Nevertheless, gyrotrons are already established in the solid-state DNP community, so that existing infrastructure can be adapted for OE-DNP by implementing dedicated probe heads, which are becoming commercially available. This strategy may particularly facilitate extending OE-DNP to even higher magnetic fields, where multiple high-frequency gyrotrons have been already installed in NMR facilities. Additional future improvements could include integration of OE-DNP with cryogenic probe technologies to further increase sensitivity, as has been explored in the context of solid-state DNP.

Overall, we foresee that OE-DNP will become a powerful complement to existing hyperpolarization techniques. As NMR is a central analytical technique for complex chemical and physical environments, OE-DNP might offer attractive opportunities. The synergy with other, previously developed, hyperpolarization methods will boost future research with new transformative strategies for NMR-based analysis of chemical, physical, and biological systems.

CRediT authorship contribution statement

Luming Yang: Writing – review & editing, Writing – original draft, Project administration, Conceptualization. **Igor Tkach:** Writing – review & editing, Writing – original draft. **Alex van der Ham:** Writing – review & editing, Writing – original draft. **Maik Reinhard:** Writing – review & editing, Writing – original draft. **Yu Rao:** Writing – review & editing, Writing – original draft. **Tamar Wolf:** Writing – review & editing, Writing – original draft. **Ilya Kuprov:** Writing – review & editing, Writing – original draft. **Marcel Levien:** Writing – review & editing, Writing – original draft. **Tomas Orlando:** Writing – review & editing, Writing – original draft. **Marina Bennati:** Writing – review & editing, Writing – original draft, Supervision, Project administration, Funding acquisition, Conceptualization.

Declaration of competing interest

The authors declare that they have no known competing financial interests or personal relationships that could have appeared to influence the work reported in this paper.

Acknowledgements

This work was supported by the European Research Council (ERC) Advanced Grant 101,020,262 BIO-enMR to M.B. and the Max Planck Society. L.Y. acknowledges the Alexander von Humboldt Foundation for a Postdoctoral Fellowship. M.R., L.Y., M.B. acknowledge the DFG through the BENCh Research Training Group – 389,479,699/GRK2455. T.O. acknowledges the National Science Foundation (DMR-2128556) and the State of Florida for funding of the NHMFL. M.L. acknowledges funding by SNSF for a Swiss Postdoctoral Fellowship Grant No. 234089. We thank Sergei Kuzin for proof-reading the manuscript.

Appendix A. Summary of OE-DNP enhancements at 9.2/9.4 and 14.1 Tesla

Table A1
9.4 T ^{13}C liquid-state OE-DNP enhancements measured with an NMR-optimized setup. Samples were doped with 0.025 M TEMPONE-^{15}N-d_{16} unless otherwise noted. FG represents the chemical functionality of the nucleus (CX_n: polyhalogenated carbon; C_α: α- to electron-withdrawing group; C=O: carbonyl; C_H=O: aldehyde; C_H(Ar): aryl protonated carbon; C_H(Alk): alkyl protonated carbon; C_q: quaternary carbon; C_X: halogenated carbon). Error for ε is about ±10%.

Compound	FG	ε	Reference
CCl_4 (neat)	CX_n	120	[40]
$CHCl_3$-^{13}C (0.2 M in CCl_4)	CX_n	200	
Ethyl acetoacetate-1,2,3,4–$^{13}C_4$ (< 0.5 M in CCl_4)	C_α	10–12	
	C=O	-*	
3-hydroxybut-2-enoate-1,2,3,4–$^{13}C_4$ (tautomer of ethyl acetoacetate) (< 0.5 M in CCl_4)	C_α	7–9	
	C=O	–	
	Enol	–	
Benzene-$^{13}C_6$ (0.2 M in CCl_4)	C_H(Ar)	7	
Fluorobenzene-$^{13}C_6$ (0.5 M in CCl_4)	C_F	–	
	C_H(Ar)	6–8	
Chlorobenzene-$^{13}C_6$ (0.5 M in CCl_4)	C_{Cl}	2	
	C_H(Ar)	9–10	
Bromobenzene-$^{13}C_6$ (0.5 M in CCl_4)	C_{Br}	3	
	C_H(Ar)	9–10	
Iodobenzene-$^{13}C_6$ (0.5 M in CCl_4)	C_I	25	
	C_H(Ar)	9	
p-Iodofluorobenzene (1.5 M in cyclohexane)	C_I	25	
	C_F	–	
	C_H(Ar)	15–20	
E-Hexenyl acetate (0.5 M in CCl_4)	C_α	14	
	C=O	–1	
	C_H(Alk)	4	
	C=C	4–5	
ST034307 inhibitor (0.1 M in benzene)	CX_n	25	
	C_{Cl}	4	
	C_H(Ar)	4–11	
	C_q	–	
Phenylacetaldehyde (~ 1 M in CCl_4)	C_H=O	13	
	C_α	6	
	C_H(Ar)	6–7	
	C_q	2	
Guaiazulene (0.5 M in 9:1 CCl_4:$CHCl_3$)	C_H(Alk)	3–6	
	C_H(Ar)	2–3	
	C_q	0–1	
p-Cymeme (neat)	C_H(Ar)	6	
	C_H(Alk)	3–8	
	C_q	–	
Mitotane (0.5 M in CCl_4)	CX_n	12	
	C_{Cl}	1–2	
	C_H(Alk)	2	
	C_H(Ar)	2–3	
	C_q	1	
Amiodarone hydrochloride (0.4 M in $CHCl_3$)	C_I	10	
	C_H(Alk)	2–4	
	C_H(Ar)	2–3	
	C_q	–	
Sodium diatrizoate (0.5 M in 9:1 H_2O:Glycerol) (contains 0.5 M CH_3CN-^{13}C For field optimization)	C_I	5–6	
	C_α	1	
	C=O, C_q	–	
Sodium pyruvate (0.5 M in 9:1 H_2O:Glycerol)	C_α	3	[184]
Pentafluoroiodobenzene (0.6 M in CCl_4)	C_I	130	[198]
	C_F	–	
Pentafluorobromobenzene (0.6 M in CCl_4)	C_{Br}	20	
	C_F	–	
Pentafluorochlorobenzene (0.6 M in CCl_4)	C_{Cl}	3	
	C_F	–	
4-Iodoanisole (0.3 M in CCl_4)	C_I	12	
	C_H(Ar)	6–7	
	C_q	–	
4-Iodotoluene (0.6 M in CCl_4)	C_I	17	
	C_H(Ar)	7–8	
	C_q	–	

(*continued on next page*)

Table A1 (*continued*)

Compound	FG	ε	Reference
1-Bromo-4-iodobenzene	C_I	32	
(0.3 M in CCl_4)	C_H(Ar)	9–14	
	C_{Br}	3	
1-Fluoro-4-iodobenzene	C_I	35	
(0.3 M in CCl_4)	C_H(Ar)	13	
	C_F	–	
1-Chloro-4-iodobenzene	C_I	41	
(0.3 M in CCl_4)	C_H(Ar)	13–16	
	C_{Cl}	3	
1-Fluoro-2-iodobenzene	C_I	44	
(0.6 M in CCl_4)	C_H(Ar)	8–12	
	C_F	–	
2,4-Difluoroiodobenzene	C_I	55	
(0.6 M in CCl_4)	C_H(Ar)	15–20	
	C_F	–	
2,3,4-Trifluoroiodobenzene	C_I	76	
(0.6 M in CCl_4)	C_H(Ar)	14–16	
	C_F	–	
CBr_4–^{13}C	CX_n	180	
(0.6 M in CCl_4)			

* $|\varepsilon| < 1$.

Table A2
9.4 T ^{13}C liquid-state OE-DNP enhancements measured with a resonant setup equipped either with a helical cylindrical or a Fabry-Pérot resonator. Measurements in ref. [114] were performed with 0.1 M TEMPONE-^{15}N-d_{16}. Measurements in refs. [75] and [136] were performed with 0.1 M TEMPOL unless otherwise noted. FG represents the chemical functionality of the nucleus.

Compound	FG	ε	Reference
CCl_4–^{13}C	CX_n	430 ± 50	[114]
(neat)			Helical cylindrical resonator
$CHCl_3$-^{13}C	CX_n	320 ± 60	
(neat)			
CBr_4–^{13}C	CX_n	600 ± 60	
(~ 3 M in CCl_4)			
Diethyl malonate-1,2,3-$^{13}C_3$	C_α	30 ± 10	
(neat)	C=O	–	
Ethyl acetoacetate-2,4–$^{13}C_2$	C_α	13–18 ± 1–2	
(neat)			
Pyruvic acid-3-^{13}C	C_α	13 ± 3	
(77:100 M/M in diisopropyl ether, with 1.5:1 M/M pyridine)			
Indole-2-^{13}C	C_H(Ar)	14.1 ± 2.5 (C2)	[75]
(0.1 M TEMPO)			Helical cylindrical resonator
(2 M in CCl_4)			
Indole-$^{13}C_8$	C_H(Ar)	26.2 ± 2.4 (C2)	
(0.1 M TEMPO)		5.4 ± 0.2 (C4–6)	
(2 M in CCl_4)		11.6 ± 1.1 (C3)	
		20.7 ± 2.5 (C7)	
	C_q	−1.8 to −2.1 ± 0.5	
Imidazole-2-^{13}C-1,3-$^{15}N_2$	C_H(Ar)	> 0	
(2 M in D_2O)		(low SNR due to severe sample heating)	
Imidazole-2-^{13}C-1,3-$^{15}N_2$	C_H(Ar)	50 ± 10	[75]
(2 M in D_2O)			Fabry-Pérot resonator
Glucose-$^{13}C_6$	C_α*	2.2–6.9 ± 0.4–2.2	
(2 M in H_2O)			
Glycine-$^{13}C_2$	C_α*	10.7 ± 1.7	
(2 M in H_2O)	C=O	~ −1	
Alanine-$^{13}C_3$	C_α*	6.0 ± 1.6	
(1.4 M in H_2O)	C_H(Alk)	6.1 ± 2.2	
	C=O	~ −1	
Serine-$^{13}C_3$	C_α*	6.0–6.5 ± 0.1	
(2 M in H_2O)	C=O	~ −1	
Proline-$^{13}C_5$	C_α*	4.5–10.5 ± 0.5–0.8	
(2 M in H_2O)	C_H(Alk)	6.9–8.2 ± 0.7	
	C=O	~ −1	
Sodium pyruvate-3-^{13}C	C_α	16	[136]
(1 M in H_2O)		(at 340 K)	Fabry-Pérot resonator

* For glucose and amino acids, C_α here refers to the carbon atoms α- to an electron-withdrawing group.

Table A3
9.4 T ^{13}C liquid-state OE-DNP enhancements measured with a MAS-DNP setup described in ref. [181]. Samples were doped with 0.01 M TEMPO-NE-^{15}N-d_{16}.

Compound	FG	ε
$CHCl_3$-^{13}C (neat)	CX_n	50.8
1,1,2,2-$C_2H_2Cl_4$–1,2 (neat)	CX_n	8.6
Phenylacetylene-2 (neat)	C_H(alkyne)	7.3

Table A4
14.1 T ^{13}C liquid-state OE-DNP enhancements measured with a MAS-DNP setup described in ref. [114]. Samples were doped with 0.01 M TEMPO-NE-^{15}N-d_{16} unless otherwise noted.

Compound	FG	ε
CCl_4–^{13}C (neat)	CX_n	23 ± 5
$CHCl_3$-^{13}C (neat)	CX_n	17.5 ± 2
CBr_4 (5% ^{13}C-enriched) (~ 0.19 M in CCl_4)	CX_n	35 ± 3
CCl_4–^{13}C (0.01 M FN2a) (neat)	CX_n	2.9 ± 0.3

Table A5
14.1 T ^{13}C liquid-state OE-DNP enhancements measured with a non-resonant setup described in ref. [137]. Samples were doped with 0.01 M TEMPO. Solvents were n-pentane-d_{12} unless otherwise noted.

Compound	FG	ε	Reference
CCl_4–^{13}C (9% v. with 1% v. $CHCl_3$-^{13}C)	CX_n	21 ± 1	[134]
$CHCl_3$-^{13}C (1% v. with 9% v. CCl_4–^{13}C)	CX_n	70 ± 7	
CCl_4–^{13}C (7% v. with 7% v. $CDCl_3$-^{13}C)	CX_n	20 ± 1	
$CDCl_3$-^{13}C (7% v. with 7% v. CCl_4–^{13}C)	CX_n	52 ± 1	
Phenylacetylene-2-^{13}C (5% v. with 5% v. CCl_4–^{13}C)	$C \equiv C_H$ (protonated)	35 ± 6	
CCl_4–^{13}C (5% v. with 5% v. Phenylacetylene-2-^{13}C)	CX_n	26 ± 2	
n-pentane-d_{12} (as solvent, ≥ 86% v.)	C-D(Alk)	1	
CCl_4–^{13}C (8% v. with 2% v. $CHCl_3$-^{13}C) (solvent: n-hexane-d_{14})	CX_n	4.3 ± 0.1	[178]
$CHCl_3$-^{13}C (2% v. with 8% v. CCl_4–^{13}C) (solvent: n-hexane-d_{14})	CX_n	21 ± 1	
Indole-$^{13}C_8$ (0.44 M in 4:1 n-heptane-d_{16}:Xylene-d_{10})	C_H(Ar)	1–3 ± 0.2	
Phenylacetylene-2-^{13}C (0.32 M in 3:1 n-heptane-d_{16}:Toluene-d_8)	$C \equiv C_H$ (protonated)	10.4 ± 0.4	

Table A6
9.2–9.4 T ^{1}H liquid-state OE-DNP enhancements measured with resonant setups described in refs. [46,115,135,136]. Negative and positive enhancements correspond to OE-DNP and SE-DNP, respectively.

Compound	FG	P_{MW} (W)	Temperature (K)	ε	Reference
H_2O (1 M TEMPOL)	OH	~ 0.1	318	−14	[152]
		1	433	−83	

(continued on next page)

Table A6 (*continued*)

Compound	FG	P_{MW} (W)	Temperature (K)	ε	Reference
H_2O (65 mM Fremy's salt-^{15}N) (0.05 M K_2CO_3)		0.6	333	−38	[139]
H_2O (40 mM Fremy's salt-^{15}N) (0.05 M K_2CO_3)		0.045	~ 318	−10.4	[116]
H_2O (50 mM TEMPOL-^{15}N)		0.045		−6.2	
H_2O (80 mM TEMPOL)		70	~ 313	−10	[138]
Sodium pyruvate (1 M in D_2O/H_2O) (12 mM TEMPOL)	CH_3	0.045	~ 313	−1.6	[219]
Sodium lactate (1 M in D_2O/H_2O) (12 mM TEMPOL)	CH_3			−1	
Alanine (1 M in D_2O/H_2O) (12 mM TEMPOL)	CH_3			−0.7	
DMSO (1 M TEMPOL)	CH_3	0.45	~ 440	−29	[231]
Acetone (1 M TEMPOL)	CH_3		~ 403	−33	
Toluene (1 M TEMPOL)	CH_3		~ 310	−18	
	CH(Ar)			−18.3	
Imidazole-2-^{13}C-1,3-$^{15}N_2$ (0.1 M TEMPO) (1 M in $CDCl_3$)	CH(Ar)	1.4	~ 300	−4.0 to −5.2	[75] Helical cylindrical resonator
Imidazole-2-^{13}C-1,3-$^{15}N_2$ (0.1 M TEMPOL) (2 M in D_2O)				−12.3 to −18.7	
Indole-$^{13}C_8$ (0.1 M TEMPO) (2 M in CCl_4)	CH(Ar) NH			−1.5 to −11.8 −9.5	
Imidazole-2-^{13}C-1,3-$^{15}N_2$ (0.1 M TEMPOL) (2 M in D_2O)	CH(Ar)	5.5		−5.0	[75] Fabry-Pérot resonator
Glucose-$^{13}C_6$ (0.1 M TEMPOL) (2 M in H_2O)	CH			−8.3	
Glycine-$^{13}C_2$ (0.1 M TEMPOL) (2 M in H_2O)	CH			−10.0	
Alanine-$^{13}C_3$ (0.1 M TEMPOL) (1.4 M in H_2O)	CH			−10.2 (overlaps with H_2O)	
Serine-$^{13}C_3$ (0.1 M TEMPOL) (2 M in H_2O)	CH			−7.0 (overlaps with H_2O)	
Proline-$^{13}C_5$ (0.1 M TEMPOL) (2 M in H_2O)	CH CH			−2.9 −7.0 (overlaps with H_2O)	
DMSO (50 mM TEMPOL)	CH_3	0.23	~ 383	−7.2	[63]
DMSO (50 mM nitroxides)				−2.7 to −6.6	
DMSO (1 M TEMPOL)		0.75	~ 473	−32	
DMPC (1:39 M ratio, TEMPOL)	Acyl chain	5	~ 298	−5	[28,109]
DMPC (1:78 M ratio, bTbK)				−14	
DMPC (1:78 M ratio, TOTAPOL)				−15	
DMPC (BDPA, D_2O) (BDPA/DPMC/D_2O molar ratio 1/10/500)		5	~ 320	12	[103]
Triglycine (25 mM OX063)	CH_2	5	~ 315	35	[104]
Glypromate (25 mM OX063)	CH_2			55	

Table A7
9.4 T ^{19}F liquid-state OE-DNP enhancements measured with an NMR-optimized setup. Samples of 0.5 M of target were doped with 0.010 M galvinoxyl and dissolved in CCl_4 unless otherwise noted. FG represents the chemical functionality of the nucleus.

Compound	FG	ε	Reference
Fluorobenzene (0.5 M in CCl_4)	FC (Ar)	23 ± 2	[40]*
α,α,α-trifluorotoluene	CF_3	10 ± 1	
Diethyl fluoromalonate	FCH (Alk)	16 ± 2	
Decafluoropentane	CF_3	9 ± 1	
	CF_2	8–9 ± 1	
	CF	10 ± 1	
Flutamide (0.01 M in 0.33 M DMSO and CCl_4)	CF_3	7 ± 1	
1,4-difluorobenzene	FC (Ar)	20 ± 3	[39]
4-fluoroanisole	FC (Ar)	20 ± 3	
4-fluoroacetophenone	FC (Ar)	20 ± 3	
1-fluoronaphthalene	FC (Ar)	21 ± 4	
3-chloro-4-fluoronitrobenzene	FC (Ar)	14 ± 3	
1-fluoropentane	FCH_2 (Alk)	22 ± 4	
1-fluoropentane (0.025 M TEMPONE-^{15}N-d_{16})	FCH_2 (Alk)	2.3 ± 0.4	
Benzoylfluoride	FC=O	9 ± 2	
Methyl trifluoroacetate	CF_3	9 ± 2	
2,3,4,6-tetra-*O*-acetyl-α-D-glucopyranosyl fluoride (0.4 M in $CHCl_3$)	FCH (Alk)	5 ± 1	
(3-bromophenyl)sulfur pentafluoride	F_1 (ax)	7 ± 2	
	F_2 (eq)	9 ± 2	
L-Fmoc-3-fluorophenylalanine (0.0025 M in 1.2 M $CHCl_3$ and CCl_4)	FC (Ar)	10 ± 2	
L-Fmoc-3-fluorophenylalanyl-L-3-fluorophenylalanine methyl ester (0.0025 M in 1.2 M $CHCl_3$ and CCl_4)	F_1C, F_2C (Ar)	11 ± 2	
Fluorobenzene	FC (Ar)	24 ± 4	
Fluorobenzene (0.025 M TEMPO)	FC (Ar)	3.9 ± 0.6	
Flutrimazole (0.015 M galvinoxyl, 0.1 M in 1.2 M $CHCl_3$ and CCl_4)	F_1 (Ar, ortho)	5 ± 1	
	F_2 (Ar, Para)	10 ± 2	
Hexafluorobenzene	FC (Ar)	16 ± 3	
Hexafluorobenzene (0.025 M TEMPO)	FC (Ar)	1.0 ± 0.2	
Hexafluorobenzene (0.025 M TEMPONE-^{15}N-d_{16})	FC (Ar)	3.4 ± 0.4	[285]
α,α,α-trifluorotoluene (0.025 M TEMPONE-^{15}N-d_{16} in toluene)	CF_3	2.5 ± 0.3	
Diethyl fluoromalonate (0.025 M TEMPONE-^{15}N-d_{16})	FCH (Alk)	2.2 ± 0.3	
4-fluorotoluene	FC (Ar)	23 ± 2	
4-fluoroiodobenzene	FC (Ar)	17 ± 2	
4-fluoronitrobenzene	FC (Ar)	15 ± 2	
1,2-difluorobenzene	FC (Ar)	21 ± 3	
1,3-difluorobenzene	FC (Ar)	19 ± 2	
1,2,4-trifluorobenzene	F_1C (Ar)	21 ± 3	
	F_2C (Ar)	21 ± 3	
	F_4C (Ar)	20 ± 2	
1,2,4,5-tetrafluorobenzene (neat)	FC (Ar)	13 ± 2	
2-fluoronaphthalene	FC (Ar)	21 ± 3	
Pentafluorobenzene (3 M in CCl_4)	FC (ortho)	21 ± 3	
	FC (meta)	22 ± 3	
	FC (Para)	21 ± 3	
Pentafluoroiodobenzene	FC (ortho)	14 ± 2	
	FC (meta)	19 ± 2	
	FC (Para)	18 ± 2	
Sitagliptin (0.01 M in 1.2 M $CHCl_3$ and CCl_4)	F_AC (Ar)	2.4 ± 0.4	
	F_BC (Ar)	3.6 ± 0.6	
	F_CC (Ar)	3.8 ± 0.6	
	CF_3	3.0 ± 0.5	
Fluticasone propionate (0.01 M in 0.21 M DMSO and CCl_4)	F9αC	0.6 ± 0.1	
	F6αCH	6.2 ± 0.7	
	SCH_2F	0.8 ± 0.1	
Sodium tetrakis[3,5-bis(trifluoromethyl) Phenyl]borate (0.01 M in 1.2 M THF and toluene)	CF_3	1.6 ± 0.2	
Fulvestrant (0.01 M in 0.18 M DMSO and CCl_4)	CF_3	3.8 ± 0.4	
	CF_2	0.8 ± 0.1	
Fulvestrant (ethylated) (0.04 M)	CF_3	5.8 ± 0.6	
	CF_2	5.2 ± 0.6	

(*continued on next page*)

Table A7 (*continued*)

Compound	FG	ε	Reference
2-Fluorobenzyl alcohol (0.025 M TEMPO)	FC (Ar)	3.7 ± 0.4	
2,6-Difluorobenzyl alcohol (0.025 M TEMPO)	FC (Ar)	3.3 ± 0.4	

* Note: Enhancements reported in ref. [40] were recorded with a commercial batch of galvinoxyl radical containing diamagnetic impurities and nominal concentration of 0.025 M.

Data availability

Data will be made available on request.

References

[1] J.H. Ardenkjaer-Larsen, G.S. Boebinger, A. Comment, S. Duckett, A.S. Edison, F. Engelke, C. Griesinger, R.G. Griffin, C. Hilty, H. Maeda, G. Parigi, T. Prisner, E. Ravera, J. van Bentum, S. Vega, A. Webb, C. Luchinat, H. Schwalbe, L. Frydman, Facing and overcoming sensitivity challenges in biomolecular NMR spectroscopy, Angew. Chem. Int. Ed. 54 (2015) 9162–9185, https://doi.org/10.1002/anie.201410653.

[2] A.W. Overhauser, Polarization of nuclei in metals, Phys. Rev. 92 (1953) 411–415, https://doi.org/10.1103/PhysRev.92.411.

[3] K.H. Hausser, D. Stehlik, Dynamic nuclear polarization in liquids, in: J.S. Waugh (Ed.), Adv. Magn. Opt. Reson., Academic Press, 1968, pp. 79–139.

[4] W. Müller-Warmuth, K. Meise-Gresch, Molecular motions and interactions as studied by dynamic nuclear polarization (DNP) in free radical solutions, in: J. S. Waugh (Ed.), Adv. Magn. Opt. Reson., Academic Press, 1983, pp. 1–45.

[5] J.F. Jacquinot, W.T. Wenckebach, M. Goldman, A. Abragam, Polarization and NMR observation of ^{43}Ca nuclei in CaF_2, Phys. Rev. Lett. 32 (1974) 1096–1097, https://doi.org/10.1103/PhysRevLett.32.1096.

[6] M.J. Duijvestijn, C. van der Lugt, J. Smidt, R.A. Wind, K.W. Zilm, D.C. Staplin, ^{13}C NMR spectroscopy in diamonds using dynamic nuclear polarization, Chem. Phys. Lett. 102 (1983) 25–28, https://doi.org/10.1016/0009-2614(83)80650-2.

[7] R.A. Wind, M.J. Duijvestijn, C. van der Lugt, A. Manenschijn, J. Vriend, Applications of dynamic nuclear polarization in ^{13}C NMR in solids, Prog. Nucl. Magn. Reson. Spectrosc. 17 (1985) 33–67, https://doi.org/10.1016/0079-6565(85)80005-4.

[8] D.J. Singel, H. Seidel, R.D. Kendrick, C.S. Yannoni, A spectrometer for EPR, DNP, and multinuclear high-resolution NMR, J. Magn. Reson. 81 (1989) 145–161, https://doi.org/10.1016/0022-2364(89)90273-4.

[9] M. Afeworki, S. Vega, J. Schaefer, Direct electron-to-carbon polarization transfer in homogeneously doped polycarbonates, Macromolecules 25 (2002) 4100–4105, https://doi.org/10.1021/ma00042a009.

[10] D.A. Hall, D.C. Maus, G.J. Gerfen, S.J. Inati, L.R. Becerra, F.W. Dahlquist, R. G. Griffin, Polarization-enhanced NMR spectroscopy of biomolecules in frozen solution, Science 276 (1997) 930–932, https://doi.org/10.1126/science.276.5314.930.

[11] J.H. Ardenkjær-Larsen, B. Fridlund, A. Gram, G. Hansson, L. Hansson, M. H. Lerche, R. Servin, M. Thaning, K. Golman, Increase in signal-to-noise ratio of > 10,000 times in liquid-state NMR, Proc. Natl. Acad. Sci. U. S. A. 100 (2003) 10158–10163, https://doi.org/10.1073/pnas.1733835100.

[12] S.J. Elliott, Q. Stern, M. Ceillier, T. El Daraï, S.F. Cousin, O. Cala, S. Jannin, Practical dissolution dynamic nuclear polarization, Prog. Nucl. Magn. Reson. Spectrosc. 126 (2021) 59–100, https://doi.org/10.1016/j.pnmrs.2021.04.002.

[13] C. Hilty, D. Kurzbach, L. Frydman, Hyperpolarized water as universal sensitivity booster in biomolecular NMR, Nat. Protoc. 17 (2022) 1621–1657, https://doi.org/10.1038/s41596-022-00693-8.

[14] C. Griesinger, M. Bennati, H.M. Vieth, C. Luchinat, G. Parigi, P. Hofer, F. Engelke, S.J. Glaser, V. Denysenkov, T.F. Prisner, Dynamic nuclear polarization at high magnetic fields in liquids, Prog. Nucl. Magn. Reson. Spectrosc. 64 (2012) 4–28, https://doi.org/10.1016/j.pnmrs.2011.10.002.

[15] V. Denysenkov, T. Prisner, Liquid-state Overhauser DNP at high magnetic fields, eMagRes 8 (2019) 41–54, https://doi.org/10.1002/9780470034590.emrstm1557.

[16] M. Bennati, T. Orlando, Overhauser DNP in liquids on C-13 nuclei, eMagRes 8 (2019) 11–18, https://doi.org/10.1002/9780470034590.emrstm1581.

[17] R. Kaptein, K. Dijkstra, K. Nicolay, Laser photo-CIDNP as a surface probe for proteins in solution, Nature 274 (1978) 293–294, https://doi.org/10.1038/274293a0.

[18] I. Kuprov, T.D. Craggs, S.E. Jackson, P. Hore, Spin relaxation effects in photochemically induced dynamic nuclear polarization spectroscopy of nuclei with strongly anisotropic hyperfine couplings, J. Am. Chem. Soc. 129 (2007) 9004–9013, https://doi.org/10.1021/ja0705792.

[19] Y. Okuno, S. Cavagnero, Photochemically induced dynamic nuclear polarization: basic principles and applications, eMagRes 6 (2017) 283–314, https://doi.org/10.1002/9780470034590.emrstm1499.

[20] S. Jannin, J.N. Dumez, P. Giraudeau, D. Kurzbach, Application and methodology of dissolution dynamic nuclear polarization in physical, chemical and biological contexts, J. Magn. Reson. 305 (2019) 41–50, https://doi.org/10.1016/j.jmr.2019.06.001.

[21] T. Hamachi, N. Yanai, Recent developments in materials and applications of triplet dynamic nuclear polarization, Prog. Nucl. Magn. Reson. Spectrosc. 142-143 (2024) 55–68, https://doi.org/10.1016/j.pnmrs.2024.05.001.

[22] C.R. Bowers, D.P. Weitekamp, Parahydrogen and synthesis allow dramatically enhanced nuclear alignment, J. Am. Chem. Soc. 109 (1987) 5541–5542, https://doi.org/10.1021/ja00252a049.

[23] M.G. Pravica, D.P. Weitekamp, Net NMR alignment by adiabatic transport of parahydrogen addition products to high magnetic field, Chem. Phys. Lett. 145 (1988) 255–258, https://doi.org/10.1016/0009-2614(88)80002-2.

[24] R.W. Adams, J.A. Aguilar, K.D. Atkinson, M.J. Cowley, P.I. Elliott, S.B. Duckett, G.G. Green, I.G. Khazal, J. Lopez-Serrano, D.C. Williamson, Reversible interactions with Para-hydrogen enhance NMR sensitivity by polarization transfer, Science 323 (2009) 1708–1711, https://doi.org/10.1126/science.1168877.

[25] P.J. Rayner, S.B. Duckett, Signal amplification by reversible exchange (SABRE): from discovery to diagnosis, Angew. Chem. Int. Ed. 57 (2018) 6742–6753, https://doi.org/10.1002/anie.201710406.

[26] G. Buntkowsky, F. Theiss, J. Lins, Y.A. Miloslavina, L. Wienands, A. Kiryutin, A. Yurkovskaya, Recent advances in the application of parahydrogen in catalysis and biochemistry, RSC Adv. 12 (2022) 12477–12506, https://doi.org/10.1039/d2ra01346k.

[27] D.A. Barskiy, S. Knecht, A.V. Yurkovskaya, K.L. Ivanov, SABRE: chemical kinetics and spin dynamics of the formation of hyperpolarization, Prog. Nucl. Magn. Reson. Spectrosc. 114 (2019) 33–70, https://doi.org/10.1016/j.pnmrs.2019.05.005.

[28] J. Eills, D. Budker, S. Cavagnero, E.Y. Chekmenev, S.J. Elliott, S. Jannin, A. Lesage, J. Matysik, T. Meersmann, T. Prisner, J.A. Reimer, H. Yang, I. V. Koptyug, Spin hyperpolarization in modern magnetic resonance, Chem. Rev. 123 (2023) 1417–1551, https://doi.org/10.1021/acs.chemrev.2c00534.

[29] S.J. Nelson, J. Kurhanewicz, D.B. Vigneron, P.E. Larson, A.L. Harzstark, M. Ferrone, M. van Criekinge, J.W. Chang, R. Bok, I. Park, G. Reed, L. Carvajal, E. J. Small, P. Munster, V.K. Weinberg, J.H. Ardenkjaer-Larsen, A.P. Chen, R. E. Hurd, L.I. Odegardstuen, F.J. Robb, J. Tropp, J.A. Murray, Metabolic imaging of patients with prostate cancer using hyperpolarized [1-^{13}C]pyruvate, Sci. Transl. Med. 5 (2013) 198ra108, https://doi.org/10.1126/scitranslmed.3006070.

[30] A. Comment, Dissolution DNP for in vivo preclinical studies, J. Magn. Reson. 264 (2016) 39–48, https://doi.org/10.1016/j.jmr.2015.12.027.

[31] M. Gierse, L. Nagel, M. Keim, S. Lucas, T. Speidel, T. Lobmeyer, G. Winter, F. Josten, S. Karaali, M. Fellermann, J. Scheuer, C. Muller, F. van Heijster, J. Skinner, J. Loffler, A. Parker, J. Handwerker, A. Marshall, A. Salhov, B. El-Kassem, C. Vassiliou, J.W. Blanchard, R. Picazo-Frutos, J. Eills, H. Barth, F. Jelezko, V. Rasche, F. Schilling, I. Schwartz, S. Knecht, Parahydrogen-polarized fumarate for preclinical in vivo metabolic magnetic resonance imaging, J. Am. Chem. Soc. 145 (2023) 5960–5969, https://doi.org/10.1021/jacs.2c13830.

[32] M.M. Chaumeil, J.A. Bankson, K.M. Brindle, S. Epstein, F.A. Gallagher, M. Grashei, C. Guglielmetti, J.D. Kaggie, K.R. Keshari, S. Knecht, C. Laustsen, A. B. Schmidt, D. Vigneron, Y.F. Yen, F. Schilling, New horizons in hyperpolarized ^{13}C MRI, Mol. Imaging Biol. 26 (2024) 222–232, https://doi.org/10.1007/s11307-023-01888-5.

[33] A. Dey, B. Charrier, K. Lemaitre, V. Ribay, D. Eshchenko, M. Schnell, R. Melzi, Q. Stern, S.F. Cousin, J.G. Kempf, S. Jannin, J.N. Dumez, P. Giraudeau, Fine optimization of a dissolution dynamic nuclear polarization experimental setting for ^{13}C NMR of metabolic samples, Magn. Reson. 3 (2022) 183–202, https://doi.org/10.5194/mr-3-183-2022.

[34] M. Stefanska, T. Muntener, S. Hiller, Photo-CIDNP for quantification of micromolar analytes in urine, Commun. Chem. 8 (2025) 223, https://doi.org/10.1038/s42004-025-01626-8.

[35] M. Otikovs, G.L. Olsen, E.R. Kupce, L. Frydman, Natural abundance, single-scan ^{13}C-^{13}C-based structural elucidations by dissolution DNP NMR, J. Am. Chem. Soc. 141 (2019) 1857–1861, https://doi.org/10.1021/jacs.8b12216.

[36] Y. Wang, J. Kim, C. Hilty, Determination of protein-ligand binding modes using fast multi-dimensional NMR with hyperpolarization, Chem. Sci. 11 (2020) 5935–5943, https://doi.org/10.1039/d0sc00266f.

[37] C. Lhoste, B. Lorandel, C. Praud, A. Marchand, R. Mishra, A. Dey, A. Bernard, J. N. Dumez, P. Giraudeau, Ultrafast 2D NMR for the analysis of complex mixtures, Prog. Nucl. Magn. Reson. Spectrosc. 130-131 (2022) 1–46, https://doi.org/10.1016/j.pnmrs.2022.01.002.

[38] B.O. Jimmink, M. Tessari, A.P.M. Kentgens, Hyphenation of 2D NMR with hydrogenative PHIP, Magn. Reson. Chem. 63 (2025) 278–282, https://doi.org/10.1002/mrc.5510.

[39] M. Reinhard, A. van der Ham, L. Yang, L. Broker, T. Orlando, I. Tkach, M. Levien, M. Bennati, Enhancing NMR signals in liquids by fluorine-19 Overhauser dynamic nuclear polarization (DNP) and hyperpolarization transfer to carbon-13, Angew. Chem. Int. Ed. 64 (2025) e202517498, https://doi.org/10.1002/anie.202517498.

[40] M. Levien, L. Yang, A. van der Ham, M. Reinhard, M. John, A. Purea, J. Ganz, T. Marquardsen, I. Tkach, T. Orlando, M. Bennati, Overhauser enhanced liquid state nuclear magnetic resonance spectroscopy in one and two dimensions, Nat. Commun. 15 (2024) 5904, https://doi.org/10.1038/s41467-024-50265-5.

[41] I. Solomon, Relaxation processes in a system of two spins, Phys. Rev. 99 (1955) 559–565, https://doi.org/10.1103/PhysRev.99.559.

[42] H.C. Dorn, J. Wang, L. Allen, D. Sweeney, T.E. Glass, Flow dynamic nuclear polarization, a novel method for enhancing NMR signals in flowing fluids, J. Magn. Reson. 79 (1988) 404–412, https://doi.org/10.1016/0022-2364(88)90078-9.

[43] N.M. Loening, M. Rosay, V. Weis, R.G. Griffin, Solution-state dynamic nuclear polarization at high magnetic field, J. Am. Chem. Soc. 124 (2002) 8808–8809, https://doi.org/10.1021/ja026660g.

[44] P. Höfer, G. Parigi, C. Luchinat, P. Carl, G. Guthausen, M. Reese, T. Carlomagno, C. Griesinger, M. Bennati, Field dependent dynamic nuclear polarization with radicals in aqueous solution, J. Am. Chem. Soc. 130 (2008) 3254–3255, https://doi.org/10.1021/ja0783207.

[45] M.J. Prandolini, V.P. Denysenkov, M. Gafurov, S. Lyubenova, B. Endeward, M. Bennati, T.F. Prisner, First DNP results from a liquid water-TEMPOL sample at 400 MHz and 260 GHz, Appl. Magn. Reson. 34 (2008) 399–407, https://doi.org/10.1007/s00723-008-0128-2.

[46] V. Denysenkov, M.J. Prandolini, M. Gafurov, D. Sezer, B. Endeward, T.F. Prisner, Liquid state DNP using a 260 GHz high power gyrotron, Phys. Chem. Chem. Phys. 12 (2010) 5786–5790, https://doi.org/10.1039/C003697h.

[47] M. Bennati, EPR interactions—Hyperfine couplings, in: D. Goldfarb, S. Stoll (Eds.), EPR Spectroscopy: Fundamentals and Methods, John Wiley & Sons, Chichester, UK, 2018.

[48] I. Solomon, N. Bloembergen, Nuclear magnetic interactions in the HF molecule, J. Chem. Phys. 25 (1956) 261–266, https://doi.org/10.1063/1.1742867.

[49] A. Abragam, R.V. Pound, Influence of electric and magnetic fields on angular correlations, Phys. Rev. 92 (1953) 943–962, https://doi.org/10.1103/PhysRev.92.943.

[50] M. Bennati, I. Tkach, M. Türke, Dynamic Nuclear Polarization in Liquids, in: Electron Paramagnetic Resonance, 2010, pp. 155–182.

[51] J.M. Franck, A. Pavlova, J.A. Scott, S. Han, Quantitative cw Overhauser effect dynamic nuclear polarization for the analysis of local water dynamics, Prog. Nucl. Magn. Reson. Spectrosc. 74 (2013) 33–56, https://doi.org/10.1016/j.pnmrs.2013.06.001.

[52] G.R. Eaton, S.S. Eaton, D.P. Barr, R.T. Weber, Quantitative EPR, Springer Vienna, 2010.

[53] M.H. Levitt, Spin Dynamics: Basics of Nuclear Magnetic Resonance, John Wiley & Sons, 2015.

[54] W. Müller-Warmuth, R. Vilhjalmsson, P.A.M. Gerlof, J. Smidt, J. Trommel, Intermolecular interactions of benzene and carbon tetrachloride with selected free radicals in solution as studied by ^{13}C and ^{1}H dynamic nuclear polarization, Mol. Phys. 31 (1976) 1055–1067, https://doi.org/10.1080/00268977600100811.

[55] X. Wang, W.C. Isley Iii, S.I. Salido, Z. Sun, L. Song, K.H. Tsai, C.J. Cramer, H. C. Dorn, Optimization and prediction of the electron-nuclear dipolar and scalar interaction in ^{1}H and ^{13}C liquid state dynamic nuclear polarization, Chem. Sci. 6 (2015) 6482–6495, https://doi.org/10.1039/c5sc02499d.

[56] J.H. Freed, Dynamic effects of pair correlation functions on spin relaxation by translational diffusion in liquids. II. Finite jumps and independent T_1 processes, J. Chem. Phys. 68 (1978) 4034–4037, https://doi.org/10.1063/1.436302.

[57] C.F. Polnaszek, R.G. Bryant, Nitroxide radical induced solvent proton relaxation: measurement of localized translational diffusion, J. Chem. Phys. 81 (1984) 4038–4045, https://doi.org/10.1063/1.448147.

[58] M. Bennati, C. Luchinat, G. Parigi, M.-T. Türke, Water ^{1}H relaxation dispersion analysis on a nitroxide radical provides information on the maximal signal enhancement in Overhauser dynamic nuclear polarization experiments, Phys. Chem. Chem. Phys. 12 (2010) 5902–5910, https://doi.org/10.1039/C002304N.

[59] D. Kruk, A. Korpala, E. Rossler, K.A. Earle, W. Medycki, J. Moscicki, 1H NMR relaxation in glycerol solutions of nitroxide radicals: effects of translational and rotational dynamics, J. Chem. Phys. 136 (2012) 114504, https://doi.org/10.1063/1.3692603.

[60] Y. Okuno, A. Szabo, G.M. Clore, Quantitative interpretation of solvent paramagnetic relaxation for probing protein-cosolute interactions, J. Am. Chem. Soc. 142 (2020) 8281–8290, https://doi.org/10.1021/jacs.0c00747.

[61] D. Sezer, Rationalizing Overhauser DNP of nitroxide radicals in water through MD simulations, Phys. Chem. Chem. Phys. 16 (2014) 1022–1032, https://doi.org/10.1039/c3cp53565g.

[62] M. Levien, M. Hiller, I. Tkach, M. Bennati, T. Orlando, Nitroxide derivatives for dynamic nuclear polarization in liquids: the role of rotational diffusion, J. Phys. Chem. Lett. 11 (2020) 1629–1635, https://doi.org/10.1021/acs.jpclett.0c00270.

[63] A.A. Kuzhelev, D. Dai, V. Denysenkov, I.A. Kirilyuk, E.G. Bagryanskaya, T. F. Prisner, Influence of rotational motion of nitroxides on overhauser dynamic nuclear polarization: a systematic study at high magnetic fields, J. Phys. Chem. C 125 (2021) 25651–25659, https://doi.org/10.1021/acs.jpcc.1c06979.

[64] T. Orlando, I. Kuprov, M. Hiller, Theoretical analysis of scalar relaxation in ^{13}C-DNP in liquids, J. Magn. Reson. Open 10-11 (2022) 100040, https://doi.org/10.1016/j.jmro.2022.100040.

[65] N. Enkin, G. Liu, M.d.C. Gimenez-Lopez, K. Porfyrakis, I. Tkach, M. Bennati, A high saturation factor in Overhauser DNP with nitroxide derivatives: the role of ^{14}N nuclear spin relaxation, Phys. Chem. Chem. Phys. 17 (2015) 11144–11149, https://doi.org/10.1039/C5CP00935A.

[66] B.B. Mascitti, G. Zanoni, A. van der Ham, L. Yang, L. Franco, F. Mancin, F. Rastrelli, T. Orlando, Nanoparticle-assisted dynamic nuclear polarization in liquids, Phys. Chem. Chem. Phys. 27 (2025) 22366–22374, https://doi.org/10.1039/d5cp02465j.

[67] W. Müller-Warmuth, R.v. Steenwinkel, F. Noack, Dynamic nuclear polarization experiments on ^{19}F in solutions and their interpretation by the "pulse model" of molecular collisions, Z. Naturforsch. A 23 (1968) 506–513, https://doi.org/10.1515/zna-1968-0408.

[68] F. Noack, G.J. Krüger, W. Müller-Warmuth, R. van Steenwinkel, Stochastische Prozesse in Spinsystemen, Z. Naturforsch. A 22 (1967) 2102–2108, https://doi.org/10.1515/zna-1967-1239.

[69] G. Liu, M. Levien, N. Karschin, G. Parigi, C. Luchinat, M. Bennati, One-thousand-fold enhancement of high field liquid nuclear magnetic resonance signals at room temperature, Nat. Chem. 9 (2017) 676–680, https://doi.org/10.1038/nchem.2723.

[70] D. Sezer, M. Gafurov, M.J. Prandolini, V.P. Denysenkov, T.F. Prisner, Dynamic nuclear polarization of water by a nitroxide radical: rigorous treatment of the electron spin saturation and comparison with experiments at 9.2 tesla, Phys. Chem. Chem. Phys. 11 (2009) 6638–6653, https://doi.org/10.1039/b906719c.

[71] D. Sezer, M.J. Prandolini, T.F. Prisner, Dynamic nuclear polarization coupling factors calculated from molecular dynamics simulations of a nitroxide radical in water, Phys. Chem. Chem. Phys. 11 (2009) 6626–6637, https://doi.org/10.1039/b905709a.

[72] D. Sezer, Computation of DNP coupling factors of a nitroxide radical in toluene: seamless combination of MD simulations and analytical calculations, Phys. Chem. Chem. Phys. 15 (2013) 526–540, https://doi.org/10.1039/c2cp42430d.

[73] S.E. Küçük, P. Neugebauer, T.F. Prisner, D. Sezer, Molecular simulations for dynamic nuclear polarization in liquids: a case study of TEMPOL in acetone and DMSO, Phys. Chem. Chem. Phys. 17 (2015) 6618–6628, https://doi.org/10.1039/c4cp05832a.

[74] S.E. Küçük, D. Sezer, Multiscale computational modeling of ^{13}C DNP in liquids, Phys. Chem. Chem. Phys. 18 (2016) 9353–9357, https://doi.org/10.1039/c6cp01028h.

[75] D. Dai, X. Wang, Y. Liu, X.-L. Yang, C. Glaubitz, V. Denysenkov, X. He, T. Prisner, J. Mao, Room-temperature dynamic nuclear polarization enhanced NMR spectroscopy of small biological molecules in water, Nat. Commun. 12 (2021) 6880, https://doi.org/10.1038/s41467-021-27067-0.

[76] R.K. Wangsness, F. Bloch, The dynamical theory of nuclear induction, Phys. Rev. 89 (1953) 728–739, https://doi.org/10.1103/PhysRev.89.728.

[77] A.G. Redfield, On the theory of relaxation processes, IBM J. Res. Dev. 1 (1957) 19–31, https://doi.org/10.1147/rd.11.0019.

[78] A.G. Palmer, Relaxation and dynamic processes, in: J. Cavanagh, W. J. Fairbrother, A.G. Palmer, M. Rance, N.J. Skelton (Eds.), Protein NMR Spectroscopy: Principles and Practice, Second edition, Academic Press, Burlington, 2007, pp. 333–404.

[79] I. Kuprov, Diagonalization-free implementation of spin relaxation theory for large spin systems, J. Magn. Reson. 209 (2011) 31–38, https://doi.org/10.1016/j.jmr.2010.12.004.

[80] I. Kuprov, Incomplete Basis Sets, in: Spin: From Basic Symmetries to Quantum Optimal Control, Springer, 2023, pp. 291–312.

[81] L.J. Edwards, D. Savostyanov, Z. Welderufael, D. Lee, I. Kuprov, Quantum mechanical NMR simulation algorithm for protein-size spin systems, J. Magn. Reson. 243 (2014) 107–113, https://doi.org/10.1016/j.jmr.2014.04.002.

[82] C.V. Loan, Computing integrals involving the matrix exponential, IEEE Trans Automat Contr 23 (1978) 395–404, https://doi.org/10.1109/TAC.1978.1101743.

[83] I. Najfeld, T.F. Havel, Derivatives of the matrix exponential and their computation, Adv. Appl. Math. 16 (1995) 321–375, https://doi.org/10.1006/aama.1995.1017.

[84] F. Carbonell, J. Jimenez, L. Pedroso, Computing multiple integrals involving matrix exponentials, J. Comput. Appl. Math. 213 (2008) 300–305, https://doi.org/10.1016/j.cam.2007.01.007.

[85] D.L. Goodwin, I. Kuprov, Auxiliary matrix formalism for interaction representation transformations, optimal control, and spin relaxation theories, J. Chem. Phys. 143 (2015) 084113, https://doi.org/10.1063/1.4928978.

[86] I. Kuprov, L.C. Morris, J.N. Glushka, J.H. Prestegard, Using molecular dynamics trajectories to predict nuclear spin relaxation behaviour in large spin systems, J. Magn. Reson. 323 (2021) 106891, https://doi.org/10.1016/j.jmr.2020.106891.

[87] D.P. Rangel, P.C. Baveye, B.H. Robinson, Direct simulation of magnetic resonance relaxation rates and line shapes from molecular trajectories, J. Phys. Chem. B 116 (2012) 6233–6249, https://doi.org/10.1021/jp2062628.

[88] H.J. Hogben, M. Krzystyniak, G.T.P. Charnock, P.J. Hore, I. Kuprov, *Spinach* – a software library for simulation of spin dynamics in large spin systems, J. Magn. Reson. 208 (2011) 179–194, https://doi.org/10.1016/j.jmr.2010.11.008.

[89] V. Briganti, A. Lunghi, A machine-learning framework for accelerating spin-lattice relaxation simulations, npj Comput. Mater 11 (2025) 62, https://doi.org/10.1038/s41524-025-01547-z.

[90] K. Pervushin, R. Riek, G. Wider, K. Wüthrich, Attenuated T_2 relaxation by mutual cancellation of dipole-dipole coupling and chemical shift anisotropy indicates an avenue to NMR structures of very large biological macromolecules in solution, Proc. Natl. Acad. Sci. U. S. A. 94 (1997) 12366–12371, https://doi.org/10.1073/pnas.94.23.12366.

[91] K. Pervushin, Impact of transverse relaxation optimized spectroscopy (TROSY) on NMR as a technique in structural biology, Q. Rev. Biophys. 33 (2000) 161–197, https://doi.org/10.1017/S0033583500003619.
[92] H.M. McConnell, Effect of anisotropic hyperfine interactions on paramagnetic relaxation in liquids, J. Chem. Phys. 25 (1956) 709–711, https://doi.org/10.1063/1.1743033.
[93] M.G. Concilio, M. Soundararajan, L. Frydman, I. Kuprov, High-field solution state DNP using cross-correlations, J. Magn. Reson. 326 (2021) 106940, https://doi.org/10.1016/j.jmr.2021.106940.
[94] G.W. Reginsson, N.C. Kunjir, S.T. Sigurdsson, O. Schiemann, Trityl radicals: spin labels for nanometer-distance measurements, Chem. A Eur. J. 18 (2012) 13580, https://doi.org/10.1002/chem.201203014.
[95] J.J. Jassoy, A. Meyer, S. Spicher, C. Wuebben, O. Schiemann, Synthesis of nanometer sized bis- and tris-trityl model compounds with different extent of spin-spin coupling, Molecules 23 (2018) 682, https://doi.org/10.3390/molecules23030682.
[96] I. Kuprov, Bestiary of spin Hamiltonians, in: Spin: From Basic Symmetries to Quantum Optimal Control, Springer, 2023, pp. 73–105.
[97] M.G. Concilio, I. Kuprov, L. Frydman, *J*-driven dynamic nuclear polarization for sensitizing high field solution state NMR, Phys. Chem. Chem. Phys. 24 (2022) 2118–2125, https://doi.org/10.1039/D1CP04186J.
[98] M.G. Concilio, L. Frydman, Microwave-free *J*-driven dynamic nuclear polarization: a proposal for enhancing the sensitivity of solution-state NMR, Phys. Rev. E 107 (2023) 035303, https://doi.org/10.1103/PhysRevE.107.035303.
[99] M. Grazia Concilio, L. Frydman, Steady state effects introduced by local relaxation modes on *J*-driven DNP-enhanced NMR, J. Magn. Reson. 355 (2023) 107542, https://doi.org/10.1016/j.jmr.2023.107542.
[100] M.G. Concilio, Y. Wang, L. Wang, X. Kong, Triplet *J*-driven DNP — a proposal to increase the sensitivity of solution-state NMR without microwaves, J. Phys. Chem. A 129 (2025) 3886–3897, https://doi.org/10.1021/acs.jpca.5c02079.
[101] I. Kuprov, Dissipative Spin Dynamics, in: Spin: From Basic Symmetries to Quantum Optimal Control, Springer, 2023, pp. 223–289.
[102] I. Kuprov, N. Wagner-Rundell, P.J. Hore, Bloch-Redfield-Wangsness theory engine implementation using symbolic processing software, J. Magn. Reson. 184 (2007) 196–206, https://doi.org/10.1016/j.jmr.2006.09.023.
[103] A.A. Kuzhelev, D. Dai, V. Denysenkov, T.F. Prisner, Solid-like dynamic nuclear polarization observed in the fluid phase of lipid bilayers at 9.4 T, J. Am. Chem. Soc. 144 (2022) 1164–1168, https://doi.org/10.1021/jacs.1c12837.
[104] A.A. Kuzhelev, V. Denysenkov, I.M. Ahmad, O.Y. Rogozhnikova, D.V. Trukhin, E. G. Bagryanskaya, V.M. Tormyshev, S.T. Sigurdsson, T.F. Prisner, Solid-effect dynamic nuclear polarization in viscous liquids at 9.4 T using narrow-line polarizing agents, J. Am. Chem. Soc. 145 (2023) 10268–10274, https://doi.org/10.1021/jacs.3c01358.
[105] D. Dai, V. Denysenkov, E.G. Bagryanskaya, V.M. Tormyshev, T.F. Prisner, A. A. Kuzhelev, ^{13}C hyperpolarization of viscous liquids by transfer of solid-effect ^{1}H dynamic nuclear polarization at high magnetic field, J. Phys. Chem. Lett. 14 (2023) 7059–7064, https://doi.org/10.1021/acs.jpclett.3c01732.
[106] D. Sezer, The solid effect of dynamic nuclear polarization in liquids, Magn. Reson. 4 (2023) 153–174, https://doi.org/10.5194/mr-4-153-2023.
[107] A. Kuzhelev, ^{31}P dynamic nuclear polarization through the solid effect: study of biomolecules in aqueous solutions at 9.4 T, Anal. Chem. 97 (2025) 14890–14893, https://doi.org/10.1021/acs.analchem.5c02158.
[108] D. Sezer, D. Dai, T.F. Prisner, The solid effect of dynamic nuclear polarization in liquids - accounting for g-tensor anisotropy at high magnetic fields, Magn. Reson. 4 (2023) 243–269, https://doi.org/10.5194/mr-4-243-2023.
[109] O. Jakdetchai, V. Denysenkov, J. Becker-Baldus, B. Dutagaci, T.F. Prisner, C. Glaubitz, Dynamic nuclear polarization-enhanced NMR on aligned lipid bilayers at ambient temperature, J. Am. Chem. Soc. 136 (2014) 15533–15536, https://doi.org/10.1021/ja509799s.
[110] S.-T. Han, R.G. Griffin, K.-N. Hu, C.-G. Joo, C.D. Joye, I. Mastovsky, M.A. Shapiro, J.R. Sirigiri, R.J. Temkin, A.C. Torrezan, Continuous-wave submillimeter-wave gyrotrons, in: Terahertz Physics, Devices, and Systems, SPIE (2006) 41–48.
[111] M.Y. Glyavin, A.V. Chirkov, G.G. Denisov, A.P. Fokin, V.V. Kholoptsev, A. N. Kuftin, A.G. Luchinin, G.Y. Golubyatnikov, V.I. Malygin, M.V. Morozkin, V. N. Manuilov, M.D. Proyavin, A.S. Sedov, E.V. Sokolov, E.M. Tai, A.I. Tsvetkov, V. E. Zapevalov, Experimental tests of a 263 GHz gyrotron for spectroscopic applications and diagnostics of various media, Rev. Sci. Instrum. 86 (2015) 054705, https://doi.org/10.1063/1.4921322.
[112] A. Fokin, M. Glyavin, G. Golubiatnikov, L. Lubyako, M. Morozkin, B. Movschevich, A. Tsvetkov, G. Denisov, High-power sub-terahertz source with a record frequency stability at up to 1 Hz, Sci. Rep. 8 (2018) 4317, https://doi.org/10.1038/s41598-018-22772-1.
[113] K. Herb, R. Tschaggelar, G. Denninger, G. Jeschke, Double resonance calibration of g factor standards: carbon fibers as a high precision standard, J. Magn. Reson. 289 (2018) 100–106, https://doi.org/10.1016/j.jmr.2018.02.006.
[114] T. Orlando, R. Dervişoğlu, M. Levien, I. Tkach, T.F. Prisner, L.B. Andreas, V. P. Denysenkov, M. Bennati, Dynamic nuclear polarization of C-13 nuclei in the liquid state over a 10 tesla field range, Angew. Chem. Int. Ed. 58 (2019) 1402–1406, https://doi.org/10.1002/anie.201811892.
[115] V.P. Denysenkov, M.J. Prandolini, A. Krahn, M. Gafurov, B. Endeward, T. F. Prisner, High-field DNP spectrometer for liquids, Appl. Magn. Reson. 34 (2008) 289–299, https://doi.org/10.1007/s00723-008-0127-3.
[116] M.J. Prandolini, V.P. Denysenkov, M. Gafurov, B. Endeward, T.F. Prisner, High-field dynamic nuclear polarization in aqueous solutions, J. Am. Chem. Soc. 131 (2009) 6090–6092, https://doi.org/10.1021/ja901496g.
[117] T. Orlando, H. Bui, J. Cabigting, N. Ibbetson, J. van Tol, T. Dubroca, X. Wang, F. Mentink-Vigier, Impact of non-polar solvents in dynamic nuclear polarization at high magnetic fields, J. Magn. Reson. 375 (2025) 107885, https://doi.org/10.1016/j.jmr.2025.107885.
[118] C. George, N. Chandrakumar, Chemical-shift-resolved ^{19}F NMR spectroscopy between 13.5 and 135 MHz: Overhauser-DNP-enhanced diagonal suppressed correlation spectroscopy, Angew. Chem. Int. Ed. 53 (2014) 8441–8444, https://doi.org/10.1002/anie.201402320.
[119] J. Gendell, J.H. Freed, G.K. Fraenkel, Solvent effects in electron spin resonance spectra, J. Chem. Phys. 37 (1962) 2832–2841, https://doi.org/10.1063/1.1733110.
[120] M.C.R. Symons, A.S. Pena-Nuñez, Solvation of nitroxides, J. Chem. Soc. Faraday Trans. 1 (81) (1985) 2421–2435, https://doi.org/10.1039/f19858102421.
[121] B.R. Knauer, J.J. Napier, The nitrogen hyperfine splitting constant of the nitroxide functional group as a solvent polarity parameter. The relative importance for a solvent polarity parameter of its being a cybotactic probe vs. its being a model process, J. Am. Chem. Soc. 98 (1976) 4395–4400, https://doi.org/10.1021/ja00431a010.
[122] P. Franchi, M. Lucarini, P. Pedrielli, G.F. Pedulli, Nitroxide radicals as hydrogen bonding acceptors. An infrared and EPR study, ChemPhysChem 3 (2002) 789–793, https://doi.org/10.1002/1439-7641(20020916)3:9<789::AID-CPHC789>3.0.CO;2-Z.
[123] X. Pang, W.J. Jin, Exploring the halogen bond specific solvent effects in halogenated solvent systems by ESR probe, New J. Chem. 39 (2015) 5477–5483, https://doi.org/10.1039/c5nj00300h.
[124] V. Weis, M. Bennati, M. Rosay, J.A. Bryant, R.G. Griffin, High-field DNP and ENDOR with a novel multiple-frequency resonance structure, J. Magn. Reson. 140 (1999) 293–299, https://doi.org/10.1006/jmre.1999.1841.
[125] F. Bloch, Nuclear induction, Phys. Rev. 70 (1946) 460–474, https://doi.org/10.1103/PhysRev.70.460.
[126] J.J. Yin, M. Pasenkiewicz-Gierula, J.S. Hyde, Lateral diffusion of lipids in membranes by pulse saturation recovery electron spin resonance, Proc. Natl. Acad. Sci. U. S. A. 84 (1987) 964–968, https://doi.org/10.1073/pnas.84.4.964.
[127] M.T. Türke, M. Bennati, Saturation factor of nitroxide radicals in liquid DNP by pulsed ELDOR experiments, Phys. Chem. Chem. Phys. 13 (2011) 3630–3633, https://doi.org/10.1039/c0cp02126a.
[128] M.T. Türke, G. Parigi, C. Luchinat, M. Bennati, Overhauser DNP with ^{15}N labelled Fremy's salt at 0.35 tesla, Phys. Chem. Chem. Phys. 14 (2012) 502–510, https://doi.org/10.1039/c1cp22332a.
[129] J.S. Hyde, J.C.W. Chien, J.H. Freed, Electron–electron double resonance of free radicals in solution, J. Chem. Phys. 48 (1968) 4211–4226, https://doi.org/10.1063/1.1669760.
[130] N. Enkin, G. Liu, I. Tkach, M. Bennati, High DNP efficiency of TEMPONE radicals in liquid toluene at low concentrations, Phys. Chem. Chem. Phys. 16 (2014) 8795–8800, https://doi.org/10.1039/C4CP00854E.
[131] M. Reinhard, M. Levien, M. Bennati, T. Orlando, Large ^{31}P-NMR enhancements in liquid state dynamic nuclear polarization through radical/target molecule non-covalent interaction, Phys. Chem. Chem. Phys. 25 (2023) 822–828, https://doi.org/10.1039/d2cp04092a.
[132] C.P. Poole, Electron Spin Resonance: A Comprehensive Treatise on Experimental Techniques, 2nd ed., John Wiley & Sons Inc, 1983.
[133] M.T. Türke, I. Tkach, M. Reese, P. Höfer, M. Bennati, Optimization of dynamic nuclear polarization experiments in aqueous solution at 15 MHz/9.7 GHz: a comparative study with DNP at 140 MHz/94 GHz, Phys. Chem. Chem. Phys. 12 (2010) 5893–5901, https://doi.org/10.1039/C002814M.
[134] T. Dubroca, S. Wi, J. van Tol, L. Frydman, S. Hill, Large volume liquid state scalar Overhauser dynamic nuclear polarization at high magnetic field, Phys. Chem. Chem. Phys. 21 (2019) 21200–21204, https://doi.org/10.1039/c9cp02997d.
[135] V. Denysenkov, T. Prisner, Liquid state dynamic nuclear polarization probe with Fabry-Pérot resonator at 9.2 T, J. Magn. Reson. 217 (2012) 1–5, https://doi.org/10.1016/j.jmr.2012.01.014.
[136] V. Denysenkov, D. Dai, T.F. Prisner, A triple resonance (e, ^{1}H, ^{13}C) probehead for liquid-state DNP experiments at 9.4 tesla, J. Magn. Reson. 337 (2022) 107185, https://doi.org/10.1016/j.jmr.2022.107185.
[137] T. Dubroca, A.N. Smith, K.J. Pike, S. Froud, R. Wylde, B. Trociewitz, J. McKay, F. Mentink-Vigier, J. van Tol, S. Wi, W. Brey, J.R. Long, L. Frydman, S. Hill, A quasi-optical and corrugated waveguide microwave transmission system for simultaneous dynamic nuclear polarization NMR on two separate 14.1 T spectrometers, J. Magn. Reson. 289 (2018) 35–44, https://doi.org/10.1016/j.jmr.2018.01.015.
[138] D. Yoon, A.I. Dimitriadis, M. Soundararajan, C. Caspers, J. Genoud, S. Alberti, E. de Rijk, J.-P. Ansermet, High-field liquid-state dynamic nuclear polarization in microliter samples, Anal. Chem. 90 (2018) 5620–5626, https://doi.org/10.1021/acs.analchem.7b04700.
[139] M. Gafurov, V. Denysenkov, M.J. Prandolini, T.F. Prisner, Temperature dependence of the proton overhauser DNP enhancements on aqueous solutions of Fremy's salt measured in a magnetic field of 9.2 T, Appl. Magn. Reson. 43 (2012) 119–128, https://doi.org/10.1007/s00723-012-0352-7.
[140] J.R. Biller, V.M. Meyer, H. Elajaili, G.M. Rosen, S.S. Eaton, G.R. Eaton, Frequency dependence of electron spin relaxation times in aqueous solution for a nitronyl nitroxide radical and perdeuterated-tempone between 250 MHz and 34 GHz, J. Magn. Reson. 225 (2012) 52–57, https://doi.org/10.1016/j.jmr.2012.10.002.
[141] J.R. Biller, H. Elajaili, V. Meyer, G.M. Rosen, S.S. Eaton, G.R. Eaton, Electron spin–lattice relaxation mechanisms of rapidly-tumbling nitroxide radicals, J. Magn. Reson. 236 (2013) 47–56, https://doi.org/10.1016/j.jmr.2013.08.006.

[142] S.S. Eaton, G.R. Eaton, Relaxation mechanisms, eMagRes (2016) 1543–1556, https://doi.org/10.1002/9780470034590.emrstm1507.

[143] B.H. Robinson, D.A. Haas, C. Mailer, Molecular dynamics in liquids: spin-lattice relaxation of nitroxide spin labels, Science 263 (1994) 490–493, https://doi.org/10.1126/science.8290958.

[144] W. Froncisz, T.G. Camenisch, J.J. Ratke, J.R. Anderson, W.K. Subczynski, R. A. Strangeway, J.W. Sidabras, J.S. Hyde, Saturation recovery EPR and ELDOR at W-band for spin labels, J. Magn. Reson. 193 (2008) 297–304, https://doi.org/10.1016/j.jmr.2008.05.008.

[145] N. Wili, A.B. Nielsen, L.A. Völker, L. Schreder, N.C. Nielsen, G. Jeschke, K.O. Tan, Designing broadband pulsed dynamic nuclear polarization sequences in static solids, Sci. Adv. 8 (2022) eabq0536, https://doi.org/10.1126/sciadv.abq0536.

[146] V.S. Redrouthu, G. Mathies, Efficient pulsed dynamic nuclear polarization with the X-inverse-X sequence, J. Am. Chem. Soc. 144 (2022) 1513–1516, https://doi.org/10.1021/jacs.1c09900.

[147] M. Alecci, D.J. Lurie, Low field (10 mT) pulsed dynamic nuclear polarization, J. Magn. Reson. 138 (1999) 313–319, https://doi.org/10.1006/jmre.1999.1721.

[148] E.A. Nasibulov, K.L. Ivanov, R.Z. Sagdeev, Theoretical treatment of pulsed dnp experiments: effects of spectral exchange, Appl. Magn. Reson. 50 (2019) 1233–1240, https://doi.org/10.1007/s00723-019-01144-6.

[149] E.A. Nasibulov, K.L. Ivanov, A.V. Yurkovskaya, H.M. Vieth, Theory of the Overhauser effect in the pulsed mode of EPR pumping: exploiting the advantages of coherent electron spin motion, Phys. Chem. Chem. Phys. 14 (2012) 6459–6468, https://doi.org/10.1039/c2cp23896a.

[150] P. Schöps, P.E. Spindler, T.F. Prisner, Multi-frequency pulsed Overhauser DNP at 1.2 tesla, Z. Phys. Chem. 231 (2017) 561–573, https://doi.org/10.1515/zpch-2016-0844.

[151] R.A. Wind, H. Lock, M. Mehring, ^{13}C knight shift saturation and ^{1}H dynamic nuclear polarization in a polycrystalline sample of the organic conductor (fluoranthenyl)$_2PF_6$, Chem. Phys. Lett. 141 (1987) 283–288, https://doi.org/10.1016/0009-2614(87)85024-8.

[152] P. Neugebauer, J.G. Krummenacker, V.P. Denysenkov, G. Parigi, C. Luchinat, T. F. Prisner, Liquid state DNP of water at 9.2 T: an experimental access to saturation, Phys. Chem. Chem. Phys. 15 (2013) 6049–6056, https://doi.org/10.1039/c3cp44461a.

[153] J.D. Jackson, Classical Electrodynamics, John Wiley & Sons, 2021.

[154] F.J. Scott, T. Dubroca, R.W. Schurko, S. Hill, J.R. Long, F. Mentink-Vigier, Characterization of dielectric properties and their impact on MAS-DNP NMR applications, J. Magn. Reson. 365 (2024) 107742, https://doi.org/10.1016/j.jmr.2024.107742.

[155] H.J. Liebe, G.A. Hufford, T. Manabe, A model for the complex permittivity of water at frequencies below 1 THz, Int. J. Infrared Millim. Waves 12 (1991) 659–675, https://doi.org/10.1007/BF01008897.

[156] N.Y. Tan, R. Li, P. Brauer, C. D'Agostino, L.F. Gladden, J.A. Zeitler, Probing hydrogen-bonding in binary liquid mixtures with terahertz time-domain spectroscopy: a comparison of Debye and absorption analysis, Phys. Chem. Chem. Phys. 17 (2015) 5999–6008, https://doi.org/10.1039/C4CP04477K.

[157] T. Maly, T.J. Keller, Instrumentation for high-field dynamic nuclear polarization and electron paramagnetic resonance spectroscopy, Eur. Phys. J. A 61 (2025), https://doi.org/10.1140/epja/s10050-025-01483-y.

[158] I.V. Sergeyev, F. Aussenac, A. Purea, C. Reiter, E. Bryerton, S. Retzloff, J. Hesler, L. Tometich, M. Rosay, Efficient 263 GHz magic angle spinning DNP at 100 K using solid-state diode sources, Solid State Nucl. Magn. Reson. 100 (2019) 63–69, https://doi.org/10.1016/j.ssnmr.2019.03.008.

[159] K.A. Earle, D.S. Tipikin, J.H. Freed, Far-infrared electron-paramagnetic-resonance spectrometer utilizing a quasioptical reflection bridge, Rev. Sci. Instrum. 67 (1996) 2502–2513, https://doi.org/10.1063/1.1147205.

[160] E.J. Reijerse, P.J. van Dam, A.A.K. Klaassen, W.R. Hagen, P.J.M. van Bentum, G. M. Smith, Concepts in high-frequency EPR — applications to bio-inorganic systems, Appl. Magn. Reson. 14 (1998) 153–167, https://doi.org/10.1007/bf03161887.

[161] Y. Quan, M.V.H. Subramanya, Y. Ouyang, M. Mardini, T. Dubroca, S. Hill, R. G. Griffin, Coherent dynamic nuclear polarization using chirped pulses, J. Phys. Chem. Lett. 14 (2023) 4748–4753, https://doi.org/10.1021/acs.jpclett.3c00726.

[162] M. Mardini, R.S. Palani, I.M. Ahmad, S. Mandal, S.K. Jawla, E. Bryerton, R. J. Temkin, S.T. Sigurdsson, R.G. Griffin, Frequency-swept dynamic nuclear polarization, J. Magn. Reson. 353 (2023) 107511, https://doi.org/10.1016/j.jmr.2023.107511.

[163] T.F. Kemp, H.R. Dannatt, N.S. Barrow, A. Watts, S.P. Brown, M.E. Newton, R. Dupree, Dynamic nuclear polarization enhanced NMR at 187 GHz/284 MHz using an extended interaction klystron amplifier, J. Magn. Reson. 265 (2016) 77–82, https://doi.org/10.1016/j.jmr.2016.01.021.

[164] A.A. Nevzorov, S. Milikisiyants, A. Marek, I. Kaminker, A.I. Smirnov, Room-temperature pulsed dynamic nuclear polarization at 7 T, J. Phys. Chem. Lett. 16 (2025) 5321–5326, https://doi.org/10.1021/acs.jpclett.5c00737.

[165] Z. Zhang, Y. Jiang, H. Pi, H. Chen, C. Liu, J. Feng, M. Liu, THz-enhanced dynamic nuclear polarized liquid spectrometer, J. Magn. Reson. 330 (2021) 107044, https://doi.org/10.1016/j.jmr.2021.107044.

[166] M. Rosay, M. Blank, F. Engelke, Instrumentation for solid-state dynamic nuclear polarization with magic angle spinning NMR, J. Magn. Reson. 264 (2016) 88–98, https://doi.org/10.1016/j.jmr.2015.12.026.

[167] D. Yoon, M. Soundararajan, P. Cuanillon, F. Braunmueller, S. Alberti, J. P. Ansermet, Dynamic nuclear polarization by frequency modulation of a tunable gyrotron of 260 GHz, J. Magn. Reson. 262 (2016) 62–67, https://doi.org/10.1016/j.jmr.2015.11.008.

[168] B. Corzilius, High-field dynamic nuclear polarization, Annu. Rev. Phys. Chem. 71 (2020) 143–170, https://doi.org/10.1146/annurev-physchem-071119-040222.

[169] S. Jawla, Q.Z. Ni, A. Barnes, W. Guss, E. Daviso, J. Herzfeld, R. Griffin, R. Temkin, Continuously tunable 250 GHz gyrotron with a double disk window for DNP-NMR spectroscopy, J. Infrared Millim. Terahertz Waves 34 (2013) 42–52, https://doi.org/10.1007/s10762-012-9947-1.

[170] T. Prisner, V. Denysenkov, Double-resonance structure and method for investigating samples by DNP and/or ENDOR, in US8570033B2 (2013).

[171] H. Kogelnik, T. Li, Laser beams and resonators, Appl. Optics 5 (1966) 1550–1567, https://doi.org/10.1364/AO.5.001550.

[172] S. Milikisiyants, A.A. Nevzorov, A.I. Smirnov, Photonic band-gap resonators for high-field/high-frequency EPR of microliter-volume liquid aqueous samples, J. Magn. Reson. 296 (2018) 152–164, https://doi.org/10.1016/j.jmr.2018.09.006.

[173] A.A. Nevzorov, S. Milikisiyants, A.N. Marek, A.I. Smirnov, Multi-resonant photonic band-gap/saddle coil DNP probehead for static solid state NMR of microliter volume samples, J. Magn. Reson. 297 (2018) 113–123, https://doi.org/10.1016/j.jmr.2018.10.010.

[174] A.A. Nevzorov, A. Marek, S. Milikisiyants, A.I. Smirnov, Characterization of photonic band resonators for DNP NMR of thin film samples at 7 T magnetic field, J. Magn. Reson. 323 (2021) 106893, https://doi.org/10.1016/j.jmr.2020.106893.

[175] A.A. Nevzorov, A. Marek, S. Milikisiyants, A.I. Smirnov, High-frequency, high-power DNP/EPR spectrometer operating at 7 T magnetic field, J. Magn. Reson. 362 (2024) 107677, https://doi.org/10.1016/j.jmr.2024.107677.

[176] G. Annino, A. Macor, E. De Rijk, S. Alberti, Magnetic resonance hyperpolarization probe head, in: WO2013000508A1, 2013.

[177] G. Annino, A. Macor, E. De Rijk, S. Alberti, Magnetic resonance hyperpolarization and multiple irradiation probe head, in US9448290B2 (2016).

[178] M. Soundararajan, T. Dubroca, J. van Tol, S. Hill, L. Frydman, S. Wi, Proton-detected solution-state NMR at 14.1 T based on scalar-driven ^{13}C Overhauser dynamic nuclear polarization, J. Magn. Reson. 343 (2022) 107304, https://doi.org/10.1016/j.jmr.2022.107304.

[179] G.M. Smith, J.C.G. Lesurf, R.H. Mitchell, P.C. Riedi, Quasi-optical CW mm-wave electron spin resonance spectrometer, Rev. Sci. Instrum. 69 (1998) 3924–3937, https://doi.org/10.1063/1.1149200.

[180] K.R. Thurber, W.M. Yau, R. Tycko, Low-temperature dynamic nuclear polarization at 9.4 T with a 30 mW microwave source, J. Magn. Reson. 204 (2010) 303–313, https://doi.org/10.1016/j.jmr.2010.03.016.

[181] Y. Rao, A. Venkatesh, P. Moutzouri, L. Emsley, ^{1}H hyperpolarization of solutions by Overhauser dynamic nuclear polarization with ^{13}C-^{1}H polarization transfer, J. Phys. Chem. Lett. 13 (2022) 7749–7755, https://doi.org/10.1021/acs.jpclett.2c01956.

[182] Y. Rao, F. De Biasi, R. Wei, C. Copéret, L. Emsley, Probing homogeneous catalysts and precatalysts in solution by exchange-mediated Overhauser dynamic nuclear polarization NMR, J. Am. Chem. Soc. 146 (2024) 12587–12594, https://doi.org/10.1021/jacs.4c01570.

[183] Y. Rao, D. Gioffre, M. Levien, M. Worle, P. Pandey, M. Mazzanti, C. Coperet, L. Emsley, Surface enhanced nuclear magnetic resonance spectroscopy at solid-liquid interfaces using Overhauser dynamic nuclear polarization, J. Am. Chem. Soc. 147 (2025) 21297–21301, https://doi.org/10.1021/jacs.5c04452.

[184] T. Marquardsen, M. Bennati, I. Tkach, M. Levien, T. Orlando, L. Yang, A. Leavesly, R. Wylde, DNP probe head for high resolution, liquid-state nmr, in: WO2024115698A1, 2023.

[185] J.L. Russ, J. Gu, K.H. Tsai, T. Glass, J.C. Duchamp, H.C. Dorn, Nitroxide/substrate weak hydrogen bonding: attitude and dynamics of collisions in solution, J. Am. Chem. Soc. 129 (2007) 7018–7027, https://doi.org/10.1021/ja064632i.

[186] W. Müller-Warmuth, R. Vilhjalmsson, Dynamische Kernpolarisation und zwischenmolekulare Wechselwirkungen in phosphor-und thalliumorganischen Lösungen, Z. Phys. Chem. 93 (1974) 283–298, https://doi.org/10.1524/zpch.1974.93.1-6.283.

[187] Y. He, Z. Zhang, J. Feng, C. Huang, F. Chen, C. Liu, M. Liu, Simultaneous acquisition of multi-nuclei enhanced NMR/MRI by solution-state dynamic nuclear polarization, Sci. China Chem. 59 (2016) 830–835, https://doi.org/10.1007/s11426-015-0512-0.

[188] K.H. Tsai, T.E. Glass, H.C. Dorn, Dipolar-dominated ^{29}Si dynamic nuclear polarization overhauser enhancements for hexamethyldisiloxane, J. Magn. Reson. 89 (1990) 362–366, https://doi.org/10.1016/0022-2364(90)90240-a.

[189] R.D. Bates, E.H. Poindexter, B.E. Wagner, Dynamic nuclear polarization studies of intermolecular coupling of deuteron and unpaired electron spins, J. Chem. Phys. 59 (1973) 3031–3037, https://doi.org/10.1063/1.1680440.

[190] J.A. Potenza, J.W. Linowski, Dynamic polarization of ^{7}Li nuclei in solution, J. Chem. Phys. 54 (1971) 4095–4099, https://doi.org/10.1063/1.1675472.

[191] J.A. Potenza, J.W. Linowski, E.H. Poindexter, B.E. Wagner, R.D. Bates, Dynamic polarization of ^{7}Li nuclei in solutions containing radical ions, Mol. Phys. 29 (1975) 1597–1610, https://doi.org/10.1080/00268977500101401.

[192] B.E. Wagner, J.W. Linowski, J.A. Potenza, R.D. Bates, J.N. Helbert, E. H. Poindexter, Dynamic nuclear polarization studies of labile complex formation between lithium ion and nitronyl nitroxide or imidazoline-1-oxyl radical ligands, J. Am. Chem. Soc. 98 (1976) 4405–4409, https://doi.org/10.1021/ja00431a012.

[193] R. Vilhjalmsson, J. Köppen, Dynamic nuclear polarization of tin-119 nuclei in free radical solutions, Chem. Phys. Lett. 50 (1977) 442–444, https://doi.org/10.1016/0009-2614(77)80362-X.

[194] T. Harris, O. Szekely, L. Frydman, On the potential of hyperpolarized water in biomolecular NMR studies, J. Phys. Chem. B 118 (2014) 3281–3290, https://doi.org/10.1021/jp4102916.

[195] G. Angelovski, B.J. Tickner, G. Wang, Opportunities and challenges with hyperpolarized bioresponsive probes for functional imaging using magnetic resonance, Nat. Chem. 15 (2023) 755–763, https://doi.org/10.1038/s41557-023-01211-3.

[196] M. Butikofer, G.R. Stadler, H. Kadavath, R. Cadalbert, F. Torres, R. Riek, Rapid protein-ligand affinity determination by photoinduced hyperpolarized NMR, J. Am. Chem. Soc. 146 (2024) 17974–17985, https://doi.org/10.1021/jacs.4c04000.

[197] K.H. Tsai, H.C. Dorn, A model for establishing the ultimate enhancements (a_∞) in the low to high magnetic field transfer dynamic nuclear polarization experiment, Appl. Magn. Reson. 1 (1990) 231–254, https://doi.org/10.1007/bf03166157.

[198] L. Yang, T. Orlando, M. Bennati, Halogen-bond-mediated ^{13}C Overhauser dynamic nuclear polarization at 9.4 T, J. Phys. Chem. Lett. 16 (2025) 4505–4514, https://doi.org/10.1021/acs.jpclett.5c00798.

[199] M. Levien, M. Reinhard, M. Hiller, I. Tkach, M. Bennati, T. Orlando, Spin density localization and accessibility of organic radicals affect liquid-state DNP efficiency, Phys. Chem. Chem. Phys. 23 (2021) 4480–4485, https://doi.org/10.1039/d0cp05796g.

[200] R.D. Green, Hydrogen Bonding by C—H Groups, 1 ed., Red Globe Press, London, 1974.

[201] R.D. Bates, B.E. Wagner, E.H. Poindexter, Transient intermolecular spin coupling of trichloromethane with di-tert-butyl nitroxide free radical, J. Phys. Chem. 81 (1977) 276–279, https://doi.org/10.1021/j100518a018.

[202] G. Cavallo, P. Metrangolo, R. Milani, T. Pilati, A. Priimagi, G. Resnati, G. Terraneo, The halogen bond, Chem. Rev. 116 (2016) 2478–2601, https://doi.org/10.1021/acs.chemrev.5b00484.

[203] M. Witwicki, P.K. Walencik, J. Jezierska, How accurate is density functional theory in predicting spin density? An insight from the prediction of hyperfine coupling constants, J. Mol. Model. 26 (2019) 10, https://doi.org/10.1007/s00894-019-4268-0.

[204] Z.W. Windom, A. Perera, R.J. Bartlett, Benchmarking isotropic hyperfine coupling constants using (QTP) DFT functionals and coupled cluster theory, J. Chem. Phys. 156 (2022) 092107, https://doi.org/10.1063/5.0069928.

[205] M. Saitow, F. Neese, Accurate spin-densities based on the domain-based local pair-natural orbital coupled-cluster theory, J. Chem. Phys. 149 (2018) 034104, https://doi.org/10.1063/1.5027114.

[206] A.A. Auer, V.A. Tran, B. Sharma, G.L. Stoychev, D. Marx, F. Neese, A case study of density functional theory and domain-based local pair natural orbital coupled cluster for vibrational effects on EPR hyperfine coupling constants: vibrational perturbation theory versus ab initio molecular dynamics, Mol. Phys. 118 (2020) e1797916, https://doi.org/10.1080/00268976.2020.1797916.

[207] P. Dzien, A. Fages, G. Jona, K.M. Brindle, M. Schwaiger, L. Frydman, Following metabolism in living microorganisms by hyperpolarized ^{1}H NMR, J. Am. Chem. Soc. 138 (2016) 12278–12286, https://doi.org/10.1021/jacs.6b07483.

[208] A.J. Simpson, M.J. Simpson, R. Soong, Environmental nuclear magnetic resonance spectroscopy: an overview and a primer, Anal. Chem. 90 (2018) 628–639, https://doi.org/10.1021/acs.analchem.7b03241.

[209] K. Ronda, J. Gauthier, K. Singaravadivel, P.M. Costa, K. Downey, W.W. Wolff, D. H. Lysak, J. Pellizzari, O.V. Meulen, K. Steiner, A. Jenne, M. Bastawrous, Z. Ng, A. Haber, B. Goerling, V. Busse, F. Busse, C. Elliot, S. Mabury, M. Ateia, D.C. G. Muir, R.J. Letcher, K. Krishnamurthy, S. Kleywegt, K.J. Jobst, M.J. Simpson, A. J. Simpson, NMR as a discovery tool: exploration of industrial effluents discharged into the environment, Magn. Reson. Chem. 63 (2025) 453–475, https://doi.org/10.1002/mrc.5527.

[210] G. Zhang, F. Schilling, S.J. Glaser, C. Hilty, Reaction monitoring using hyperpolarized NMR with scaling of heteronuclear couplings by optimal tracking, J. Magn. Reson. 272 (2016) 123–128, https://doi.org/10.1016/j.jmr.2016.09.006.

[211] O. Semenova, P.M. Richardson, A.J. Parrott, A. Nordon, M.E. Halse, S.B. Duckett, Reaction monitoring using SABRE-hyperpolarized benchtop (1 T) NMR spectroscopy, Anal. Chem. 91 (2019) 6695–6701, https://doi.org/10.1021/acs.analchem.9b00729.

[212] J.N. Helbert, E.H. Poindexter, B.E. Wagner, Scalar dynamic nuclear polarization of protons in trifluoroacetic acid solutions, Chem. Phys. Lett. 52 (1977) 546–548, https://doi.org/10.1016/0009-2614(77)80506-x.

[213] J. Milani, F. Saenz, C. Roussel, J.P. Ansermet, Heterogeneous Overhauser-DNP on ^{1}H dominated by scalar coupling in aqueous solution, Magn. Reson. Chem. 61 (2023) 180–183, https://doi.org/10.1002/mrc.5321.

[214] R.A. Dwek, R.E. Richards, D. Taylor, Nuclear electron double resonance in liquids, in: E.F. Mooney (Ed.), Annual Reports on NMR Spectroscopy, Academic Press, 1969, pp. 293–344.

[215] E.H. Poindexter, J.R. Stewart, P.J. Caplan, Dynamic polarization of fluorine nuclei in solutions of selected free radicals, J. Chem. Phys. 47 (1967) 2862–2873, https://doi.org/10.1063/1.1712309.

[216] H.C. Dorn, T.E. Glass, R. Gitti, K.H. Tsai, Transfer of ^{1}H and ^{13}C dynamic nuclear polarization from immobilized nitroxide radicals to flowing liquids, Appl. Magn. Reson. 2 (1991) 9–27, https://doi.org/10.1007/BF03166265.

[217] M.D. Lingwood, T.A. Siaw, N. Sailasuta, B.D. Ross, P. Bhattacharya, S. Han, Continuous flow Overhauser dynamic nuclear polarization of water in the fringe field of a clinical magnetic resonance imaging system for authentic image contrast, J. Magn. Reson. 205 (2010) 247–254, https://doi.org/10.1016/j.jmr.2010.05.008.

[218] M.D. Lingwood, A.J. Sederman, M.D. Mantle, L.F. Gladden, S. Han, Overhauser dynamic nuclear polarization amplification of NMR flow imaging, J. Magn. Reson. 216 (2012) 94–100, https://doi.org/10.1016/j.jmr.2012.01.007.

[219] J.G. Krummenacker, V.P. Denysenkov, T.F. Prisner, Liquid state DNP on metabolites at 260 GHz EPR/400 MHz NMR frequency, Appl. Magn. Reson. 43 (2012) 139–146, https://doi.org/10.1007/s00723-012-0351-8.

[220] V. Denysenkov, M. Terekhov, R. Maeder, S. Fischer, S. Zangos, T. Vogl, T. F. Prisner, Continuous-flow DNP polarizer for MRI applications at 1.5T, Sci. Rep. 7 (2017) 44010, https://doi.org/10.1038/srep44010.

[221] R. Kircher, H. Hasse, K. Münnemann, High flow-rate benchtop NMR spectroscopy enabled by continuous Overhauser DNP, Anal. Chem. 93 (2021) 8897–8905, https://doi.org/10.1021/acs.analchem.1c01118.

[222] R. Kircher, S. Mross, H. Hasse, K. Münnemann, Functionalized controlled porous glasses for producing radical-free hyperpolarized liquids by Overhauser DNP, Molecules 27 (2022) 6402, https://doi.org/10.3390/molecules27196402.

[223] J. Phuong, B. Salgado, T. Labusch, H. Hasse, K. Münnemann, Overhauser dynamic nuclear polarization enables single scan benchtop ^{13}C nmr spectroscopy in continuous-flow, Anal. Chem. 97 (2025) 4308–4317, https://doi.org/10.1021/acs.analchem.4c03985.

[224] J. Mandral, J. Phuong, J. Farjon, P. Giraudeau, K. Münnemann, J.-N. Dumez, Ultrafast 2D benchtop NMR spectroscopy enhanced by flow Overhauser dynamic nuclear polarization, J. Magn. Reson. Open 23 (2025) 100195, https://doi.org/10.1016/j.jmro.2025.100195.

[225] M. Reese, D. Lennartz, T. Marquardsen, P. Höfer, A. Tavernier, P. Carl, T. Schippmann, M. Bennati, T. Carlomagno, F. Engelke, C. Griesinger, Construction of a liquid-state NMR DNP shuttle spectrometer: first experimental results and evaluation of optimal performance characteristics, Appl. Magn. Reson. 34 (2008) 301–311, https://doi.org/10.1007/s00723-008-0131-7.

[226] M. Reese, M.-T. Türke, I. Tkach, G. Parigi, C. Luchinat, T. Marquardsen, A. Tavernier, P. Höfer, F. Engelke, C. Griesinger, M. Bennati, ^{1}H and ^{13}C dynamic nuclear polarization in aqueous solution with a two-field (0.35 T/14 T) shuttle DNP spectrometer, J. Am. Chem. Soc. 131 (2009) 15086–15087, https://doi.org/10.1021/ja905959n.

[227] A. Krahn, P. Lottmann, T. Marquardsen, A. Tavernier, M.-T. Türke, M. Reese, A. Leonov, M. Bennati, P. Hoefer, F. Engelke, C. Griesinger, Shuttle DNP spectrometer with a two-center magnet, Phys. Chem. Chem. Phys. 12 (2010) 5830–5840, https://doi.org/10.1039/C003381B.

[228] J.A. Villanueva-Garibay, G. Annino, P.J.M. van Bentum, A.P.M. Kentgens, Pushing the limit of liquid-state dynamic nuclear polarization at high field, Phys. Chem. Chem. Phys. 12 (2010) 5846–5849, https://doi.org/10.1039/C002554M.

[229] E.V. Kryukov, M.E. Newton, K.J. Pike, D.R. Bolton, R.M. Kowalczyk, A.P. Howes, M.E. Smith, R. Dupree, DNP enhanced NMR using a high-power 94 GHz microwave source: a study of the TEMPOL radical in toluene, Phys. Chem. Chem. Phys. 12 (2010) 5757–5765, https://doi.org/10.1039/C003189E.

[230] S.G.J. van Meerten, M.C.D. Tayler, A.P.M. Kentgens, P.J.M. van Bentum, Towards Overhauser DNP in supercritical CO_2, J. Magn. Reson. 267 (2016) 30–36, https://doi.org/10.1016/j.jmr.2016.04.002.

[231] P. Neugebauer, J.G. Krummenacker, V.P. Denysenkov, C. Helmling, C. Luchinat, G. Parigi, T.F. Prisner, High-field liquid state NMR hyperpolarization: a combined DNP/NMRD approach, Phys. Chem. Chem. Phys. 16 (2014) 18781–18787, https://doi.org/10.1039/c4cp02451f.

[232] T. Prisner, V. Denysenkov, D. Sezer, Liquid state DNP at high magnetic fields: instrumentation, experimental results and atomistic modelling by molecular dynamics simulations, J. Magn. Reson. 264 (2016) 68–77, https://doi.org/10.1016/j.jmr.2015.11.004.

[233] J.M. Robert, R.F. Evilia, High-resolution nuclear magnetic resonance spectroscopy of quadrupolar nuclei: nitrogen-14 and oxygen-17 examples, J. Am. Chem. Soc. 107 (1985) 3733–3735, https://doi.org/10.1021/ja00298a063.

[234] R.A. Wind, S. Bai, J.Z. Hu, M.S. Solum, P.D. Ellis, D.M. Grant, R.J. Pugmire, C. M. Taylor, C.R. Yonker, ^{1}H dynamic nuclear polarization in supercritical ethylene at 1.4 T, J. Magn. Reson. 143 (2000) 233–239, https://doi.org/10.1006/jmre.2000.2016.

[235] K.L. Kirk, Fluorine in medicinal chemistry: recent therapeutic applications of fluorinated small molecules, J. Fluor. Chem. 127 (2006) 1013–1029, https://doi.org/10.1016/j.jfluchem.2006.06.007.

[236] E.P. Gillis, K.J. Eastman, M.D. Hill, D.J. Donnelly, N.A. Meanwell, Applications of fluorine in medicinal chemistry, J. Med. Chem. 58 (2015) 8315–8359, https://doi.org/10.1021/acs.jmedchem.5b00258.

[237] G. Theodoridis, Fluorine-Containing Agrochemicals: An Overview of Recent Developments, in: Fluorine and the Environment - Agrochemicals, Archaeology, Green Chemistry & Water, 2006, pp. 121–175.

[238] Y. Ogawa, E. Tokunaga, O. Kobayashi, K. Hirai, N. Shibata, Current contributions of organofluorine compounds to the agrochemical industry, iScience 23 (2020) 101467, https://doi.org/10.1016/j.isci.2020.101467.

[239] T. Imae, Fluorinated polymers, Curr. Opin. Colloid Interface Sci. 8 (2003) 307–314, https://doi.org/10.1016/s1359-0294(03)00050-5.

[240] I. Furó, I. Iliopoulos, P. Stilbs, Structure and dynamics of associative water-soluble polymer aggregates as seen by ^{19}F NMR spectroscopy, J. Phys. Chem. B 104 (1999) 485–494, https://doi.org/10.1021/jp9927404.

[241] S.L. Grage, X. Xu, M. Schmitt, P. Wadhwani, A.S. Ulrich, ^{19}F-labeling of peptides revealing long-range NMR distances in fluid membranes, J. Phys. Chem. Lett. 5 (2014) 4256–4259, https://doi.org/10.1021/jz502195t.

[242] D. Jirak, A. Galisova, K. Kolouchova, D. Babuka, M. Hruby, Fluorine polymer probes for magnetic resonance imaging: quo vadis? MAGMA 32 (2019) 173–185, https://doi.org/10.1007/s10334-018-0724-6.

[243] K.T. Cockburn, B.D. Sykes, Fluorine labelling for in situ ^{19}F NMR in oriented systems, J. Biomol. NMR 78 (2024) 119–124, https://doi.org/10.1007/s10858-024-00438-7.

[244] A.M. Gronenborn, Small, but powerful and attractive: ^{19}F in biomolecular NMR, Structure 30 (2022) 6–14, https://doi.org/10.1016/j.str.2021.09.009.
[245] J.X. Yu, R.R. Hallac, S. Chiguru, R.P. Mason, New frontiers and developing applications in ^{19}F NMR, Prog. Nucl. Magn. Reson. Spectrosc. 70 (2013) 25–49, https://doi.org/10.1016/j.pnmrs.2012.10.001.
[246] M.V. Gomez, S. Baas, A.H. Velders, Multinuclear 1D and 2D NMR with ^{19}F-photo-CIDNP hyperpolarization in a microfluidic chip with untuned microcoil, Nat. Commun. 14 (2023) 3885, https://doi.org/10.1038/s41467-023-39537-8.
[247] J. Bernarding, C. Bruns, I. Prediger, M. Mutzel, M. Plaumann, Detection of sub-nmol amounts of the antiviral drug favipiravir in ^{19}F MRI using photo-chemically induced dynamic nuclear polarization, Sci. Rep. 14 (2024) 1527, https://doi.org/10.1038/s41598-024-51454-4.
[248] A.I. Silva Terra, M. Rossetto, C.L. Dickson, G. Peat, D. Uhrin, M.E. Halse, Enhancing 19F benchtop NMR spectroscopy by combining Para-hydrogen hyperpolarization and multiplet refocusing, ACS Meas. Sci. Au 3 (2023) 73–81, https://doi.org/10.1021/acsmeasuresciau.2c00055.
[249] Y. Lee, H. Zeng, S. Ruedisser, A.D. Gossert, C. Hilty, Nuclear magnetic resonance of hyperpolarized fluorine for characterization of protein–ligand interactions, J. Am. Chem. Soc. 134 (2012) 17448–17451, https://doi.org/10.1021/ja308437h.
[250] J. Hu, J. Kim, C. Hilty, Detection of protein–ligand interactions by ^{19}F nuclear magnetic resonance using hyperpolarized water, J. Phys. Chem. Lett. 13 (2022) 3819–3823, https://doi.org/10.1021/acs.jpclett.2c00448.
[251] O. Neudert, C. Mattea, H.W. Spiess, S. Stapf, K. Münnemann, A comparative study of ^{1}H and ^{19}F Overhauser DNP in fluorinated benzenes, Phys. Chem. Chem. Phys. 15 (2013) 20717–20726, https://doi.org/10.1039/c3cp52912f.
[252] A. Peksoz, A. Yalciner, M.A. Cimenoglu, A low field fluorine-electron double resonance study for GALV and BDPA in some aliphatic and aromatic solvents, Z. Naturforsch. A 64 (2009) 477–484, https://doi.org/10.1515/zna-2009-7-810.
[253] R.H. Webb, N.v. Nghia, M.R. Pearlman, E.H. Poindexter, P.J. Caplan, J. A. Potenza, Dynamic nuclear polarization: collision mechanics in fluorocarbon solutions, J. Chem. Phys. 50 (1969) 4408–4417, https://doi.org/10.1063/1.1670911.
[254] E.H. Poindexter, P.J. Caplan, B.E. Wagner, R.D. Bates, Relaxation of fluorine nuclei by collisions with free radicals, J. Chem. Phys. 61 (1974) 3821–3827, https://doi.org/10.1063/1.1682571.
[255] A. Dey, A. Banerjee, Unusual Overhauser dynamic nuclear polarization behavior of fluorinated alcohols at room temperature, J. Phys. Chem. B 123 (2019) 10463–10469, https://doi.org/10.1021/acs.jpcb.9b08144.
[256] H. Guo, Y.C. Fan, Z. Sun, Y. Wu, O. Kwon, Phosphine organocatalysis, Chem. Rev. 118 (2018) 10049–10293, https://doi.org/10.1021/acs.chemrev.8b00081.
[257] M.d.M. Conejo, A. Pastor, F. Montilla, A. Galindo, P atom as ligand in transition metal chemistry: structural aspects, Coord. Chem. Rev. 434 (2021) 213730, https://doi.org/10.1016/j.ccr.2020.213730.
[258] F. Bhinderwala, P. Evans, K. Jones, B.R. Laws, T.G. Smith, M. Morton, R. Powers, Phosphorus NMR and its application to metabolomics, Anal. Chem. 92 (2020) 9536–9545, https://doi.org/10.1021/acs.analchem.0c00591.
[259] R.G. Shulman, T.R. Brown, K. Ugurbil, S. Ogawa, S.M. Cohen, J.A. den Hollander, Cellular applications of ^{31}P and ^{13}C nuclear magnetic resonance, Science 205 (1979) 160–166, https://doi.org/10.1126/science.36664.
[260] D.G. Gorenstein, Phosphorous-31 NMR: Principles and Applications, Academic Press, 2012.
[261] J.A. Potenza, P.J. Caplan, E.H. Poindexter, Low-field dynamic polarization of ^{31}P nuclei, J. Chem. Phys. 49 (1968) 2461–2463, https://doi.org/10.1063/1.1670434.
[262] R.A. Dwek, N.L. Paddock, J.A. Potenza, E.H. Poindexter, Dynamic nuclear polarization in phosphonitrilic ring compounds, J. Am. Chem. Soc. 91 (1969) 5436–5439, https://doi.org/10.1021/ja01048a006.
[263] R.A. Dwek, P.J. Captlan, E.H. Poindexter, J.A. Potenza, Dynamic nuclear polarization in phosphorus compounds at 74 gauss, Chem. Phys. Lett. 3 (1969) 283–285, https://doi.org/10.1016/0009-2614(69)80230-7.
[264] J.A. Potenza, E.H. Poindexter, P.J. Caplan, R.A. Dwek, Dynamic polarization of phosphorus-31 nuclei - some effects of chemical environment, J. Am. Chem. Soc. 91 (1969) 4356–4360, https://doi.org/10.1021/ja01044a006.
[265] E.H. Poindexter, G.R. Neil, Dynamic nuclear polarization in phosphorus compounds with perchlorotriphenylmethyl and other radicals, J. Chem. Phys. 52 (1970) 5648–5651, https://doi.org/10.1063/1.1672839.
[266] E.H. Poindexter, R.L. Glazer, Dynamic polarization of phosphorus nuclei by nitroxide radicals, J. Am. Chem. Soc. 92 (1970) 4784–4786, https://doi.org/10.1021/ja00719a004.
[267] W. Müller-Warmuth, H. Grützediek, R. Van Steenwinkel, A quantitative study of the nuclear-electron Overhauser effect of phosphorus-31 in solutions, Z. Naturforsch. A 25 (1970) 1696–1702, https://doi.org/10.1515/zna-1970-1121.
[268] P. Schanda, E. Kupce, B. Brutscher, SOFAST-HMQC experiments for recording two-dimensional heteronuclear correlation spectra of proteins within a few seconds, J. Biomol. NMR 33 (2005) 199–211, https://doi.org/10.1007/s10858-005-4425-x.
[269] M. Mishkovsky, L. Frydman, Principles and progress in ultrafast multidimensional nuclear magnetic resonance, Annu. Rev. Phys. Chem. 60 (2009) 429–448, https://doi.org/10.1146/annurev.physchem.040808.090420.
[270] P. Giraudeau, L. Frydman, Ultrafast 2D NMR: an emerging tool in analytical spectroscopy, Annu. Rev. Anal. Chem. 7 (2014) 129–161, https://doi.org/10.1146/annurev-anchem-071213-020208.
[271] M. Levien, Development of ^{13}C Liquid State Dynamic Nuclear Polarization at 9.4 Tesla, Georg-August-Universität Göttingen, 2023.
[272] A. Dey, A. Banerjee, N. Chandrakumar, Transferred Overhauser DNP: a fast, efficient approach for room temperature ^{13}C ODNP at moderately low fields and natural abundance, J. Phys. Chem. B 121 (2017) 7156–7162, https://doi.org/10.1021/acs.jpcb.7b05081.
[273] T.J. Keller, T. Maly, Overhauser dynamic nuclear polarization (ODNP)-enhanced two-dimensional proton NMR spectroscopy at low magnetic fields, Magn Reson 2 (2021) 117–128, https://doi.org/10.5194/mr-2-117-2021.
[274] U. Piantini, O. Sorensen, R.R. Ernst, Multiple quantum filters for elucidating NMR coupling networks, J. Am. Chem. Soc. 104 (1982) 6800–6801, https://doi.org/10.1021/ja00388a062.
[275] M. Kadkhodaie, O. Rivas, M. Tan, A. Mohebbi, A.J. Shaka, Broadband homonuclear cross polarization using flip-flop spectroscopy, J. Magn. Reson. 91 (1991) 437–443, https://doi.org/10.1016/0022-2364(91)90210-k.
[276] A. Bax, R. Freeman, S.P. Kempsell, Natural abundance carbon-13-carbon-13 coupling observed via double-quantum coherence, J. Am. Chem. Soc. 102 (2002) 4849–4851, https://doi.org/10.1021/ja00534a056.
[277] G.A. Morris, R. Freeman, Enhancement of nuclear magnetic resonance signals by polarization transfer, J. Am. Chem. Soc. 101 (1979) 760–762, https://doi.org/10.1021/ja00497a058.
[278] L. Braunschweiler, R.R. Ernst, Coherence transfer by isotropic mixing: application to proton correlation spectroscopy, J. Magn. Reson. 53 (1983) 521–528, https://doi.org/10.1016/0022-2364(83)90226-3.
[279] T.L. Hwang, M. Kadkhodaei, A. Mohebbi, A.J. Shaka, Coherent and incoherent magnetization transfer in the rotating frame, Magn. Reson. Chem. 30 (1992) S24–S34, https://doi.org/10.1002/mrc.1260301308.
[280] N. Matsumoto, K. Nishimura, N. Kimizuka, Y. Nishiyama, K. Tateishi, T. Uesaka, N. Yanai, Proton hyperpolarization relay from nanocrystals to liquid water, J. Am. Chem. Soc. 144 (2022) 18023–18029, https://doi.org/10.1021/jacs.2c07518.
[281] T.R. Eichhorn, A.J. Parker, F. Josten, C. Muller, J. Scheuer, J.M. Steiner, M. Gierse, J. Handwerker, M. Keim, S. Lucas, M.U. Qureshi, A. Marshall, A. Salhov, Y. Quan, J. Binder, K.D. Jahnke, P. Neumann, S. Knecht, J. W. Blanchard, M.B. Plenio, F. Jelezko, L. Emsley, C.C. Vassiliou, P. Hautle, I. Schwartz, Hyperpolarized solution-state NMR spectroscopy with optically polarized crystals, J. Am. Chem. Soc. 144 (2022) 2511–2519, https://doi.org/10.1021/jacs.1c09119.
[282] S. Wi, A. Giannouli, K. Butbul, J. Lumata, T. Dubroca, F. Scott, Z. Dowdell, R. W. Schurko, H. Van Tol, L. Frydman, Toward generalized solution-state ^{1}H DNP NMR via particle-mediated cross-relaxation, J. Phys. Chem. Lett. 16 (2025) 6627–6636, https://doi.org/10.1021/acs.jpclett.5c01398.
[283] D. Neuhaus, P.A. Evans, Structural studies of proteins in solution using proton nuclear magnetic resonance, in: Spectroscopic Methods and Analyses: NMR, Mass Spectrometry, and Metalloprotein Techniques, Springer, 1993, pp. 15–67.
[284] B. Vögeli, The nuclear Overhauser effect from a quantitative perspective, Prog. Nucl. Magn. Reson. Spectrosc. 78 (2014) 1–46.
[285] M. Reinhard, Development of ^{19}F and ^{31}P Dynamic Nuclear Polarization in the Liquid State, Georg-August-Universität Göttingen, 2024.
[286] P. Kaderavek, F. Ferrage, G. Bodenhausen, D. Kurzbach, High-resolution NMR of folded proteins in hyperpolarized physiological solvents, Chem. A Eur. J. 24 (2018) 13418–13423, https://doi.org/10.1002/chem.201802885.
[287] O. Szekely, G.L. Olsen, I.C. Felli, L. Frydman, High-resolution 2D NMR of disordered proteins enhanced by hyperpolarized water, Anal. Chem. 90 (2018) 6169–6177, https://doi.org/10.1021/acs.analchem.8b00585.
[288] F. Torres, M. Butikofer, G.R. Stadler, A. Renn, H. Kadavath, R. Bobrovs, K. Jaudzems, R. Riek, Ultrafast fragment screening using photo-hyperpolarized (CIDNP) NMR, J. Am. Chem. Soc. 145 (2023) 12066–12080, https://doi.org/10.1021/jacs.3c01392.
[289] K.G. Valentine, G. Mathies, S. Bedard, N.V. Nucci, I. Dodevski, M.A. Stetz, T. V. Can, R.G. Griffin, A.J. Wand, Reverse micelles as a platform for dynamic nuclear polarization in solution NMR of proteins, J. Am. Chem. Soc. 136 (2014) 2800–2807, https://doi.org/10.1021/ja4107176.
[290] A. van der Ham, Discontinuous hyperpolarization schemes in liquid-state Overhauser dynamic nuclear polarization experiments, J. Magn. Reson. Open 21 (2024), https://doi.org/10.1016/j.jmro.2024.100160.
[291] J. Phuong, R. Kircher, S. Mross, B. Salgado, H. Hasse, K. Münnemann, Quantitative nuclear magnetic resonance spectroscopy with Overhauser dynamic nuclear polarization, ChemPhysChem 26 (2025) e202401052, https://doi.org/10.1002/cphc.202401052.
[292] P. Giraudeau, Challenges and perspectives in quantitative NMR, Magn. Reson. Chem. 55 (2016) 61–69, https://doi.org/10.1002/mrc.4475.
[293] E.R. McCarney, B.D. Armstrong, R. Kausik, S. Han, Dynamic nuclear polarization enhanced nuclear magnetic resonance and electron spin resonance studies of hydration and local water dynamics in micelle and vesicle assemblies, Langmuir 24 (2008) 10062–10072, https://doi.org/10.1021/la800334k.
[294] B.D. Armstrong, S. Han, Overhauser dynamic nuclear polarization to study local water dynamics, J. Am. Chem. Soc. 131 (2009) 4641–4647, https://doi.org/10.1021/ja809259q.
[295] J.M. Franck, Y. Ding, K. Stone, P.Z. Qin, S. Han, Anomalously rapid hydration water diffusion dynamics near DNA surfaces, J. Am. Chem. Soc. 137 (2015) 12013–12023, https://doi.org/10.1021/jacs.5b05813.
[296] I. Kaminker, R. Barnes, S. Han, Overhauser dynamic nuclear polarization studies on local water dynamics, Methods Enzymol. 564 (2015) 457–483, https://doi.org/10.1016/bs.mie.2015.06.040.
[297] J.M. Franck, S. Han, Overhauser dynamic nuclear polarization for the study of hydration dynamics, explained, Methods Enzymol. 615 (2019) 131–175, https://doi.org/10.1016/bs.mie.2018.09.024.

[298] J. Carreras, M. Caputo, D. Colasurdo, M. Pila, D. Ruiz, S. Laurella, Elucidation of organic reaction mechanisms using nuclear magnetic resonance: a review, Appl. Magn. Reson. 55 (2024) 1335–1376, https://doi.org/10.1007/s00723-024-01676-6.
[299] V. Sans, L. Cronin, Towards dial-a-molecule by integrating continuous flow, analytics and self-optimisation, Chem. Soc. Rev. 45 (2016) 2032–2043, https://doi.org/10.1039/c5cs00793c.
[300] B. Meyer, T. Peters, NMR spectroscopy techniques for screening and identifying ligand binding to protein receptors, Angew. Chem. Int. Ed. 42 (2003) 864–890, https://doi.org/10.1002/anie.200390233.
[301] C.A. Lepre, J.M. Moore, J.W. Peng, Theory and applications of NMR-based screening in pharmaceutical research, Chem. Rev. 104 (2004) 3641–3676, https://doi.org/10.1021/cr030409h.
[302] K. Meyer, S. Kern, N. Zientek, G. Guthausen, M. Maiwald, Process control with compact NMR, TrAC, Trends Anal. Chem. 83 (2016) 39–52, https://doi.org/10.1016/j.trac.2016.03.016.
[303] S. Bowen, C. Hilty, Temporal chemical shift correlations in reactions studied by hyperpolarized nuclear magnetic resonance, Anal. Chem. 81 (2009) 4543–4547, https://doi.org/10.1021/ac900456q.
[304] H. Zeng, Y. Lee, C. Hilty, Quantitative rate determination by dynamic nuclear polarization enhanced NMR of a Diels-Alder reaction, Anal. Chem. 82 (2010) 8897–8902, https://doi.org/10.1021/ac101670n.
[305] A.D. Robinson, F. Hill-Casey, S.B. Duckett, M.E. Halse, Quantitative reaction monitoring using parahydrogen-enhanced benchtop NMR spectroscopy, Phys. Chem. Chem. Phys. 26 (2024) 14317–14328, https://doi.org/10.1039/d3cp06221j.
[306] K. Konsewicz, G. Laczko, I. Papai, V.V. Zhivonitko, Activation of H_2 using ansa-aminoboranes: solvent effects, dynamics, and spin hyperpolarization, Phys. Chem. Chem. Phys. 26 (2024) 3197–3207, https://doi.org/10.1039/d3cp05816f.
[307] Y. Lee, G.S. Heo, H. Zeng, K.L. Wooley, C. Hilty, Detection of living anionic species in polymerization reactions using hyperpolarized NMR, J. Am. Chem. Soc. 135 (2013) 4636–4639, https://doi.org/10.1021/ja4001008.
[308] T. Harris, P. Giraudeau, L. Frydman, Kinetics from indirectly detected hyperpolarized NMR spectroscopy by using spatially selective coherence transfers, Chem. A Eur. J. 17 (2011) 697–703, https://doi.org/10.1002/chem.201002151.
[309] K.M. Ward, A.H. Aletras, R.S. Balaban, A new class of contrast agents for MRI based on proton chemical exchange dependent saturation transfer (CEST), J. Magn. Reson. 143 (2000) 79–87, https://doi.org/10.1006/jmre.1999.1956.
[310] J. Zhou, P.C.M.V. Zijl, Chemical exchange saturation transfer imaging and spectroscopy, Prog. Nucl. Magn. Reson. Spectrosc. 48 (2006) 109–136, https://doi.org/10.1016/j.pnmrs.2006.01.001.
[311] A. Lesage, M. Lelli, D. Gajan, M.A. Caporini, V. Vitzthum, P. Mieville, J. Alauzun, A. Roussey, C. Thieuleux, A. Mehdi, G. Bodenhausen, C. Coperet, L. Emsley, Surface enhanced NMR spectroscopy by dynamic nuclear polarization, J. Am. Chem. Soc. 132 (2010) 15459–15461, https://doi.org/10.1021/ja104771z.
[312] A.J. Rossini, A. Zagdoun, M. Lelli, A. Lesage, C. Coperet, L. Emsley, Dynamic nuclear polarization surface enhanced NMR spectroscopy, Acc. Chem. Res. 46 (2013) 1942–1951, https://doi.org/10.1021/ar300322x.